NEUROIMAGING AND EXTRACELLULAR MATRIX BASED APPROACHES TO OPTIC NEUROPATHY

by

Yolandi van der Merwe

Bachelor of Science, University of Pittsburgh, 2013

Submitted to the Graduate Faculty of

Swanson School of Engineering in partial fulfillment

of the requirements for the degree of

Doctor of Philosophy

University of Pittsburgh

2018

UNIVERSITY OF PITTSBURGH

SWANSON SCHOOL OF ENGINEERING

This dissertation was presented

by

Yolandi van der Merwe

It was defended on

March 30th, 2018

and approved by

Michael B. Steketee, PhD, Adjunct Professor, Department of Ophthalmology

Kevin C. Chan, PhD, Adjunct Professor, Department of Ophthalmology

William R. Wagner, PhD, Professor, Department of Surgery

Kacey Marra, PhD, Associate Professor, Department of Plastic Surgery

Jeff Gross, PhD, Professor, Department of Ophthalmology

Dissertation Director: Stephen F. Badylak, DVM, PhD, MD, Professor, Department of Surgery

NEUROIMAGING AND EXTRACELLULAR MATRIX BASED APPROACHES TO OPTIC NEUROPATHY

Yolandi van der Merwe, PhD

University of Pittsburgh, 2018

There are approximately 2.4 million acute ocular injuries annually in the U.S. Twenty percent of these injuries result in partial or complete blindness due to traumatic injury to retinal ganglion cells (RGC). Like all central nervous system (CNS) neurons, RGC fail to regenerate injured axons because of multiple factors that lead to secondary tissue damage. We currently lack a therapeutic platform that can alter the default non-regenerative healing response. Stated differently, we lack a method to preserve or restore CNS function.

Extracellular matrix (ECM) bioscaffolds have been shown to promote site appropriate tissue remodeling in multiple anatomical sites through stem and progenitor cell recruitment, proliferation, and differentiation. Additionally, redirection of the default immune response is facilitated by providing factors derived from the ECM that promote the phenotypic transition of immune cells from a pro-inflammatory to a pro-remodeling state. Recently discovered matrix bound nanovesicles (MBV) were found in all tested laboratory produced and commercially available ECM. MBV are bioactive and recapitulate some effects of the parent ECM from which they are derived and represent a potentially significant vertical advance in treating traumatic optic nerve and retinal injuries.

The objective of the present thesis was to determine the efficacy of ECM and MBV to repair optic nerve and retinal tissue. First, we determined the functional and spatiotemporal changes in the visual system after acute ocular injury. Next, we measured the effect of ECM on optic nerve remodeling and the inflammatory response. Finally, we characterized the effect of

MBV on the inflammatory response, RGC survival, and retinal function after acute ocular injury. ECM improved tissue remodeling in some animals. However, the results were variable, indicating ECM has the potential to improve CNS remodeling, but may not be the optimal treatment platform in the visual system. MBV increased RGC neurite outgrowth and suppressed pro-inflammatory microglia and astrocyte polarization *in vitro*, and increased RGC survival and retinal function after ocular injury. MBV offer an easily injectable, minimally invasive therapy that can improve RGC survival and potentially increase visual function after ocular injury.

TABLE OF CONTENTS

LIST OF FIGURES

PREFACE

Nine years ago, I left South Africa to pursue a bioengineering B.S degree at the University of Pittsburgh. I started as an undergraduate researcher in June 2011 and over the last seven years have developed into an independent researcher capable of formulating and executing studies to further the field of regenerative medicine. In my time spent here in the United States, I have grown professionally and personally, and none of this would have been possible without the constant support from my family, friends, mentors, and co-workers. I would like to thank Dr. Michael Steketee for providing me with invaluable guidance throughout my graduate career, for everything from experimental support, writing tips, career guidance, and everything else that I needed. Dr. Stephen Badylak took me into his laboratory as an undergraduate student and again as a final year graduate student, and I owe him my sincerest gratitude for all the support, opportunities, and guidance he provided. I would like to thank Dr. Kevin Chan for all the support, guidance, and opportunities he provided that helped shape me into the researcher I am today. I would also like to thank my committee members, Drs. William Wagner, Kacey Marra, and Jeff Gross, for their support and insight.

I would like to acknowledge my laboratory co-workers and CNS research group who worked with me on all CNS and ocular related projects: Anne Faust, Tanchen Ren, Leon Ho, Xiaoling Yang, George Hussey, Mark Murdock, Janet Reing, and Scott Johnson. I also thank all

the undergraduate students who helped support my research: Bianca Leonard, Apoorva Kandakatla, Ecem Sakalli, and Caroline Westrick.

Thank you also to all my closest Pittsburgh friends who supported me along the way: Anne Faust, Liza Bruk, Erika Pliner, Jessi Mischel, Erinn Grigsby, Stephanie Wiltman, Sanjeev Khanna, Rousseau Kluever, Alex Rodenkirk, and Scott Salo. A special thank you to Anne Faust, who not only helped me with all aspects of research, but also became one of my closest friends in the process.

And finally, I would like to thank my family: my mom and dad, Christa and Deon, and brother, Jannes. Although you are far away, your unwavering support shone through the daily messages and check in calls and you have always been there for me through everything. I appreciate everything you have done for me to get me to where I am today and will forever be truly grateful.

1.0 INTRODUCTION AND SPECIFIC AIMS

Regenerative medicine is a branch of translational medicine aimed at replacing or remodeling damaged tissue or organs with the goal to restore lost function. Tissue engineering is a sub-section of regenerative medicine that utilizes engineering and materials science principles to restore or improve tissue functionality. Through tissue engineering, materials can be developed that utilize naturally occurring bioactive molecules and cellular components, or synthetic polymers and components to support functional tissue recovery. Naturally derived scaffolds are typically complex materials comprised of growth factors, cytokines, proteins, small molecules, and other bioactive factors, while synthetic materials can be engineered to deliver specific combinations of desired factors. Naturally derived extracellular matrix (ECM) biologic scaffolds are widely used in regenerative medicine and are produced through decellularization of healthy tissue to remove cellular content, while maintaining tissue specific bioactive molecules. ECM maintains homeostasis in tissues and organs throughout the body, therefore a logical approach is to use these scaffolds to influence the microenvironment to support normal tissue recovery and functionality. Recently, bioactive matrix bound nanovesicles (MBV) were found to be present in all available ECM scaffolds and were shown to recapitulate some favorable responses associated with ECM scaffolds. MBV open a new area of ECM technology and allows ECM bioactive components to be delivered in minimally invasive manners, thereby promoting functional recovery in injured tissues.

1.1 TRAUMATIC OPTIC NEUROPATHY

Traumatic injury to the central nervous system (CNS) results in irreversible neurologic impairments, and in the visual system injury often results in permanent vision loss. In the U.S., there are approximately 2.4 million eye injuries every year and the majority occur in 18-45 year-olds, while up to 35% occur in individuals under the age of 17 [1, 2]. Foreign objects in the eye have the highest injury rate, followed by contusions and open wounds, and the majority of ocular injuries are treated in emergency departments (50.7%), followed by private physicians' offices (38.7%) [3]. Currently, an estimated 4.2 million people in the U.S. are visually impaired while 1.3 million are legally blind [4, 5], and besides drastically decreasing the patients' quality of life, vision impairment is estimated to incur a total annual economic burden of $38.2 billion in the U.S. [6]. Therefore, there exists a need for a treatment therapy that can prevent ocular injury and vision loss, thereby improving quality of life and decreasing economic burden of affected individuals.

1.2 NEUROIMAGING OF THE VISUAL SYSTEM

The current gold standard for detecting axon degeneration and the efficacy of experimental therapies after injury is with histology. However, histology offers no information regarding the rate of tissue remodeling or tissue functionality. By utilizing multi-parametric imaging modalities in concert with histology, it is possible to gain a more comprehensive understanding of functional and structural changes in the visual system and central nervous system. In addition to detecting axon degeneration, multi-parametric imaging allows us to analyze the effects of therapeutics on the injured visual system over time as it pertains to tissue functionality and white matter integrity.

Diffusion tensor imaging (DTI) measures water diffusion patterns in compartments and gives information regarding microstructural and fiber organization [7, 8], therefore longitudinal DTI can be used to characterize the structural integrity of the visual system over time. Magnetization transfer imaging (MTI) measures the magnetization transfer between water bound to macromolecules and the surrounding free water [9], and is therefore able to examine changes in macromolecular structures. Manganese-enhanced magnetic resonance imaging (MEMRI) has been used to study the functional and structural changes in the central nervous system [10-12], as well as in identifying structural changes in the visual system [13-17]. Mn^{2+} ions act as a calcium analogue that can enter calcium channels following neuronal activation [11, 18] and can be actively transported along axonal pathways via microtubules [11, 19, 20], thereby giving information regarding axonal transport and the integrity of axonal pathway structures. Investigation of the structural organization of the visual system in glaucoma patients has also shown that glaucoma affects both vision-related and non-vision related cortical regions in the brain, which may reflect the severity of the disease [21]. Analysis of the brain network pattern revealed that while efficiency of functional communication is preserved globally, the efficiency of functional communication is affected at a local level [22]. Therefore, resting state functional connectivity MRI (RSfcMRI) can be used to examine the functional connectivity between brain regions throughout the visual system. In the first aim, two models of unilateral IOP elevation were used as models of optic neuropathy, and the effects of IOP elevation on the visual system was determined via optokinetics, multi-parametric MRI, and histology.

1.3 PRIMARY AND SECONDARY INJURY AFTER CNS INJURY

Primary injuries following ocular trauma commonly involve impact and compression that result in tissue necrosis [23], neuronal cell apoptosis [24], and axonal death [25]. Following initial injury to the CNS, including the visual system, axons fail to regenerate due to numerous injury-induced factors that suppress axon regeneration, including poor intrinsic axon growth ability [26], dysfunctional organelle dynamics [27], lost neurotrophic support [28], inhibitory molecules expressed by glia [29] or released during cellular injury [30], and a tissue-destructive inflammatory immune response [31] that leads to astrogliosis and permanent scarring. Astrogliosis is caused by an increase in reactive astrocytes that deposit scar tissue, termed the glial scar, consisting of proteoglycans [32, 33]. The glial scar forms a physical and chemical barrier that prevents axonal regeneration by releasing axon growth inhibiting molecules, including chondroitin sulfate proteoglycan (CSPG) [34], semaphorin-3 [35], ephrin-B2 [36], and Slit proteins [37]. A recent study showed that pro-inflammatory microglia polarize reactive astrocytes to the pro-inflammatory phenotype after optic nerve injury [38], suggesting modulating microglia phenotype can influence scar tissue formation and functional recovery after ocular injury.

After CNS injury, a pro-inflammatory, innate immune response contributes to permanently lost neuronal function by promoting changes in the micro-environment and extracellular matrix (ECM) that lead to CNS neuronal degeneration and permanent scarring. This pro-inflammatory immune response is largely due to activated resident microglia and infiltrating macrophages adopting a predominantly pro-inflammatory, M1-like, phenotype. M1-like microglia and macrophages release pro-inflammatory factors, including cytokines and microvesicles, that recruit additional cells, including microglia, astrocytes, and naïve blood macrophages, that enter the injured tissue and polarize toward M1-like phenotypes that can lead to secondary tissue damage

and increased scarring. After the initial inflammatory response resolves, M1-like macrophages and microglia persist due to pro-inflammatory cytokine signaling cascades that act by both autocrine and paracrine signaling mechanisms to maintain pro-inflammatory signaling, ultimately leading to permanent scarring. Scar tissue also appears to promote persistent inflammatory signaling. Thus, a logical approach to treating CNS injuries is to develop immunomodulatory strategies that interrupt cyclical pro-inflammatory signaling cascades while promoting anti-inflammatory, M2-like, signaling, ultimately altering the default healing response in the CNS from tissue destruction and scarring toward positive tissue and ECM remodeling. While many processes are involved in preventing axonal remodeling, this dissertation will ultimately focus on the role of microglia and astrocytes after ocular injury and how ECM derived products can be utilized to ameliorate the initial immune response to preserve neuronal survival after injury.

1.3.1 Microglia response

Microglia are part of the innate immune response and act as the resident macrophages of the CNS, comprising ~10% of the adult brain [39, 40]. In addition to monitoring the microenvironment for signs of cellular damage, microglia are important regulators of synaptic pruning [41], oligodendrocyte differentiation [42], and neural precursor migration [43] during development. Microglia originate from primitive erythromyeloid progenitors in the yolk sac [44, 45] and populate the neuroepithelium early in development. During development, microglia proliferate and colonize the CNS, from where they mature into ramified microglia [46]. After birth, microglia proliferation rate decreases, and homeostasis is maintained with controlled apoptosis [47].

In an uninjured CNS, microglia remain in a resting, neuronal support state, assessing the surroundings for injury induced signals [48]. After injury, the expression of serum proteins,

cytokines, and abnormal neurotransmitters increases [49], thereby signaling microglia to adopt the classically activated, M1-like, pro-inflammatory phenotype. Microglia respond rapidly to injury induced factors, often within 30 minutes of injury [50, 51]. Once in the M1-like phenotype, microglia release inflammatory cytokines, including tumor necrosis factor 1-α (TNF-α), interleukin-6 (IL-6), interleukin-1β (IL-1β), interferon- γ (IFNγ), and chemokines [52] to recruit immune cells to the injury site and polarize the infiltrating cells to pro-inflammatory phenotypes. The M1-like microglia undergo a transition from a ramified resting-state cell to an amoeboid shaped phagocytic cell which engulfs debris, damaged cells, and microbes [53]. Recent studies showed microglia have a direct effect on astrocyte polarization by secreting TNF-α, IL-6, and complement protein 1q (C1-q) which polarizes astrocyte to the A1-like reactive astrocyte phenotype [38]. In conjunction with macrophages, microglia contribute to creating a pro-inflammatory environment by secreting nitric oxide (NO), superoxide, hydrogen peroxide, and reactive oxygen species (ROS) [54].

Microglia can also polarize to an alternatively activated, M2-like, anti-inflammatory phenotype [55]. M2-like microglia are induced by numerous factors, including IL-4, IL-10, and IL-13. The effect of the microglia phenotype on tissue remodeling has not been studied as extensively as the macrophage phenotype. However, M2-like macrophage polarization promotes functional tissue remodeling in non-CNS tissues [56, 57]. Macrophages and microglia polarize to one of three M2-like phenotypes, i.e. M2a, M2b, an M2c, based on their function [55, 58-60]. The M2a phenotype is induced by IL-4 and IL-13 and provides parasite resistance and suppresses inflammation by upregulating Arg1 expression and inhibiting NF-κB isoforms [61, 62]. The M2b phenotype is induced by immune complexes and stimulation of toll-like receptors (TLR) and is involved in immunoregulation [63]. The M2c phenotype is induced by IL-10, TGF- β, and

glucocorticoids and is involved in immunoregulation, tissue remodeling, and ECM deposition after injury [64]. Microglia are a versatile cell type and the phenotype and function of microglia depend factors in the micro-environment. Microglia phenotype are an early cellular factor in the immune response that sets the pro-inflammatory cascades in motion, therefore modulating the microglia phenotype can influence downstream inflammatory responses and tissue remodeling after injury.

1.3.2 Astrocyte response

Astrocytes are the most abundant cell type in the CNS. Astrocytes originate in the neuroectoderm and are divided into two main classes: protoplasmic astrocytes in the grey matter and fibrous astrocytes that reside in the white matter. In the CNS, astrocytes participate in numerous functions essential to neuronal health [65, 66], metabolism [67, 68], survival, and signaling [69]. During development, astrocytes form connections with neurons and other non-neuronal cells [70, 71]. In response to CNS injury or degeneration, astrocytes show a marked change in gene expression, hypertrophy, and proliferation [72, 73], in a process called reactive astrogliosis. Reactive astrogliosis can lead to several beneficial functions, including sequestration of damaged tissue and the buffering of excess cations and neurotransmitters [74-76]. However, these changes in astrocyte activity and gene expression also have negative consequences including exacerbation of tissue damage and glial scarring which inhibits axon regeneration [32]. These negative effects may be due to the over-production of reactive oxygen species and inflammatory cytokines as well as the release of extrinsic growth inhibitory factors [72, 77], which ultimately induce neuronal cell death after injury. Modulation of the astrocyte phenotype is therefore an important consideration in promoting neuronal survival after injury.

1.4 CURRENT APPROACHES TO OPTIC NERVE REGENERATION

Injuries to the mature CNS results in lifelong neurologic and functional loss. Ocular injuries can lead to irreversible vision loss and decrease the productivity, independence, and quality of life of affected individuals. Current treatment therapies include surgery to repair damaged tissues. However, no treatments currently exist that can increase neuronal survival and axonal growth after injury. Retinal ganglion cells (RGCs) have been shown to have the ability to extend axons *in vitro* and regenerate over short distances *in vivo* when cultured in optimal conditions. Embryonic RGCs have the intrinsic ability to regenerate. However, this ability is lost soon after birth [78], which is partially due to amacrine signaling inhibiting RGC growth [26]. Changes in gene expression are responsible for the lost intrinsic ability to promote rapid axonal growth [79, 80], and after birth RGCs only extend neurites by default when they receive peptide trophic factors that signal the cells to promote growth [81].

Several experimental strategies have been tested to promote retinal ganglion cell (RGC) regeneration after injury and some strategies have been successful in promoting partial RGC regeneration in the optic nerve [82, 83]. Injection of Zymosan causes RGCs to adopt an active growth state [84], and injecting CPT-cAMP in addition to Zymosan with inhibition of phosphatase and tensin homolog (PTEN) further enhances the regenerative ability of the RGC axons [85]. The Klf family has been associated with regulating axonal regeneration [86], with Klf-4 and -9 decreasing RGC axon growth and Klf-6 and -7 increasing RGC axon growth. Klf-4 deletion has been shown to promote axon regeneration after optic nerve injury [87], and studies have suggested Klf-4 deletion enhances CNTF-induced axon regeneration in both optic nerve crush and traumatic brain injury models [88]. Transcription factor STAT3 regulates functions that are important for axon regeneration, and mitochondrial STAT3 enhances bioenergetics that further potentiates

axonal regrowth [89]. The peripheral nervous system (PNS) has limited regenerative potential and STAT3 has been shown to be upregulated after injury. Upregulation of STAT3 in CNS has also been shown to promote neurite growth *in vivo* in mice [90]. Klf-4 interacts with STAT3 through cytokine induced phosphorylation and the binding suppresses STAT3 dependent gene expression [91], and deletion of Klf-4 *in vivo* therefore induces axon regeneration through the JAK-STAT3 signaling. Additionally, Wnt3a induces Wnt signaling in RGC which leads significant axonal regrowth past the lesion site after optic nerve injury, and the Wnt3a-induced axonal regeneration and RGC survival are associated with elevated activation of STAT3. Zinc (Zn) dysregulation in retina interneurons are partially responsible for why RGC axons don't regenerate after injury. Zn increases in the retinal amacrine cell processes within an hour after optic nerve injury and continues to rise over 24 hours, after which the Zn is transferred to the RCGs via vesicular release [92], and intravitreal injections of Zn chelators have been shown to increase RGC survival after injury. CNTF an RhoA have been shown to have additive effects that promote axon regeneration when used in conjunction with one another [93], and SOCS3 [94] and PTEN [95] deletion also increase axon regeneration potential and promote axon regrowth [96].

The aforementioned experimental therapies can induce long distance axon regrowth in mouse models of optic nerve injury. However, these multi-factorial approaches often include gene therapies of which down-stream effects are unclear. Although the approaches are not optimal and face clinical translation hurdles, these studies indicate RGC axons have the ability grow and remodel when presented with the correct factors.

1.5 EXTRACELLULAR MATRIX SCAFFOLDS

Redirecting the default immune response can be done by providing factors derived from the ECM that modulate the phenotypic transition of macrophages and T-helper cells from a pro-inflammatory to a pro-remodeling state. Regenerative medicine strategies using inductive biologic scaffolds composed of ECM have been successful in numerous pre-clinical and clinical studies. More than 8 million patients have been successfully treated with ECM bioscaffolds in a variety of clinical applications involving musculoskeletal, gastrointestinal, and urogenital tissues, among others [97]. Initial studies using ECM technology in nervous system tissues are also now showing encouraging results [98]. Extracellular matrix consists of the secreted structural and functional molecules of the resident cells of each tissue that define both cellular and tissue identity [97, 99]. ECM bioscaffolds are derived by decellularizing healthy tissues, typically xenogeneic (porcine) in origin, to decrease scarring and promote site-appropriate tissue repair in tissues the body cannot repair by default. ECM provides mechanical and biochemical support, facilitates intercellular communication, and modulates cellular and metabolic functions in a tissue-appropriate manner [100]. When prepared properly, ECM is a tunable biocompatible platform that can be derived from numerous tissue sources and used in various forms, including powders [101], sheets [102], and injectable hydrogels [103], which can all be further tuned mechanically and biochemically based on the nature and severity of the injury [104].

Though the specific mechanisms by which ECM derived factors influence cell and tissue remodeling are only partially understood, ECM bioscaffolds are known to promote an anti-inflammatory, reparative, M2-like macrophage phenotype, recruit endogenous stem and progenitor cells and promote their differentiation in a site-appropriate manner, and mitigate scar

tissue formation [105-108]. Specifically, ECM is hypothesized to increase anti-inflammatory signaling at the injury site by increasing the M2/M1 macrophage ratio [109]. A low ratio M2/M1 is suggested to promote inflammation and scarring, whereas a high M2/M1 ratio appears to promote positive tissue remodeling [57, 105]. ECM appears to increase the M2/M1 macrophage ratio, in part, by releasing protein degradation products, termed matricryptic peptides [110], as infiltrating immune system cells degrade ECM bioscaffolds. In addition to modulating the innate immune response, matricryptic peptides are hypothesized to regulate several components of the healing response, either directly or indirectly, including angiogenesis [111], stem cell recruitment and differentiation [110], and neurogenesis [112], with ECM from younger, homologous tissues often being more effective [113-115], like fetal heart [116] and kidney [117]. Macrophages polarized toward an alternatively activated, M2-like, phenotype secrete cytokines and neurotrophic factors, and express cell-surface markers consistent with antigen-presenting activity, indicating ECM bioscaffolds have the potential to influence nerve, immune, and glial cell activities by modulating macrophage phenotypes. In agreement with this idea, pre-clinical studies suggest ECM bioscaffolds can promote positive tissue remodeling in rodent CNS injury models.

1.5.1.1 Matrix bound nanovesicles

MBV are nano-sized lipid bound bodies embedded securely within the extracellular matrix, are distinct and separate from exosomes, and represent a significant vertical advance in understanding tissue homeostasis and cellular function. Emerging evidence shows MBV release during ECM scaffold degradation is critical to promoting reparative, anti-inflammatory macrophage phenotypes [108]. MBV are nanometer-sized, membranous vesicles similar in size and structure to exosomes, but distinct with respect to cargo, surface markers, and compartmentalization. Whereas exosomes primarily exist in body fluids, MBV are localized to the collagen fibrils within all experimental

and commercial ECM bioscaffolds analyzed to date [118]. MBV are highly stable and protect biologically active signaling cargo, including miRNAs and proteins, from degradation [118, 119]. These MBV survive even harsh ECM decellularization processes and thus likely play a fundamental role in tissue and organ organization across species and a regulatory role in the tissue response to injury. Recognition of their presence and an understanding of their biologic activity provides for possible new therapeutic approaches that are otherwise untenable. Derived from healthy, pro-regenerative tissues, MBV have biologic potential that exceeds that of extracellular vesicles derived from cultured cell lines. MBV are plentiful, lyophilizable, highly stable, and easily incorporated into injury-specific platforms like dressings, injections, or gels. MBV stability and adaptability make them easily customizable for therapeutic platforms appropriate to the nature and to the severity of the injury.

MBV can recapitulate effects of the ECM bioscaffolds from which they were derived and these effects appear to depend on MBV miRNA cargo [120]. MBV carry unique (i.e. tissue specific) and complex cargo, including miRNAs, lipids, proteins, cytokines, carbohydrates, and other small molecules, capable of activating a variety of extra- and intracellular signaling pathways. Initial studies indicate that the cellular response to MBV depends on both surface proteins and the intra-luminal miRNA cargo [121]. Interestingly, miRNA cargo in MBV, derived from different tissues, are enriched in highly conserved miRNAs involved in cell cycle regulation and differentiation [121, 122], suggesting MBV play a fundamental role in ECM mediated tissue and organ development, organization, and function, possibly by regulating cellular phenotypes in a site appropriate manner. Small RNQ sequencing RNA-seq identified known and novel candidate miRNA packaged within MBV [118], and showed a differential miRNA signature dependent on the anatomical origin of the source tissue. Moreover, a cohort of miRNAs known to regulate

neuronal signaling pathways involved in neuronal differentiation and neurite growth, including miRNAs -30b, -125b, and -133b [123-125], were identified to be highly enriched in MBV. These results indicate MBV contain bioactive components able to regulate cellular function and have the potential to regulate and promote CNS tissue remodeling after injury.

1.6 SPECIFIC AIMS

Specific Aim 1: After traumatic optic neuropathy, to determine if diffusion tensor imaging (DTIMRI), manganese-enhanced MRI (MEMRI), and optokinetics can predict changes in the rate of retinal ganglion cell axon degeneration that predict changes in visual behavior

Hypothesis: After acute optic neuropathy, non-invasive, longitudinal MRI and behavioral studies can predict changes in RGC axon integrity along the visual pathway, axonal transport, and visual function

Specific Aim 2: To determine if tissue-specific ECMs differentially modulate the default healing response in the CNS

Hypothesis: Aim 2a tests the hypothesis CNS specific, brain derived ECM will increase RGC survival and neurite growth *in vitro*

Hypothesis: Aim 2b tests the hypothesis that CNS specific brain ECM will increase RGC axon survival and growth and decrease astrocyte activation *in vivo*

Specific Aim 3: To determine if matrix bound nanovesicles (MBV) recapitulate ECM mediated changes in the default healing response

Hypothesis: Aim 3 tests the hypothesis that MBV will increase RGC axon growth *in vitro*, and RGC survival and function *in vivo* as detected by immunohistochemistry and electroretinography (ERG)

1.6.1 Impact of specific aims

Ocular injuries resulting in blindness remain a persistent problem, yet little is known about axonal degradation progression and there is currently no off the shelf, easily administered product to provide neuroprotection and promote neuro-regeneration after injury. As a result, patients are relegated to a life of diminished productivity and a compromised quality of life. Imaging modalities allow us to probe the progression of white matter degeneration after injury, which is the first step to understanding the effects of injury on the visual system, as well as the effects of proposed therapeutics applied to injured ocular tissue. ECM-based medical technology continues to drive innovation from both a scientific and clinical perspective. Recently discovered MBV are an excellent example of such advancements and provide many opportunities for investigating signaling mechanisms by which tissue remodeling occurs during health and following injury in the adult mammalian CNS. The proposed minimally invasive MBV treatment has the very real possibility to preserve visual function in injured patients. The MBV treatment can be delivered intravitreally; therefore, requires no invasive surgical procedure and can be administered immediately after injury. In addition to treating ocular injuries, the MBV therapy may have benefit for other CNS injuries such as traumatic brain and spinal cord injuries, and this therapeutic approach applies to soldiers and civilians alike

2.0 CITICOLINE AMELIORATES THE NEUROBEHAVIORAL EFFECTS OF INTRAOCULAR PRESSURE ELEVATION ON THE VISUAL SYSTEM

2.1 INTRODUCTION

Glaucoma is a neurodegenerative disease of the visual system that involves progressive retinal ganglion cell death, optic nerve damage, and irreversible vision loss [126-129]. Glaucoma is the second leading cause of blindness worldwide; 60 million people are estimated to have glaucoma, with 8.4 million legally blind [130, 131]. One major risk factor for glaucoma is an increase in intraocular pressure (IOP). However, the direct causes of glaucoma are unknown, and how different degrees of IOP elevation affect glaucoma pathogenesis remains unclear. In addition, currently, the only clinically proven way to slow down the progression of glaucoma is decreasing IOP, yet neurodegeneration of the visual system may still occur after lowering IOP to population-derived normal levels [132, 133]. Therefore, there exists a need for a better understanding of glaucoma mechanisms resulting from IOP elevation, as well as a treatment mechanism beyond lowering IOP that can further slow the progression of the disease or decrease the severity of damage to the visual system to preserve or restore visual function.

To determine the pathophysiological mechanisms of glaucoma disease progression, several animal models have been developed targeting different aspects of IOP elevation-induced pathogenesis [134, 135]. However, because of limited methods available to probe eye-brain, and visual behavior relationships *in vivo* and simultaneously, these studies were mainly performed *ex vivo,* and the longitudinal effects of different degrees of IOP elevation on the structural and functional integrity of the visual system remain unclear. Recent studies also suggest that glaucoma

may not only involve the eye, but also the brain in a trans-synaptic manner [136, 137]. However, results remain controversial partly because of small samples [138], and there are barriers to determine if the brain can be the target for glaucoma therapeutics apart from the eye. Development of a well-controlled, *in vivo* model system for longitudinal neurobehavioral analyses may help clarify mechanisms affecting vision loss in glaucoma patients and provide a platform to evaluate the efficacy of proposed glaucoma treatments. Therefore, in this study, we combined the use of experimental glaucoma models, optokinetics, and advanced structural and functional magnetic resonance imaging (MRI) techniques to analyze the effects of acute and chronic IOP elevation on visuomotor behavior response, white matter integrity, axonal transport, and functional connectivity between visual brain nuclei over time. We hypothesize that different degrees of IOP elevation may induce different extents of structural and functional brain changes and behavioral outcomes. To explore treatment mechanisms that can reduce glaucomatous damage independent of IOP reduction, one may postulate candidate strategies that can act to preserve neural tissues, promote neurorepair, and reduce functional loss across other neurodegenerative diseases and injuries. Among these candidates, citicoline is an endogenous compound that has been suggested to slow down the detrimental effects of Alzheimer's disease [139], traumatic brain injury [140], multiple sclerosis [141] and cerebral ischemia [142] when administered exogenously. Citicoline (cytidine 5'-diphosphocoline) is a non-toxic [143], endogenous compound that plays important roles in cell membrane lipid synthesis and repair and phospholipid degradation inhibition [144], Citicoline increases certain neurotransmitters such as dopamine (by enhancing tyrosine hydroxylase activity and inhibiting dopamine reuptake), noradrenaline, and serotonin; and serves as a choline donor in the biosynthesis of acetylcholine [145, 146]. The effects of citicoline on glaucomatous neurodegeneration remain unclear. After oral ingestion, citicoline is hydrolyzed in

the intestinal wall and liver to choline and cytidine, where both compounds are rapidly absorbed, enter systemic circulation, cross the blood-brain barrier, and enter the central nervous system [147]. Therefore, in this study, we hypothesize that oral citicoline treatment can ameliorate the effects of IOP elevation on glaucomatous damage and functional deterioration in the visual system.

By using non-invasive multi-parametric MRI and behavioral studies, association can be made between the degree of IOP elevation and longitudinal structural and functional changes in the visual system after experimental glaucoma induction and oral citicoline treatment. In this study, we used diffusion tensor imaging (DTI) to characterize microstructural fiber organization along the visual pathway by measuring water diffusion patterns in white matter compartments [7]. Specifically, DTI-derived parameters, including fractional anisotropy (FA; sensitive to overall microstructural integrity), axial diffusivity ($\lambda_{//}$; sensitive to axonal integrity), and radial diffusivity ($\lambda_{\perp}$; sensitive to myelin integrity [148, 149]) were used to assess the resultant structural integrity of the visual pathway after IOP elevation and oral treatment. We also used magnetization transfer ratio from magnetization transfer imaging (MTI) to examine changes in macromolecular structures, including myelin, by measuring the magnetization transfer between water bound to macromolecules and the surrounding free water [9] in the optic nerve. Manganese (Mn) ions can offer positive T1-weighted MRI contrast enhancement and act as a calcium analogue that enters calcium channels and be actively transported anterogradely along axonal pathways via microtubules [18, 19]. Therefore, Mn-enhanced MRI (MEMRI) was used to provide information regarding anterograde transport and the integrity of the axonal pathway after IOP elevation and oral treatment. Last but not least, resting-state functional connectivity MRI (RSfcMRI) was used to explore the functional connectivity (FC) between brain regions throughout the visual system [150]. These multi-parametric brain MRI findings were examined alongside optokinetic and

histological assessments, to determine how different magnitudes and durations of IOP elevation affected neurobehavioral outcomes with and without oral citicoline treatment.

2.2 MATERIALS AND METHODS

2.2.1 Experimental paradigm

Eighty-two adult female Long Evans rats (Charles River Laboratories, Wilmington, MA) at about 8 weeks old were used in this study. They were housed in a 12 hr light/dark cycle with rat chow and water available *ad libitum*. Animals from each of the acute IOP elevation, chronic IOP elevation and sham control groups received neurobehavioral assessments using optokinetics (days 0, 7, 14, and 35), DTI (days 3, 7, 14, and 35), MTI (days 3, 7, 14, and 35), RSfcMRI (day 35), MEMRI (day 35), and histology (day 35) (Figure 1A). Additionally, a subset of the animals with chronic IOP elevation received oral doses of citicoline daily for 7 days prior to IOP elevation induction, and every 48 hours for 14 days after IOP elevation induction. The acute groups had their IOP measured during experimental induction, whereas the chronic groups had their IOP measured at days 3, 7, 14, and 35 to verify that the IOP remained elevated for the duration of the experimental period. All experiments were approved by the University of Pittsburgh Institutional Animal Care and Use Committee, and investigators followed guidelines from the Association for Research in Vision and Ophthalmology's statement for Use of Animals in Ophthalmic and Vision Research

2.2.2 Anesthesia

Animals were anesthetized via isoflurane inhalation (3% induction, 1.5% maintenance) for all chronic IOP elevation induction, MR imaging procedures, and Mn contrast agent injections. For acute IOP elevation induction, rats were anesthetized with an intraperitoneal injection of 75:10 mg/kg ketamine/xylazine cocktail (Henry Schein, NY). All procedures were performed under sterile conditions, and rat body temperature was maintained and monitored using a circulating water blanket and a rectal thermometer. After experiments, animals were placed on a heating pad for recovery and monitored until fully conscious and ambulating.

2.2.3 Acute IOP elevation induction

Twenty-five animals received mild (n=13) or severe (n=12) acute IOP elevation in the right eye via physiological saline anterior chamber perfusion. The left eye remained untreated and served as an internal control. Proparacaine hydrochloride ophthalmic solution (Bausch & Lomb, Inc., Rochester, NY, USA) and tropicamide ophthalmic solution (Akorn, Lake Forest, IL) were topically applied to the right eye to induce analgesia and pupil dilation, respectively. A 30-gauge needle was connected to a sterile saline reservoir (0.9% sodium chloride; Baxter International Inc., Deerfield, IL, USA) via sterile tubing. The needle tip was inserted into the right eye's anterior chamber under a surgical microscope, parallel to the iris, taking care not to touch the iris or lens. Once inserted, the needle was secured in place to avoid movement during the experiment. IOP was elevated to 40 mmHg and 130 mmHg for mild and severe acute IOP elevation, respectively, by elevating the saline reservoir to the appropriate height. The reservoir was secured in place for 60 min and IOP was measured with both a handheld tonometer (Icare TonoLab,

Finland) and a pressure transducer (BIOPAC Systems, Goleta, CA, USA) connected in line with sterile tubing. Afterwards, the reservoir was lowered, and the needle removed from the anterior chamber. Antibiotic ointment (Gentamicin, Akorn, Lake Forest, IL) was applied topically immediately after removal of the needle. Sham procedures (n=9) were performed by cannulating the right eye as described and keeping the saline reservoir at eye level for 60 min.

2.2.4 Chronic IOP elevation induction

Thirty-eight animals received an intracameral injection of an optically clear cross-linking hydrogel to the right eye to induce chronic IOP elevation. The left eye remained untreated and served as an internal control. Proparacaine and tropicamide were first topically applied to the right eye to induce analgesia and pupil dilation. The right eye was injected intracamerally with 15 µl of a 1:1 mixture of 4% vinyl sulfonated hyaluronic acid and 4% thiolated hyaluronic acid [151]. The injections were performed under a surgical microscope with a microinjection system through a glass micropipette (World Precision Instruments, Sarasota, FL, USA). The solidified hydrogel obstructed aqueous outflow, thereby causing a sustained increase in IOP. Antibiotic ointment was applied topically immediately after injection. Sham procedures were performed on 10 animals by injecting only the buffer solution into the right anterior chamber. IOP was measured with the handheld TonoLab tonometer at days 3, 7, 14, and 35 after hydrogel injection to verify that the IOP elevation was sustained.

2.2.5 Citicoline administration

Among the 38 animals that received chronic IOP elevation induction, 19 of them also received daily citicoline treatment (500 mg/kg; Jarrow Formulas, Los Angeles, CA) via oral gavage for 7 days prior to chronic IOP elevation induction, and every 48 hours for 14 days after chronic IOP elevation induction. Citicoline was freshly diluted in saline before each treatment.

2.2.6 Optokinetics

The OptoMotry virtual-reality optokinetic system (CerebralMechanics Inc., Lethbride, Alberta, Canada) [152, 153] was used to assess visuomotor behavior by quantifying the visual acuity of each eye. Prior to data collection, animals were acclimated to the system once per day for three days. Acclimation sessions lasted 20 min during which the animals were exposed to stimuli similar to those presented during data collection. During data collection, spatial frequency ranged from 0.042 to 0.750 cycles/degree using a simple staircase method while rotation speed (0.12 degrees/s) and 100% contrast were maintained throughout the experiment.

2.2.7 MRI Protocols

All MR imaging was performed using a 9.4-Tesla/31-cm Varian/Agilent horizontal MRI scanner (Santa Clara, CA, USA) with a 38 mm diameter transmit-receive volume coil and a receive surface coil.

DTI was acquired for all animals using a fast spin-echo sequence with 12 diffusion gradient directions at b = 1.0 ms/μm^2 and 2 non-diffusion-weighted images at b = 0 ms/μm^2 (b_0).

Other imaging parameters included: repetition time/echo time (TR/TE)= 2300/27.8 ms, echo train length=8, diffusion gradient duration time (δ)/diffusion gradient separation time (Δ) = 5/17 ms, number of repetitions = 4, field of view = 2.6 x 2.6 cm^2, acquisition matrix = 192 x 192 (zero-filled to 256 × 256), number of slices = 20, and slice thickness = 1 mm. Slices were oriented orthogonal to the prechiasmatic optic nerves.

MTI was acquired for all animals at the level of the prechiasmatic optic nerves at the same orientation and the same time points as DTI with 9.5 μT saturation pulses at 4000 Hz off-resonance. Other parameters included: TR/TE = 1500/8.43 ms, echo train length = 8, number of repetitions = 2, field of view = 2.6 x 2.6 cm^2, acquisition matrix = 192 x 192 (zero-filled to 256 × 256), number of slices = 1, and slice thickness = 1 mm.

MEMRI was done on a randomly selected subset of the mild acute IOP elevation (n = 9), severe acute IOP elevation (n = 9), acute sham control (n = 6), untreated chronic IOP elevation (n = 12), citicoline-treated chronic IOP elevation (n = 13), and chronic sham control (n = 6) groups. After all imaging and behavioral studies were completed, each animal received binocular intravitreal injections of 1.5 μL of 100 mM manganese chloride ($MnCl_2$). T1-weighted images were acquired before and at 8 hr after $MnCl_2$ injections with a fast spin-echo sequence. The same geometric parameters were used as for DTI, with TR/TE = 600/8 ms, echo train length = 8, number of slices = 8 and slice thickness = 1 mm. A saline syringe phantom was placed next to the rat head for signal normalization to account for potential system instability between imaging sessions.

For RSfcMRI, T2-weighted images were first acquired with the following parameters to serve as an anatomical reference: TR/TE = 4000/36 ms, echo train length = 8, field of view = 2.6 x 2.6 cm^2, acquisition matrix = 192 x 192 (zero-filled to 256 × 256), number of slices = 6, and slice

thickness = 1 mm. For RSfcMRI, a single-shot gradient-echo echo-planar imaging sequence with 420 repetitions was used for session. Each session resulted in 14 min of scan time, and 4 sessions were acquired per animal, resulting in approximately 1 hr of total scan time per animal. Other parameters included: TR/TE = 2000/18 ms, field of view = 32 x 32 mm^2, acquisition matrix = 64 x 64, number of slices = 6, and slice thickness = 1 mm.

2.2.8 Histology

Animals not receiving Mn injection were sacrificed at the terminal point and used for histology. They were euthanized with an intraperitoneal injection of pentobarbital (50 mg/kg) and whole-body perfusion was used to fix the tissue for histology. When the animals no longer responded to a toe pinch, they were perfused with phosphate buffered saline (PBS) at pH 7.4, followed by 4% paraformaldehyde in PBS. Optic nerves were harvested and fixed for an additional 48 hours in 4% paraformaldehyde in PBS at 4ºC. Samples were placed in 30% sucrose for cryoprotection, and then embedded in optical cutting temperature medium. The optic nerves were sectioned into 10μm thick sections, placed on histology slides, and kept at -20ºC until use.

Sections were stained for phosphorylated neurofilament (pNF) (1:1000, Covance, NJ, USA) and myelin basic protein (MBP) (1:50, Santa Cruz Biotechnology, TX, USA). The sections were washed three times with PBS and blocked and permeabilized overnight with 0.2% Triton X-100, 1% bovine serum albumin (BSA), and 5% donkey serum in PBS. pNF and MBP primary antibodies were diluted to working concentrations in 1% BSA and 5% donkey serum in PBS and incubated for 3 days at 4ºC. The sections were washed three times in PBS and incubated with secondary antibodies (1:500 donkey anti-goat Alexa488 for MBP, 1:500 donkey anti-mouse Alexa546 for pNF) in 1% BSA in PBS for 2 hr at room temperature. Sections were rinsed in PBS,

stained with 4′,6-Diamidino-2-phenylindole (DAPI), and imaged with a confocal microscope (Olympus Fluoview1000, Tokyo, Japan) at 60X magnification with the same exposure times used across sections for each antibody.

2.2.9 Data analysis

For DTI, SPM8 (Wellcome Department of Imaging Neuroscience, University College, London, UK) was used for co-registration between diffusion-weighted and non-diffusion-weighted images. 3 x 3 diffusion tensors were placed on non-diffusion-weighted and diffusion-weighted images on a pixel-by-pixel basis using DTIStudio v3.02 (Johns Hopkins University, Baltimore, MD). DTI parametric maps including fractional anisotropy (FA), axial diffusivity ($\lambda_{//}$) and radial diffusivity ($\lambda_{\perp}$) maps were computed using eigenvectors and eigenvalues in DTIStudio. Regions of interest (ROIs) were drawn manually using ImageJ v1.47 (Wayne Rasband, NIH, USA) at the prechiasmatic optic nerves at Bregma 1.5 mm, and the optic tracts at Bregma -3.5 mm based on the FA directionality map, FA value map, $\lambda_{//}$ and $\lambda_{\perp}$ maps and the rat brain atlas [154]. The corresponding DTI parametric values were then extracted. As more than 90% of the optic nerve fibers in adult rodents decussate at the optic chiasm to the contralateral optic tract [155], The visual pathway projected from the injured right eye (right optic nerve and left optic tract) was assessed relative to that projected from the uninjured left eye (left optic nerve and right optic tract), followed by between-group comparisons over time.

For MTI, the magnetization transfer ratio (MTR) for the prechiasmatic optic nerve was calculated as $MTR = (M_0-M_{sat})/M_0$, where M_{sat} represents the magnetization signal with saturation pulse, and M_0 represents the magnetization signal without saturation pulse. ROIs were

manually drawn on the prechiasmatic optic nerve based on MTR maps and the rat brain atlas and quantified using ImageJ.

For MEMRI, T1-weighted signal intensities in the left and right optic nerves, lateral geniculate nuclei (LGN), and superior colliculi (SC) were measured using manual ROI drawing in ImageJ. Signal intensities were normalized to the nearby saline phantom to counter for system instability between imaging sessions. Differences in Mn enhancement between injured and uninjured visual pathways were quantified by calculating the percentage difference in normalized T1-weighted signal intensities in the right optic nerve, left LGN and left SC relative to the left optic nerve, right LGN and right SC, respectively.

For IOP, optokinetics and MRI (except RSfcMRI) assessments, all results are presented as mean ± standard error of mean (SEM). ANOVA was used in conjunction with a Tukey's post-hoc test to determine significance between groups using GraphPad Prism v5.00 (GraphPad Software Inc., La Jolla, CA, USA). Results were considered significant when $p < 0.05$.

For RSfcMRI, images were realigned to the first volume to account for small head motions using a 3 degree-of-freedom rigid body transformation (translations in the imaging plane and rotations about the slice direction). The images were then smoothed with a 2D Gaussian function with a standard deviation of 2 voxels, followed by a temporal ideal bandpass filter with cutoff frequencies of 0.01 and 0.1 Hz. Finally, the effects of motion were regressed out of the signal using the motion parameters estimated during realignment, as well as the first and second order temporal derivatives of the motion parameters. Before this regression step, the motion parameters were also temporally filtered as above to avoid the reintroduction of high-frequency noise into the preprocessed data. ROIs were drawn manually on the LGN, SC, and visual cortex (VC) in each hemisphere, beginning with the first run of data for each animal and then propagated to all

remaining runs by performing a 3-degree-of-freedom transformation between the first image of each pair of runs, thereafter applying this transformation to the drawn ROIs. Functional connectivity (FC) in each run was then summarized by computing the mean time course in each region, computing the Pearson correlation between each pair of time courses, and converting these correlation coefficients to z-score using the Fisher r-to-z transformation. In this way, each run of data was summarized by a graph where the ROIs define the nodes and the strength of the correlation between a given pair of ROIs defines the edges. For each edge in the graph, effects for group-wise differences were investigated using a linear mixed-effects model with random slopes and intercepts included for each animal. An F-test was done on each group and a false discovery rate corrected $Q<0.05$ considered significant. Where the F-tests were significant, post-hoc testing was performed with the same model but with data restricted to the two groups being compared.

2.3 RESULTS

2.3.1 IOP was elevated to different magnitudes and durations and was unaffected by citicoline treatment

A schematic of the experimental plan is provided in Figure 1. In brief, eighty-two adult female Long Evans rats were randomly assigned to one of six IOP elevation groups. In the acute IOP elevation groups, animals received mild elevated IOP at 40 mmHg (n=13), or severe elevate IOP at 130 mmHg (n=12), or normal physiological IOP of approximately 15 mmHg as a sham control (n=9) via anterior chamber perfusion to the right eye for 1 hour. In the chronic IOP elevation groups, IOP was elevated to about 30 mmHg sustainably for 5 weeks via intracameral injection

of an optically clear, crosslinking hydrogel into the right eye. Nineteen animals with chronic IOP elevation did not receive any oral treatment (n=19), whereas another 19 animals with chronic IOP elevation received daily citicoline treatment via oral gavage for 7 days prior to IOP elevation induction, and every 48 hours for 14 days after IOP elevation induction (n=19). Another batch of animals received sham procedures by intracameral buffer solution injection without oral treatment (n=10). Optokinetics, DTI and MTI were performed longitudinally over the experimental period of 5 weeks after IOP elevation induction, whereas RSfcMRI, MEMRI and histology were performed at the end experimental time point.

2.3.2 Acute and chronic IOP elevation decreased visual acuity, whereas oral citicoline treatment increased visual acuity in the experimental eyes

For the acute IOP elevation groups, the target IOP level was confirmed with both a handheld tonometer (Icare Tonolab, Finland) and a pressure transducer (BIOPAC Systems, Goleta, CA, USA) connected in line with sterile tubing during anterior chamber perfusion (Figure 2A). The same hand-held tonometer was used to confirm successful induction of chronic IOP elevation. As shown in Figure 2B, intracameral hydrogel injection to the right eye significantly elevated IOP for the duration of the experimental period, with no significant IOP difference between citicoline-treated and untreated animals. In both citicoline-treated and untreated groups, the IOP of the right eye steadily increased from day 3 to day 14 and remained unchanged from day 14 to day 35. The left uninjured eye of the experimental groups, as well as both eyes of the sham group, remained unchanged in terms of IOP over the experimental period.

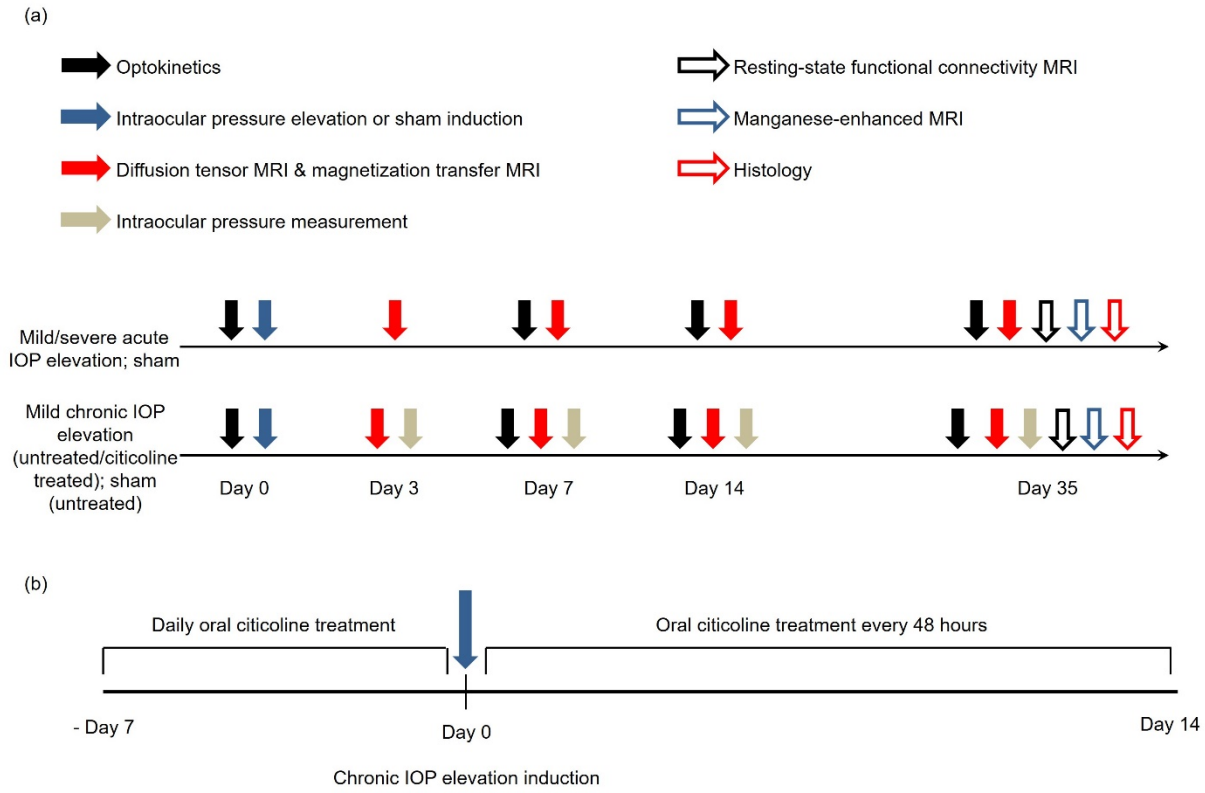

Figure 1. A. Experimental timeline for measuring eye, brain, and behavioral changes following acute and chronic intraocular pressure (IOP) elevation across 5 weeks. B. Treatment paradigm for oral citicoline administration. A subgroup of animals in the chronic IOP elevation group received oral citicoline treatment at a concentration of 500 mg citicoline/ kg of the animal. Animals received daily citicoline administration for 7 days prior to IOP elevation induction, and every 48 hours for 14 days following chronic IOP elevation induction.

Using optokinetic behavioral assessments, the visual acuity of the left, uninjured eye in all acute and chronic groups was found to remain unchanged over time and was comparable with the right experimental eye before IOP elevation (Figure 2C-D). The visual acuity of the right experimental eye under both mild and severe acute IOP elevation significantly decreased from pre-injury (day 0) to day 7 and continued to be significantly lower than the visual acuity of the left eye at days

14 and 35 (Figure 2C). At days 7, 14, and 35, the right experimental eye had a significantly lower visual acuity under severe acute IOP elevation than mild acute IOP elevation (Figure 2C).

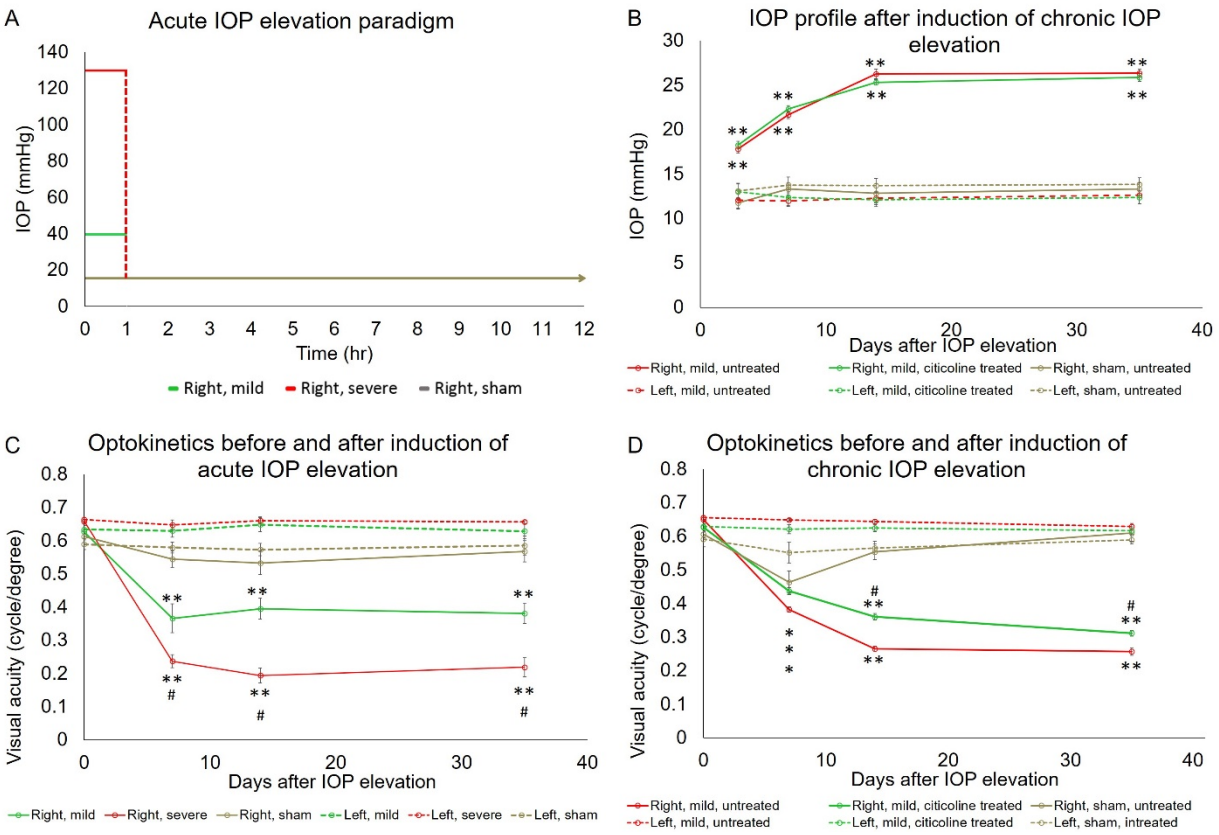

Figure 2. Intraocular pressure (IOP) profiles (a & b) and visual acuity (VA) (c & d) in acute and chronic animals. a. Anterior chamber perfusion elevated IOP transiently for one hour, after which IOP returned to baseline at ~15mmHg. b. Hydrogel injection to the right eye significantly elevated IOP in all animals for the duration of the experimental period. c. By day 7, the VA of the right eyes of the mild and severe groups were significantly decreased compared to the left eyes, and this persisted at days 14 and 35. d. The VA of the right eyes of both citicoline-treated and untreated animals became worse starting at day 7. The worsening of VA in the right eyes appeared significantly slower for the citicoline-treated group compared to the untreated group.

The right eye in both chronic IOP elevation groups and the chronic sham control group showed a significant visual acuity decrease from day 0 to day 7 (Figure 2D). By day 14, the right eye of the sham group had apparently recovered, and there was no visual acuity difference between left and right eyes at days 14 and 35. In contrast, the right eye of both citicoline-treated and untreated groups showed a persistent visual acuity decrease at days 14 and 35 after chronic IOP elevation. However, under similar levels of chronic IOP elevation, the treated group had a significantly higher visual acuity in the right experimental eye than the untreated group at days 14 and 35 (Figure 2D).

2.3.3 IOP elevation decreased fractional anisotropy and increased radial diffusivity along the visual pathway in diffusion tensor MRI, while citicoline treatment ameliorated such effects

Fractional anisotropy, radial diffusivity, and axial diffusivity were calculated as percentage change between injured (right) and uninjured (left) visual pathways. When examining the structural integrity of the visual pathway using longitudinal DTI (Figures 3-4), among the acute groups (Figure 3), the fractional anisotropy in the optic nerve was significantly lower at day 35 after severe acute IOP elevation compared to sham procedures (Figure 3B). Fractional anisotropy in the optic tract also showed a similar but statistically insignificant trend (Figure 3E), whereas radial diffusivity in the optic nerve was significantly higher at day 35 after severe acute IOP elevation compared to the sham control (Figure 3D). Over the time course, significant progression

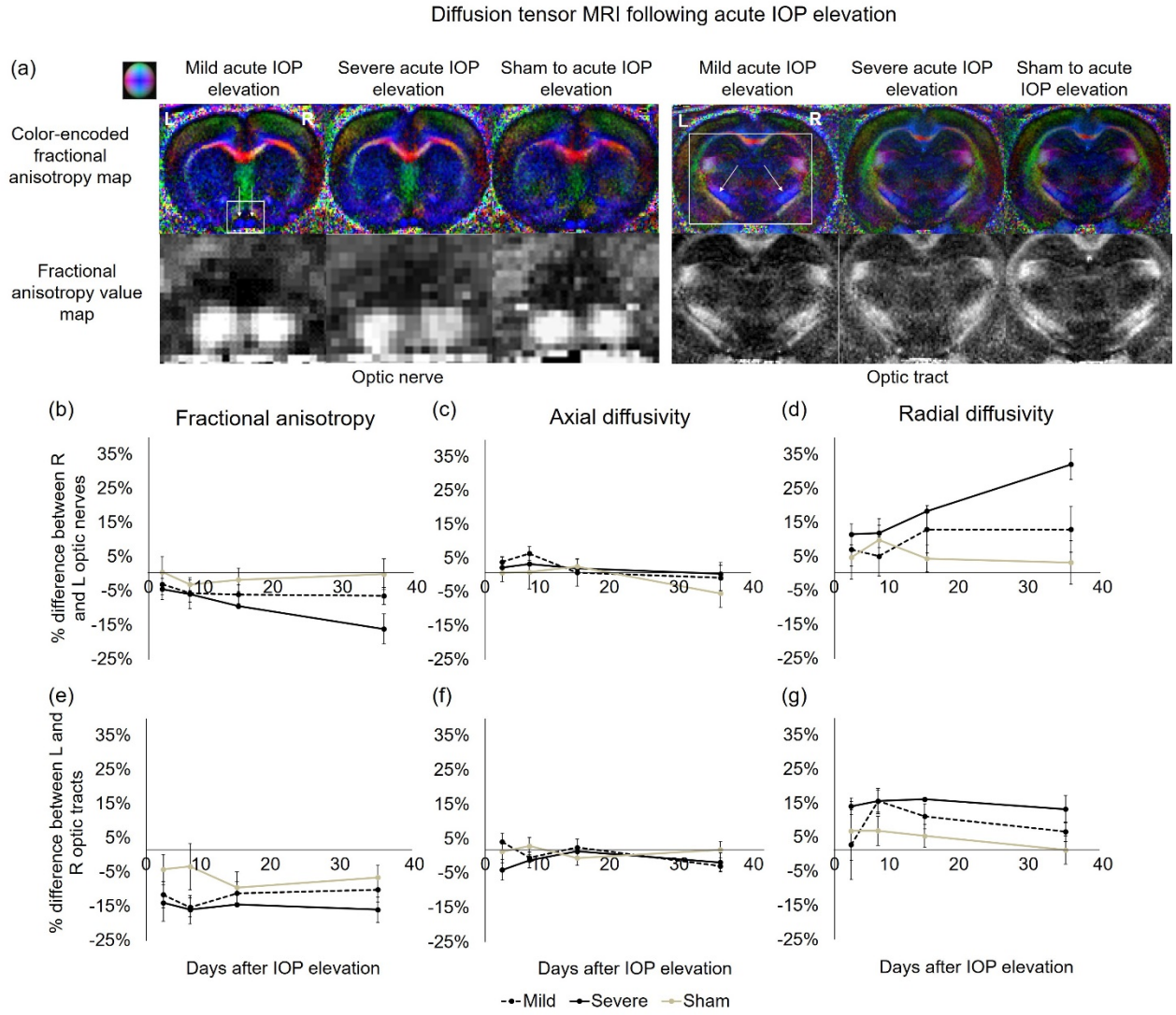

Figure 3. A. Representative fractional anisotropy (FA) color and value maps in the optic nerve and optic tract in mild, severe, and sham injury animals. B. There were significant differences in FA and RD in the optic nerves at day 35 between the severe group and sham injury

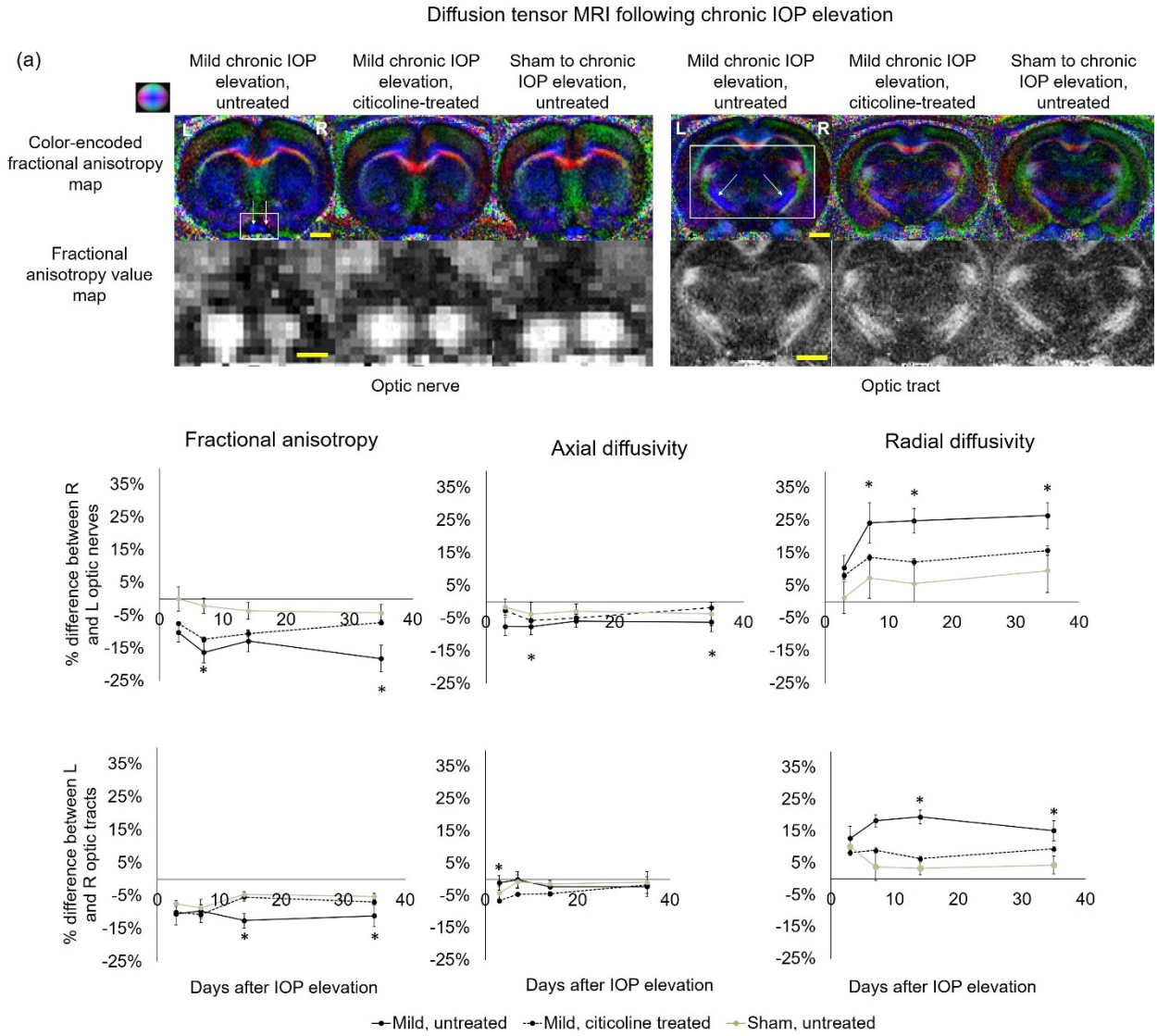

Figure 4. A. Representative fractional anisotropy (FA) color and value maps in the optic nerve and optic tract in untreated, citicoline treated, and sham injury (untreated) animals. B. There were significant differences in FA, AD, and RD between groups in the optic nerve and optic tract.

in fractional anisotropy decrease and radial diffusivity increase were observed within severe acute IOP elevation group when comparing days 3 and 7 to day 35.

Among the chronic groups (Figure 4), the optic nerve showed a significantly lower fractional anisotropy at days 7 and 35 after untreated chronic IOP elevation when compared to the sham control (Figure 4B), while the fractional anisotropy in the optic tract was significantly lower at days 14 and 35 after untreated chronic IOP elevation compared to citicoline-treated chronic IOP elevation (Figure 4E). The axial diffusivity in the optic nerve of the untreated chronic IOP elevation group was significantly lower at days 7 and 35 compared to the sham group (Figure 4C), while the optic tract of the untreated chronic IOP elevation group showed a significantly lower axial diffusivity at day 3 compared to the sham group (Figure 4F). The radial diffusivity in the optic nerve was significantly higher at days 7, 14, and 35 after untreated chronic IOP elevation compared to the sham control (Figure 4D), while the radial diffusivity in the optic tract was significantly higher at days 14 and 35 after untreated chronic IOP elevation compared to the sham control (Figure 4G). No significant difference in DTI parametric value was observed between citicoline-treated chronic IOP elevation and sham control groups along the visual pathway (Figure 4B-G).

2.3.4 IOP elevation decreased magnetization transfer ratio in the optic nerve, which was ameliorated by citicoline treatment

Magnetization ratio was calculated as percentage change between injured (right) and uninjured (left) visual pathways. Among the acute groups (Figures 5A), the prechiasmatic optic nerve showed an early decline in magnetization transfer ratio at day 3 after severe acute IOP elevation. Such decline was significantly larger than both the mild acute IOP elevation and sham control

groups. The magnetization transfer ratio in the severe acute IOP elevation group remained significantly lower than the sham control group till the end experimental time point at day 35. Among the chronic groups (Figures 5B), the magnetization transfer ratio in the optic nerve was significantly lower after chronic IOP elevation without citicoline treatment when compared to that with citicoline treatment at both days 14 and 35, while the magnetization transfer ratio between untreated chronic IOP elevation and sham control groups was significantly different at day 35. No significant difference in magnetization transfer ratio was observed between citicoline-treated chronic IOP elevation and sham control groups in the optic nerve.

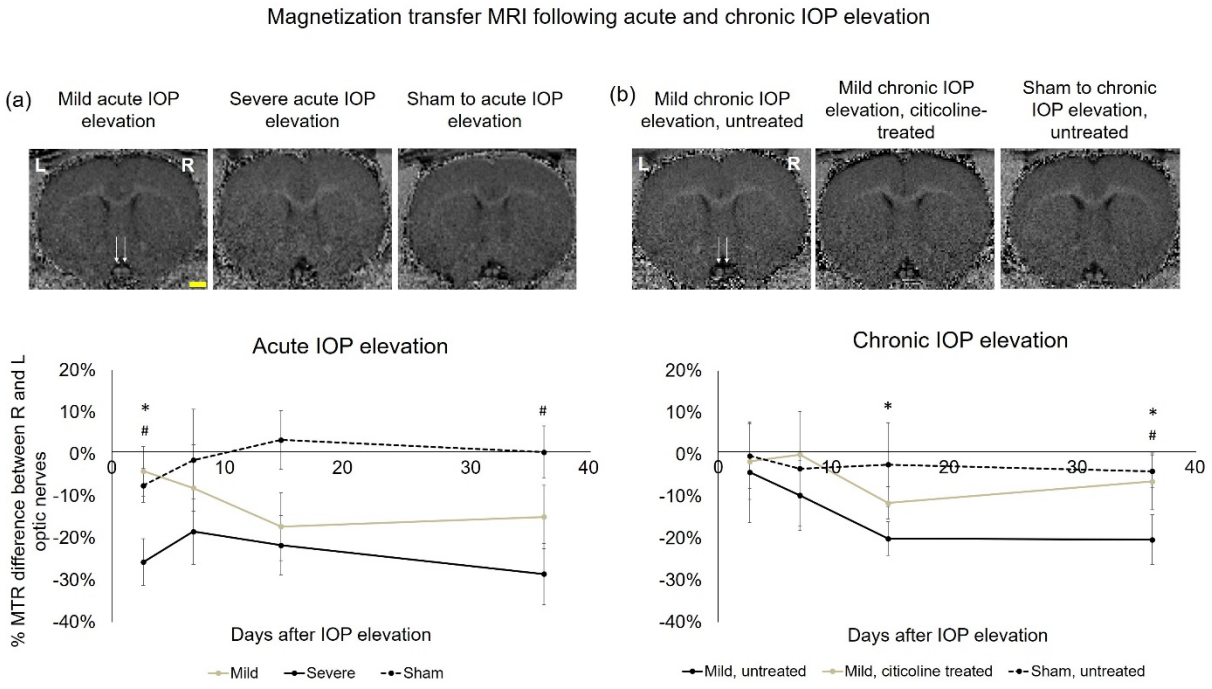

Figure 5. Magnetization transfer ratio between left and right optic nerves following acute (A) and chronic (B) IOP elevation. a. There was a significant difference between mild and severe groups 3 days after IOP elevation, and between sham and severe groups. b. There was a significant difference between untreated and citicoline treated groups 14 and 35 days after IOP elevation, and between untreated and sham groups.

2.3.5 IOP elevation decreased while citicoline recovered anterograde manganese transport to the optic nerve, lateral geniculate nucleus, and superior colliculus

Mn enhancement along the visual pathways projecting from the injured right eye [i.e. right optic nerve, left lateral geniculate nucleus (LGN), and left superior colliculus (SC)] and from the uninjured left eye (i.e. left optic nerve, right LGN, and right SC) was evaluated by quantifying their T1-weighted signal intensities before (pre-MEMRI) and at 8 hr (post-MEMRI) following intravitreal injection of $MnCl_2$ into both eyes at the end experimental time point at day 35 (Figure 6). No significant differences in T1-weighted signals was observed along the visual pathway between both hemispheres or between acute and chronic groups before intravitreal Mn injection (data not shown).

When assessing the percent intensity difference between injured and uninjured visual pathways, among the acute groups (Figure 6B-D), the left LGN showed a significantly larger reduction in Mn enhancement after severe acute IOP elevation to the right eye compared with mild acute IOP elevation and sham control (Figure 6C). The left SC also showed significantly larger reduction in Mn enhancement after severe acute IOP elevation compared to the sham control (Figure 6D).

Among the chronic groups (Figure 6E-G), the right optic nerve, left LGN and left SC showed a significantly larger reduction in Mn enhancement after untreated chronic IOP elevation compared to the sham control (Figure 6E-G), whereas the left LGN showed a significantly smaller reduction in Mn enhancement after citicoline-treated chronic IOP elevation compared to untreated chronic IOP elevation (Figure 6F). No significant difference in Mn enhancement was

observed between citicoline-treated chronic IOP elevation and sham control groups in the optic nerve or the SC (Figures 6E & 6G).

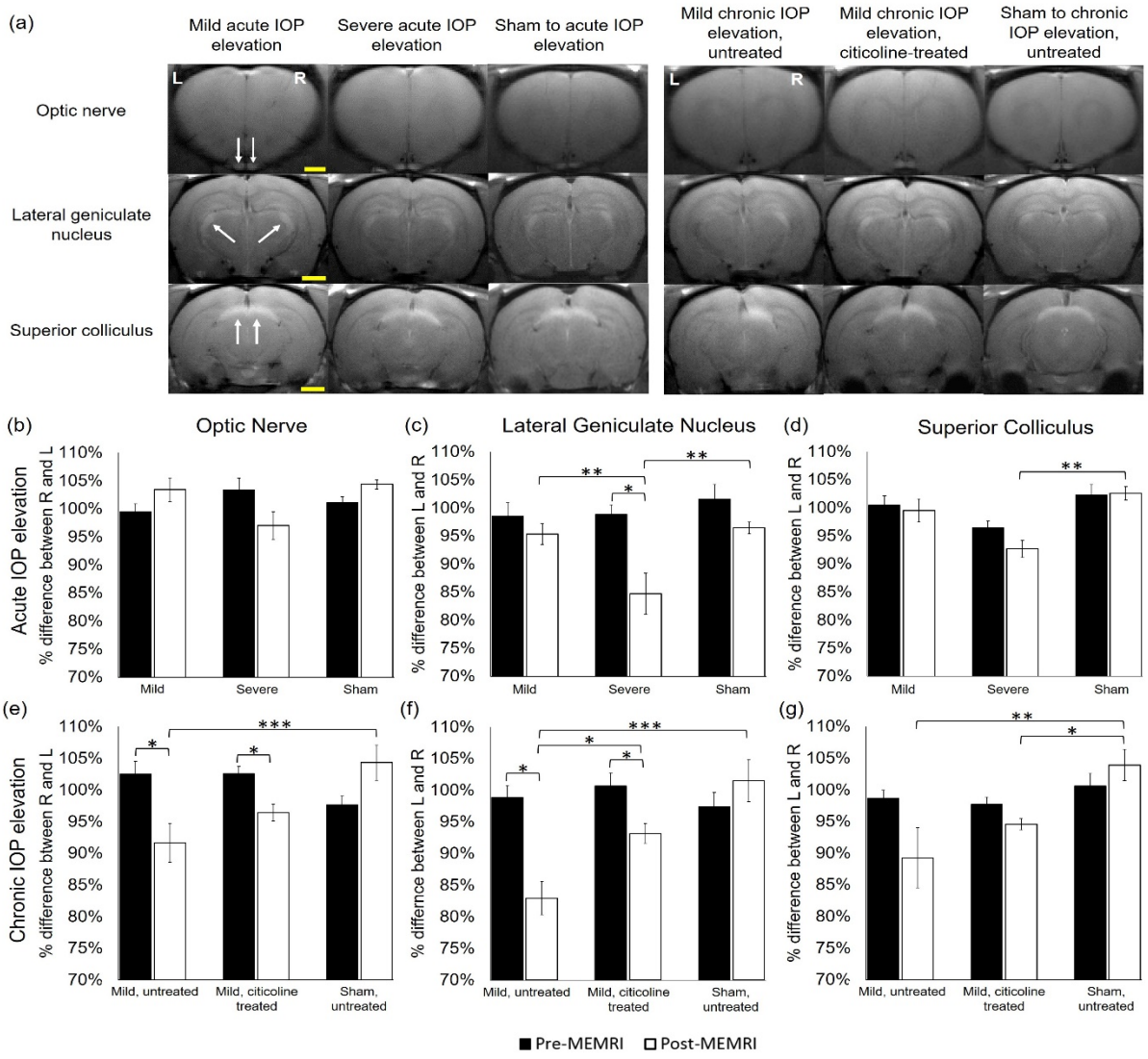

Figure 6. Representative post-MEMRI images in the optic nerve (ON) (top row), lateral geniculate nucleus (LGN) (middle row), and superior colliculus (SC) (bottom row) b. Percent difference in manganese enhancement was calculated between right and left ON, LGN, and SC

2.3.6 IOP elevation decreased functional connectivity between lateral geniculate nucleus, superior colliculus, and visual cortex, which was improved by citicoline treatment

When comparing the resting-state FC between LGN, SC, and the visual cortex (VC) of each hemisphere, significant FC differences were observed in the subcortical visual nuclei between all three acute groups, with greater differences across increasing magnitudes of IOP elevation (Figure 7). Among the chronic groups, animals with untreated chronic IOP elevation showed significantly decreased cortico-collicular, cortico-geniculate, and subcortical FC compared to the sham control within and between hemispheres (Figure 8). In contrast, animals that received chronic IOP elevation and oral citicoline treatment appeared to have preserved or improved FC. Compared to untreated chronic IOP elevation, the citicoline-treated group had increased FC between left VC and left SC.

2.3.7 IOP elevation decreased phosphorylated neurofilament and myelin basic protein expression in the optic nerve, while citicoline reduced such effects

Immunohistochemical staining for phosphorylated neurofilament (pNF) and myelin basic protein (MBP) showed comparable expression in the left optic nerve across all groups (Figure 9). pNF staining was decreased by 43.6 ± 3.6% and 65.7 ± 0.7 % in the right optic nerve of the mild and severe acute IOP elevation groups, respectively, compared to the left optic nerve. In the chronic IOP elevation group, the pNF staining in the right optic nerves was decreased by 64.4 ± 1.4% in the untreated group, and by 43.6 ± 3.5% in the citicoline-treated group. MBP staining was decreased in the right optic nerve of the mild and severe acute IOP elevation groups by 24.6 ± 4.2% and 65.1 ± 1.0%, respectively, compared to the left optic nerve. In the chronic IOP elevation

groups, the MBP staining was decreased by 59.4 ± 2.9% and 38.3 ± 4.2% in the untreated and treated groups, respectively, compared to the left optic nerve.

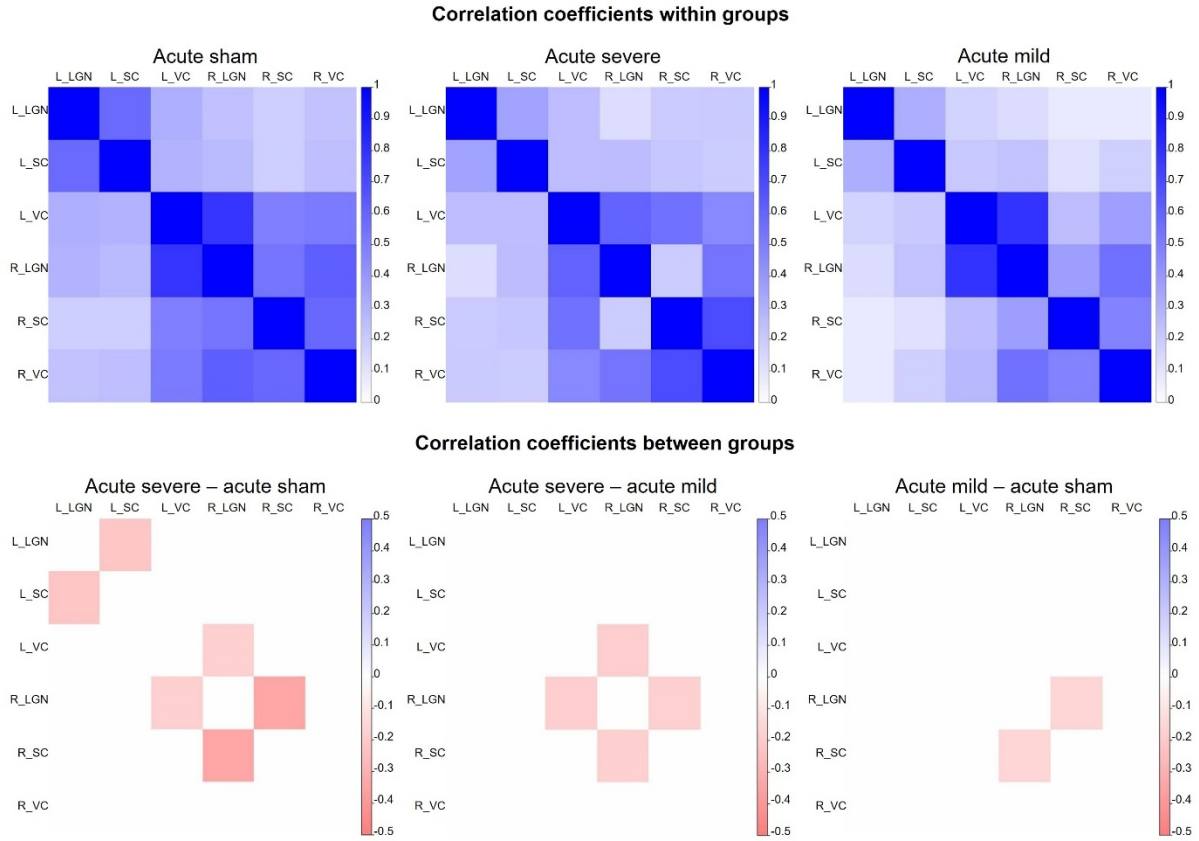

Figure 7. Resting state functional connectivity MRI at 35 days after unilateral acute IOP elevation induction at 15mmHg (sham), 40mmHg (mild), and 130mmHg (severe). Top row represents the correlation strengths between lateral geniculate nucleus (LGN), superior colliculus (SC) and visual cortex (VC) of the left (L) and right (R) hemispheres in each acute group. Bottom row represents the differences in functional connectivity (FC) between acute groups. Only statistically significant FC differences were colored in the bottom row.

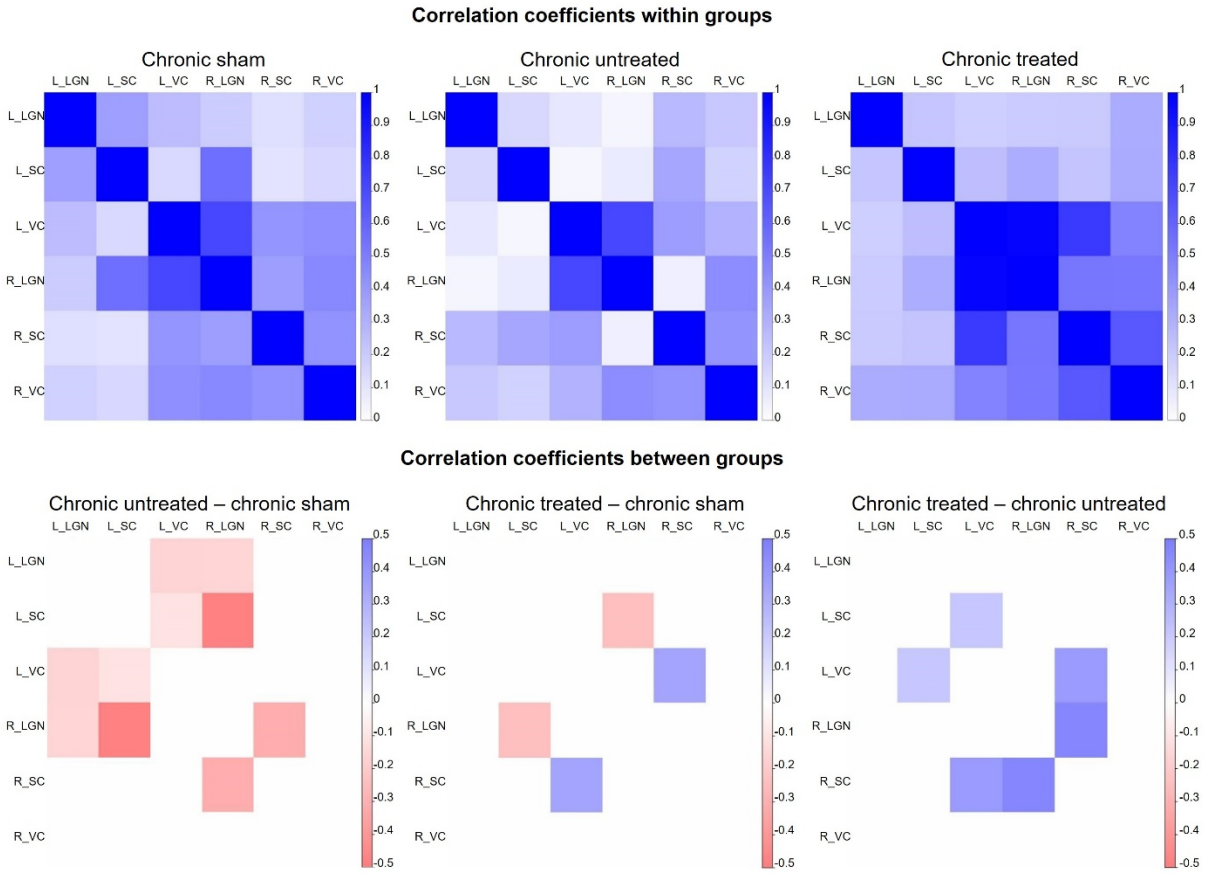

Figure 8. Resting state functional connectivity MRI 35 days after chronic intraocular pressure elevation (IOP) induction with (treated) or without (untreated) oral citicoline treatment, or sham operation (sham) without oral citicoline treatment. Top row represents the correlation strengths between lateral geniculate nucleus (LGN), superior colliculus (SC) and visual cortex (VC) of the left (L) and right (R) hemispheres in each acute group. Bottom row represents the differences in functional connectivity (FC) between chronic groups. Only statistically significant FC differences were colored in the bottom row.

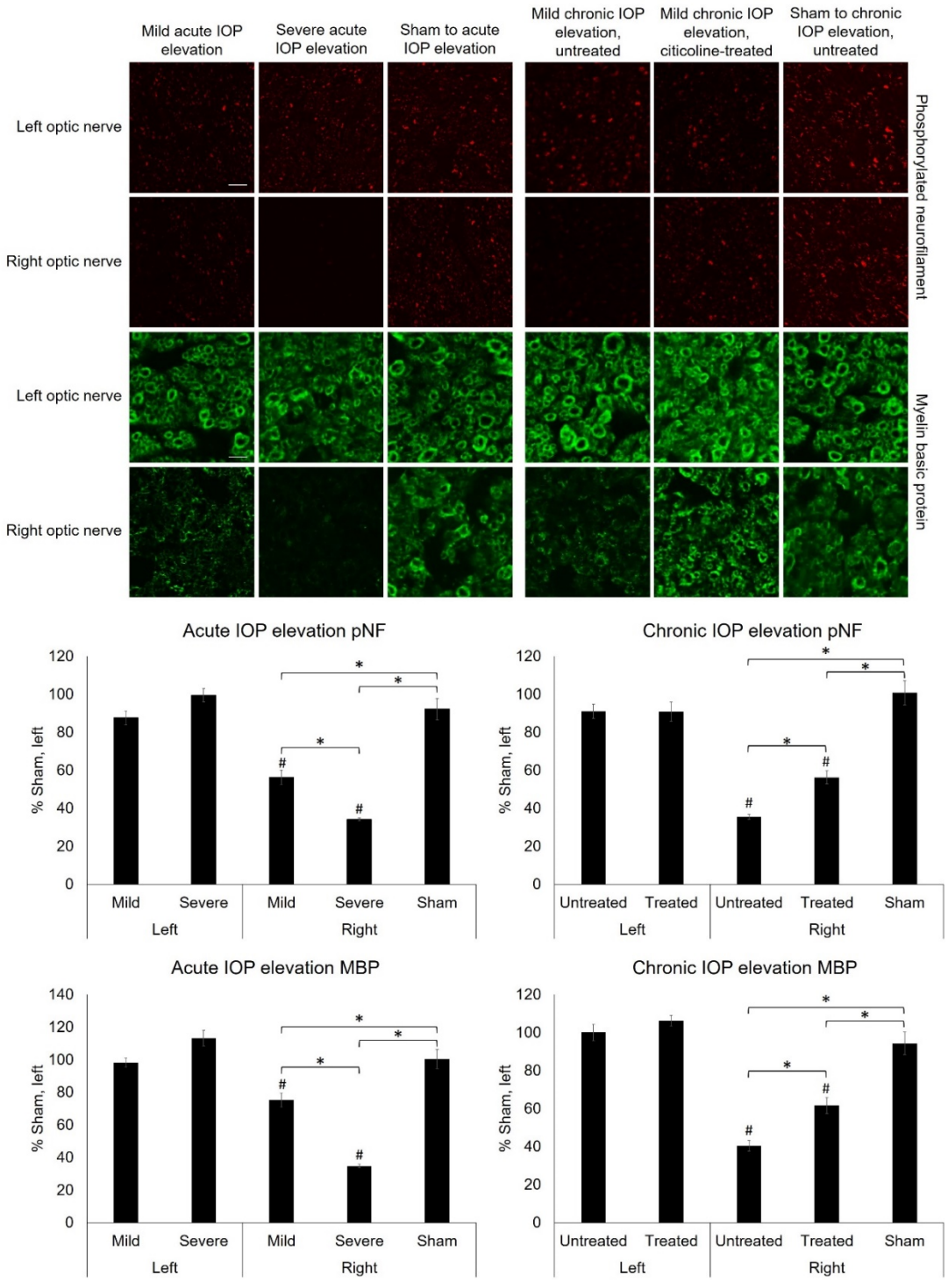

Figure 9. Phosphorylated neurofilament (pNF) and myelin basic protein (MBP) staining 35 days after acute and chronic IOP elevation.

2.4 DISCUSSION

This study demonstrated the neurobehavioral effects of different magnitudes and durations of IOP elevation on the visual system using well-controlled experimental glaucoma models. In addition, under similar levels of IOP elevation, oral citicoline treatment significantly reduced visual brain integrity loss and visual acuity decline. Studies have shown that glaucoma affects structural and functional connectivity in the human brain [156]. Both the acute and chronic models caused structural and functional changes in the visual system and demonstrated the neuromodulation of the visual system in behavioral outcomes in experimental glaucoma. Further the neuroprotective effects of oral citicoline in a chronic IOP elevation model were demonstrated.

Acute IOP elevation caused a decrease in visual acuity with severe acute IOP elevation causing a larger decrease in visual acuity than mild IOP elevation. The IOP elevation groups had a gradual decrease in visual acuity which coincided with the progressive increase in IOP. While the acute sham group, which only had a needle inserted in the anterior chamber and no pressure increase, demonstrated no changes in visual acuity, the chronic sham group displayed an initial decrease in visual acuity at day 7 that recovered by day 14. The effects of the buffer injection in the sham group were not assessed specifically. However, no prolonged effects on visual acuity or structural MRI were observed in the sham group following the buffer injection.

In experimental glaucoma models, moderate and severe acute IOP elevation do not cause any persisting changes to retinal nerve fiber layer thickness [157] or the optic nerve head and peripapillary structures [158, 159] and studies have shown that optic nerve dysfunction and disorganization may precede observable changes in vision and neuronal loss in glaucoma [160, 161]. The effect of chronic IOP elevation on these structures remains unknown. Under severe acute IOP elevation, significant changes were observed in optic nerve FA and $\lambda_{\perp}$, with no significant

change in $\lambda_{//}$. The increase in $\lambda_{\perp}$ suggests that demyelination occurred and continued progressing for up to 5 weeks after injury, even when IOP elevation was no longer present, and a similar but statistically insignificant trend was found in the optic tract. The decreased pNF positive staining and disrupted MBP morphology staining in the right optic nerve after acute IOP elevation, indicates that higher IOP elevation causes a larger disruption in neurofilament integrity and myelin density. In the chronic groups, the untreated group had significantly decreased pNF and MBP density compared to the sham and citicoline treated groups. The chronic groups had significantly lower axial diffusivity at day 35 as well, suggesting the decreased neurofilament integrity, as shown by decreased positive pNF staining, may be contributing to decreased axial diffusivity. The MBP results suggest that oral citicoline treatment preserves myelination after injury and may ultimately cause the increase visual acuity observed in the citicoline treated animals.

The large decrease in $\lambda_{\perp}$ was seen soon after induction of chronic IOP elevation indicating that the suggested demyelination occurs rapidly after with chronic IOP elevation. As in the visual acuity experiments, we observed less of a decrease in white matter integrity in the citicoline treated animals, suggesting that citicoline treatment ameliorates the damage caused by IOP elevation. In both the acute and chronic groups, we observed larger degrees of change in the optic nerve than the optic tract, suggesting that IOP elevation caused more severe structural alterations in the anterior visual pathway than the posterior visual pathway over 35 days. MTI can indicate changes in macromolecular structures [9]. Therefore, the larger MTI ratio in the citicoline treated group suggest that citicoline treatment before and after IOP elevation prevents, or inhibits, changes in white matter on a molecular level. The decreased myelin positive staining observed in the severe acute and chronic untreated animals coincides with $\lambda_{\perp}$ results from DTI, which showed increased $\lambda_{\perp}$ in the optic nerve. Together, these results indicate that the acute severe and chronic untreated

optic nerves may have undergone demyelination and that citicoline treatment preserved myelination.

MEMRI has previously been shown to be capable of indicating injury severity in an optic nerve crush model [162] and can be used to examine physiological anterograde Mn transport between the retina and the brain's visual pathway [163-165]. In the acute groups, there were no observable differences in $\lambda_{//}$ or Mn transport in the optic nerve. These coinciding results suggest $\lambda_{//}$ is related to Mn transport, as has been suggested in previous studies [166]. Following chronic IOP elevation without citicoline treatment, the optic nerve, LGN, and SC all showed significantly more Mn transport deficits compared to the sham injury group which coincides with decreased $\lambda_{//}$ integrity observed in these brain regions. The citicoline treated group showed significantly less Mn transport deficits in the LGN compared to the untreated group. These results indicate IOP elevation disrupts white matter integrity which may cause decreased anterograde transport in the visual system. Additionally, citicoline treatment ameliorates white matter integrity disruption after IOP elevation which preserves anterograde Mn transport.

Acute and chronic IOP elevation decrease both photopic and scotopic contrast sensitivity in rodents, and treatment with brinzolamide or brimonidine, both of which are IOP lowering therapeutics, is able to partially prevent contrast sensitivity loss [167]. In experimental glaucoma models in rats, choline metabolites were significantly reduced in the contralateral visual cortex after 6 weeks of IOP elevation, indicating that the metabolism of choline-containing compounds may be altered in glaucomatous visual pathway structures [168]. In young human subjects, proton magnetic resonance spectroscopy has shown an increase in choline in the brain after a single oral dose of citicoline [169], indicating that oral administration is a viable method for delivering citicoline to the CNS. Increases in retinal bioelectrical responses and improvement in the

bioelectrical activity in the visual cortex were observed 4 months after initiation of citicoline treatment and returned to baseline 2 month after cessation [170]. Rodent studies have found that increased levels of acetylcholine in the cortex drive a greater intensity in cortical responses and trigger the upregulation of cholinergic receptors [171]. Recently, clinical studies found that genes regulating acetylcholine metabolism may be altered in glaucoma patients and could increase the risk for developing primary angle-closure glaucoma [172]. In our study, we found that citicoline may be able to slow down a decline in visual acuity after IOP elevation. Citicoline in the chronic treated groups therefore slowed down functional loss independent of lowering the IOP.

Studies in mouse models have shown that although neurons may appear healthy histologically, IOP elevation may permanently decrease synaptic connections and neural activity [173]. Previous studies utilizing acetylcholinesterase inhibitors, compounds that prevent acetylcholine hydrolysis and increase the concentration and duration of acetylcholine in the CNS, have shown an increase in FC, visual perception, and processing [174], and enhanced brightness discrimination capacity after optic nerve crush [175]. Additional studies have shown that injection of an acetylcholine receptor antagonist leads to a decrease in FC in the default mode-like network [176], and decreased FC in the hippocampus, cortex, and thalamus, which could be partially reversed by administration of an agonist [177]. These previous studies, along with our current results demonstrating that oral citicoline preserves FC across the SC, LGN, and VC, suggest that increased citicoline concentration in the CNS may improve FC in the visual system and visual function after injury and disease.

This study has several limitations. Of note, Mn may be toxic to neural pathways [178], meaning that histology could only be performed using samples from animals that were not used for MEMRI experiments. Since retinal apoptosis and retinal ganglion cell death affect Mn uptake

in the retina, MEMRI findings may reflect the damage of the retina in addition to changes in Mn transport alone. In future studies, longitudinal scans over hours can be taken after intravitreal Mn injection to determine the rate of Mn transport along the visual pathway. No direct RGC evaluations were done in this study and the mechanisms of visual function prolongation weren't elucidated in the present study. However, previous. i*n vivo* studies have shown that daily citicoline treatment slows down RGC death after optic nerve crush [179] and induced apoptosis with kainic acid [180], and studies using topical treatment of citicoline have shown increased RGC activity [170, 181]. These studies suggest that citicoline treatment can slow RGC apoptosis after injury and increase RGC activity, which may lead to increased visual acuity preservation after injury and citicoline administration.

These experiments have important implications for both our understanding of glaucomatous degeneration and the ways in which we may be able to prevent such neurodegenerative processes. While it can be difficult to study glaucoma under controlled conditions in humans, this study uses experimental glaucoma animal models to simulate a variety of disease conditions. In doing so, it was possible to elucidate the differential effects of duration and magnitude of IOP elevation on structure and function in the visual pathway. More exciting, however, is the prospect of using such experiments to explore potential preventative and treatment measures for glaucoma. Recent literature suggest that citicoline may improve visual function outcomes in glaucoma patients [182-184]. However, several parameters need to be further investigated to optimize citicoline treatment, including dosage, timing, and route of administration [182, 185, 186]. Administration of citicoline, a choline supplement, concurrent with chronic IOP elevation resulted in improved visual acuity, white matter integrity, anterograde Mn Transport, and functional brain connectivity. Since brain regions other than the eyes are affected, treatment

mechanisms should focus on treating neural structures throughout the visual and nervous system and indicate intraocular pressure-lowering strategies combined with neuroprotective therapies can protect visual neurons in the retina and brain which may help to preserve vision in patients with glaucoma. This study provides a framework and experimental paradigm for such exploration, and experiments such as these will provide the groundwork for the future of glaucoma treatment.

3.0 AFTER ACUTE OPTIC NERVE ISCHEMIA IN RAT, FETAL PORCINE BRAIN ECM POSITIVELY MODULATES THE DEFAULT HEALING RESPONSE

3.1 INTRODUCTION

In adult mammals, central nervous system (CNS) neuron axons generally fail to regenerate after injury often leading to axonal degeneration, neuronal death, and permanently lost neurologic function. This failure is due, in part; to a default healing response in the CNS to prioritize rapid injury containment over preserving or restoring neurologic function. After injury, glial support cells adopt a pro-inflammatory phenotype, migrate to the injury site [38], and remodel the cellular and ECM architecture to form scar tissue [187]. Scar tissue is a complex multicellular mechanical and biochemical barrier critical to maintaining the integrity of the CNS by repairing breakdown of the blood brain barrier, containing lesions, foreign bodies, and infectious agents, among many other physical and metabolic functions [188]. However, the glial scar inhibits axon regeneration by multiple mechanical and biochemical barriers. Combinatorial approaches addressing intrinsic axon growth ability with or without modulating the innate immune response have shown that CNS axons can regenerate significant distances to restore functional reinnervation [189-191]. However, the number of regenerating axons is typically low, and many axons are misguided [192, 193]. A logical and perhaps complimentary approach to therapies that increase retinal ganglion cell (RGC) survival and axon growth may be to alter the default healing response by shifting the innate immune response within the affected CNS tissues from primarily pro-inflammatory toward a more anti-inflammatory, pro-repair response.

Extracellular matrix (ECM) technology can alter the default healing response by modulating the innate immune response [109, 194], , stabilizing the wound microenvironment [195], and stimulating site-appropriate cellular recruitment and differentiation to restore tissue function [110, 196]. Over 100 FDA approved ECM-based devices are used clinically to promote positive tissue remodeling over scarring [97]. ECM scaffolds have been used in preclinical models in numerous tissues, including heart [197, 198], esophagus [199-201], bladder [202], and muscle [203] , and recently both in the PNS and in the CNS [97, 204, 205]. ECM harvested from homologous tissue provides a more favorable environment in skin [206], cartilage [207], heart [208], tendon [209], and liver [210], among others. Moreover, ECMs derived from younger, homologous tissues can be more effective [113-115], like fetal heart [116] and kidney [117]. Studies using ECM for CNS applications are increasingly showing promise in supporting neuronal migration [211], differentiation [212], and neurite growth [213]. However, whether ECM derived from fetal brain tissue can positively modulate the default healing response in the CNS remains unreported.

The objectives of this study were to first successfully decellularize fetal porcine brain ECM. Traditional decellularization methods based using agitation are too harsh and disrupt the structure of fetal tissues. In delicate tissue like brain the majority of the ECM is lost, leading to low yields that are likely not representative of the native ECM. Therefore, vacuum assisted decellularization (VAD) [204] was used, which uses changes in pressure to pulse the decellularization agents in and out of delicate tissues, like fetal brain and retina, while maintaining the native ECM architecture to produce an acellular fB-ECM bioscaffold. The acellular scaffolds were used to develop an injectable fB-ECM hydrogel, and to test fB-ECM hydrogel biocompatibility and bioactivity *in vitro* in primary retinal ganglion cell cultures, and *in vivo* in

an established acute optic nerve ischemia model. Fetal porcine brains were successfully decellularized by VAD, preserving the delicate fetal brain ECM architecture, which is largely lost by traditional harsher agitation methods, and solubilized fB-ECM readily formed a hydrogel at 37°C. After acute optic nerve ischemia, fB-ECM pre-gel digests were easily injected into and filled the irregular retrobulbar space behind the eye, enveloping the injured optic nerve before gelling. These initial studies show fB-ECM hydrogels are biocompatible and bioactive both *in vitro*, increasing both RGC dendrite and axon growth, and *in vivo*, reducing GFAP expression by astrocytes at the injury site and, although speculative, possibly slowing the rate of RGC axon degeneration.

3.2 MATERIALS AND METHODS

3.2.1 Animals, reagents, and tissues

Sprague-Dawley rats were provided by Charles River (Wilmington, MA). All chemicals and enzymes were provided by Sigma-Aldrich (St. Louis, MO) and cell culture reagents by Life Technologies (San Diego, CA) unless otherwise noted. Fetal pigs (5-7 inches) were provided by Nebraska Scientific (Omaha, NE).

3.2.2 Fetal brain ECM (FB-ECM)

Fetal pig brains were dissected and decellularized using vacuum assisted decellularization (VAD) as described [119]. The resulting acellular fB-ECM was treated with deoxyribonuclease (DNase,

300 Kunitz units per ml) for 1h, then with 0.1% peracetic acid (PAA, Rochester Midland Corp., Rochester, NY, USA) in 4.0% ethanol for 1h. FB-ECM was washed with 1X PBS and nanopure water (3× for 15 min each). FB-ECM was frozen, lyophilized, sterilized using EtO, and stored at room temperature (rt) until further use. Qualitatively, decellularization was confirmed by hematoxylin and eosin (H&E) staining of fB-ECM sections fixed in 10% buffered formalin.

3.2.3 FB-ECM scanning electron microscopy (SEM) topography

FB-ECM pre-gel solutions (6 mg/ml) were incubated at 37ºC for 30 min, fixed overnight in 2.5% glutaraldehyde, washed in PBS (3× for 15 min each), dehydrated in graded ethanol (30, 50, 70, and 90%) for 30 min each and in 100% ethanol overnight, and finally critically point dried (Leica EM CPD030 critical point drier, Leica Microsystems, Buffalo Grove, IL, USA). Critically point dried fB-ECM was sputter-coated with a gold/palladium alloy (4.5 nm) using a Sputter Coater 108 Auto (Cressington Scientific Instruments, UK) and imaged on a JEOL JSM6330f scanning electron microscope (JEOL, Peabody, MA, USA).

3.2.4 Residual FB-ECM DNA

Residual DNA was quantified by digesting fB-ECM overnight with 0.1 mg/ml proteinase K at 50°C in Tris-EDTA buffer (10mM Tris, 1mM EDTA). Protein was removed by phenol/chloroform extraction and centrifugation. The aqueous phase was mixed with 3M sodium acetate in 100% ethanol, centrifuged, the pellet rinsed with 1X PBS, recentrifuged, and dried. Double-stranded DNA (ds-DNA) was visualized by gel electrophoresis and quantified by PicoGreen per manufacturer’s instructions (Invitrogen, Carlsbad, CA).

3.2.5 Collagen and sulfated glycosaminoglycan (sGAG)

Collagen was quantified using a Sircol Collagen Assay kit (Biocolor Ltd., UK) and sGAG quantified using a Blyscan Glycosaminoglycan Assay kit (Biocolor Ltd., UK). Briefly, fB-ECM (50 mg/ml) was digested with proteinase K, and collagen and sGAG contents analyzed by absorption at 550 nm and 656 nm, respectively, using a SpectraMax M2 spectrophotometer (Molecular Devices, LLC., Sunnyvale, CA, USA). One-way ANOVA statistical analysis was done using SPSS Statistics 19 (IBM, Armonk, NY, USA). Three samples from three independent ECM preparations were analyzed, totaling 9 samples.

3.2.6 FB-ECM hydrogel and material properties

FB-ECM hydrogels were made as described [214]. Briefly, lyophilized fB-ECM (6 mg/ml) was solubilized with pepsin (1 mg/ml; 2500 IU/mg) in 0.01 N HCl for 24h at rt, and fB-ECM pre-gel digests stored at -20°C. For use, pre-gels were thawed on ice and neutralized in media for *in vitro* or PBS for *in vivo* experiments. Turbidimetric gelation kinetics were measured using a SpectraMax M2 spectrophotometer (Molecular Devices). Briefly, a 6 mg/ml fB-ECM pre-gel solution at 4ºC was placed into a precooled 96-well plate (100 ml/well), immediately transferred to a spectrophotometer preheated to 37ºC, and the absorbance at 405 nm was measured every 2 min for 50 min. The assay was repeated in triplicate for three independent fB-ECM preparations. The following parameters were calculated: time to reach 50% and 95% maximum absorbance ($t_{0.5}$ and $t_{0.95}$), lag phase (t_{lag}, extrapolated from the linear portion of the curve), and the turbidimetric speed of gelation (S, determined by calculating the growth portion slope of the curve normalized to absorbance) [103]. Rheology was measured on a rheometer (AR2000, TA

instruments, New Castle, DE). Briefly, neutralized fB-ECM pre-gel was immediately put on a 40mm parallel geometry, the rheometer gap was set at 550 µm, and a dynamic time sweep was done with a 1 Pa stress, 0.5 % strain, and 1 rad/s after the temperature was increased to 37ºC.

3.2.7 Retinal ganglion cell (RGC) cultures

Primary RGCs were purified from male and female postnatal day 3 (P3) Sprague-Dawley rat pups (Charles River, Wilmington, MA) by immunopanning and cultured in NB-SATO media as described [215]. Purified RGCs were plated in NB-SATO (50 µl) at low density ($5 \times 10^3/cm^2$) in 96-well plates coated with poly-D-lysine (70 kDa, 10 µg/ml; Sigma-Aldrich Corp., St. Louis, MO, USA) and laminin (2 µg/mL, Sigma-Aldrich Corp.) and cultured at 37ºC. To analyze fB-ECM effects on RGC viability and neurite growth, 2X stocks of fB-ECM (500µg/ml), or pepsin (50µg/ml) were thawed on ice, neutralized to pH 7.4, and added to the cultures by pipetting immediately after plating, yielding a final concentration of 250 µg/ml. The RGCs were cultured at 37°C in 10% CO_2 for 3 days *in vitro* (DIV). All RGC cultures were performed in triplicate for at least three experimental repeats. One-way ANOVA statistical analysis was done with SPSS Statistics 19 (IBM, Armonk, NY, USA).

3.2.8 RGC viability

After 3 DIV, viability was analyzed using a live/dead cell imaging kit per manufacturer's instructions (R37601, Molecular Probes, Life Technologies). RGCs were imaged by epi-fluorescence (Zeiss AxioObserver, Zeiss, Oberkochen, Germany) using rhodamine and fluorescein filter sets. At least 3 randomly selected fields of view were imaged per well, for a

total of 9 fields of view per condition per experiment and analyzed using ImageJ (National Institutes of Health, Bethesda, MD, USA). Thus, data represents at least 27 fields of view per condition, totaling more than 300 cells per condition from three independent experiments. One-way ANOVA statistical analysis was done with SPSS Statistics 19 (IBM, Armonk, NY, USA).

3.2.9 RGC neurite growth

RGC neurite growth was analyzed as described [216]. After 3 DIV, fixed RGC cultures were incubated with anti-β III tubulin (1:300, TUJ-1, Millipore) primary antibody and amplified with a FITC-labeled rabbit anti-chicken IgY H+L (1:150, CAT31501, Thermo Scientific) for 1h at rt. RGCs were counterstained with DAPI (1:3000, 62247, Thermo-Fisher Scientific) and imaged using epi-fluorescence (Zeiss, Axio Observer, Germany). Neurite length was quantified using the ImageJ Plugin, NeuronJ (National Institutes of Health, Bethesda, MD, USA) as described [216]. Total and axon length were quantified as described [121]. One-way ANOVA statistical analysis was done using SPSS Statistics 19 (IBM, Armonk, NY, USA). At least 10 randomly selected RGCs were imaged per well in triplicate, totaling at least 30 RGCs for three experimental repeats, equaling 90 neurons per condition.

3.2.10 Acute optic nerve ischemia

Adult Sprague-Dawley rats were anesthetized with an intraperitoneal injection of a ketamine (45 mg/kg) and xylazine (10 mg/kg) and anesthesia confirmed by toe-pinch reflex. The optic nerve was exposed by making an incision in the lateral conjunctiva. A nearly bloodless plane was made using blunt dissection posteriorly until the optic nerve was exposed. Ischemia was induced by

clamping a Yasargil aneurysm clip (Aesculap FT252T) [217] (B. Braun Medical Inc.) approximately 2 mm behind the globe for exactly 10 sec. The clip was removed, and the ophthalmic artery visualized to confirm integrity. The optic nerve sheath was then fenestrated by making a lateral 2 mm incision in the optic nerve sheath using a Grieshaber ultrasharp (Alcon Grieshaber, Schaffhausen, Switzerland). Immediately after fenestration, fB-ECM pre-gel (2 µl, 6 mg/ml) was injected into the retrobulbar space around the optic nerve in n=5 animals. Following surgery with or without fB-ECM injection, the connective tissue and the conjunctiva were sutured and antibiotic ointment (Gentamicin, Bausch & Lomb, Tampa, FL) applied to the eye. Sample size was determined through power analysis with G*power software (G*power software 3.1.9.2, Germany). Based on previous experiments, effect size was calculated to be 0.6, and power analysis for ANOVA dictated n=5 animals per group for *in vivo* studies to achieve 80% for $\alpha = 0.05$.

3.2.11 Immunohistochemistry

Animals were euthanized 14 days after surgery. The optic nerves were dissected, fixed in 4% paraformaldehyde in PBS for 2 h, cryoprotected in 30% sucrose in PBS for 4 h, embedded in optimal cutting temperature (OCT) medium (Tissue-Tek; Miles Inc, Elkhart, IN), frozen in liquid nitrogen, and stored at -80ºC until sectioning. For sectioning, 15 µm thick longitudinal optic nerve sections were cut using a cryostat (Leica CM 1850; Leica Biosystems, Wetzlar, Germany), noting proximal and distal ends of the nerve. Sections were labeled with anti-growth associated protein 43 (anti-GAP43, 1:300, Thermo Scientific, RRID:AB_598153), anti-glial fibrillary acidic protein antibody (anti-GFAP, 1:300, Abcam, RRID:AB_296804), or anti-β-III tubulin (TUJ-1, 1:300, Millipore, RRID:AB_1977541). All sections were stained with the nuclear stain DAPI, and imaged

with epi-fluorescence (Zeiss, Axio Observer). Fluorescence intensity was measured using ImageJ as described [218, 219]. Briefly, fifteen 100x100 pixels ROIs were drawn 1mm before and after the crush site (GFAP) or 2mm after the crush site (GAP-43), four 100 × 100 pixels ROIs were drawn on the image background, and the area, mean fluorescence, and integrated density of each ROI was quantified. The corrected total fluorescence (CTCF) for each antibody was calculated using the formula: CTCF = integrated density – (area x mean background fluorescence). For βIII-tubulin sections, βIII-tubulin positive fluorescence per area was measured by placing ten 50 × 50 pixels ROIs approximately 2mm posterior to the crush site. The ImageJ particle counter function was used to measure the area of each ROI and the percentage of each area covered by βIII-tubulin staining. The percentage βIII-tubulin per total area was calculated: % coverage = (area βIII-tubulin positive staining/area of ROI) X 100. Data represents triplicate sections from each of the five animals per group. One-way ANOVA statistical analysis was done with SPSS Statistics 19 (IBM, Armonk, NY, USA).

3.3 RESULTS

3.3.1 Fetal porcine brain ECM derived by VAD

Fetal porcine brains (fBs) were successfully decellularized by VAD [121] to produce acellular fB-ECM, which was cotton-like after lyophilization (Figure 10 A-B). Scanning electron microscopy at 200× revealed ribbon-like structures of varying sizes (Figure 10C). At 10,000×, the ribbon-like structures had a granular surface without obvious fibrils (Figure 10D) typical of non-CNS [220] and CNS tissue ECMs [221] generated by agitation. H&E staining revealed hematoxylin positive

nuclear DNA in native fB (Figure 10E). After VAD, fB-ECM generally lacked hematoxylin positive staining, indicating nuclear and double stranded DNA removal (Figure 10F), while eosin positive staining remained, consistent with remaining ECM associated collagen and acidophilic proteins. Gel electrophoresis showed dsDNA was largely undetected in fB-ECM (Figure 10G). Quantitatively, VAD reduced dsDNA by 94% from 2859±17 ng/mg in native fB to 173±5 ng/mg in fB-ECM (Figure 10H).

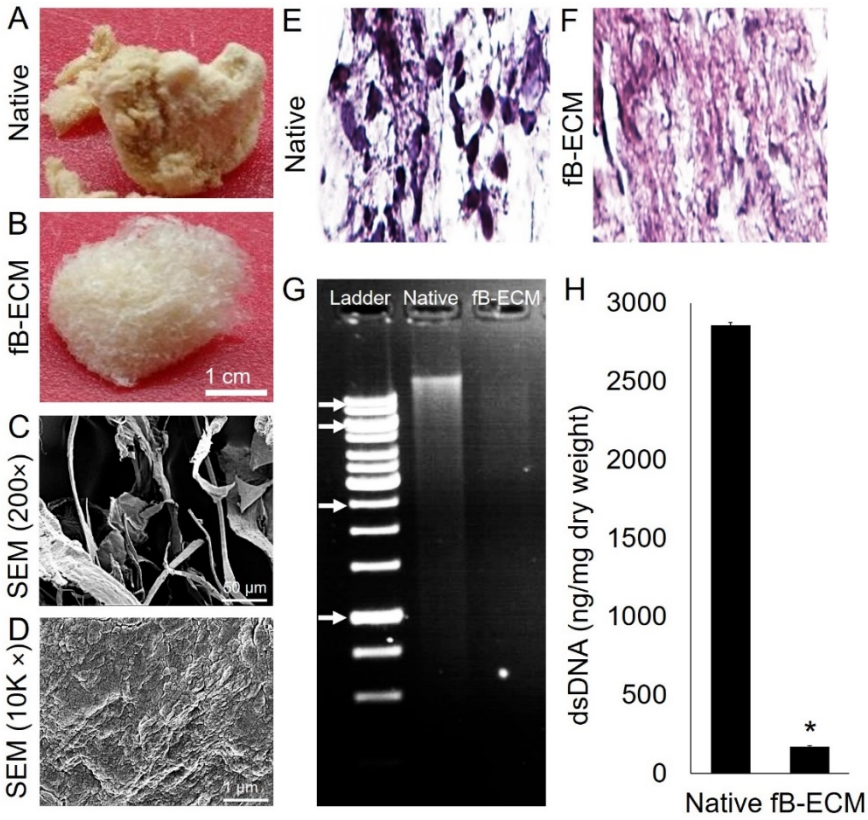

Figure 10. Native and vacuum assisted decellularized (VAD) fetal brain tissue. A. Macroscopic appearance of A. dry fetal brain and B. fetal brain ECM (fB-ECM) derived by VAD. C-D. Scanning electron microscopy of fB-ECM at C. 200× and D. 10,000×. E-F. H&E staining of fetal brain E. before (Native) and F. after VAD (fB-ECM). G. Gel electrophoresis of Native fetal brain and fB-ECM. G. PicoGreen analysis showed double stranded DNA (dsDNA) was largely removed by VAD.

3.3.2 FB-ECM collagen, sulfated glycosaminoglycan, and hyaluronic acid

Collagen, sulfated glycosaminoglycan (sGAG), and hyaluronic acid (HA) content were analyzed in native fB and in fB-ECM (Figure 11). VAD increased collagen from 0.03±0.0 mg/mg dry weight in native fB to 0.5±0.02 mg/mg dry weight in fB-ECM. In contrast, VAD reduced sGAG from 67±2 µg/mg in native fB to 24±1 µg/mg in fB-ECM (Figure 11B). Similarly, HA decreased from 44±1 µg/mg in native fB to 12±1 µg/mg in fB-ECM (Figure 11C).

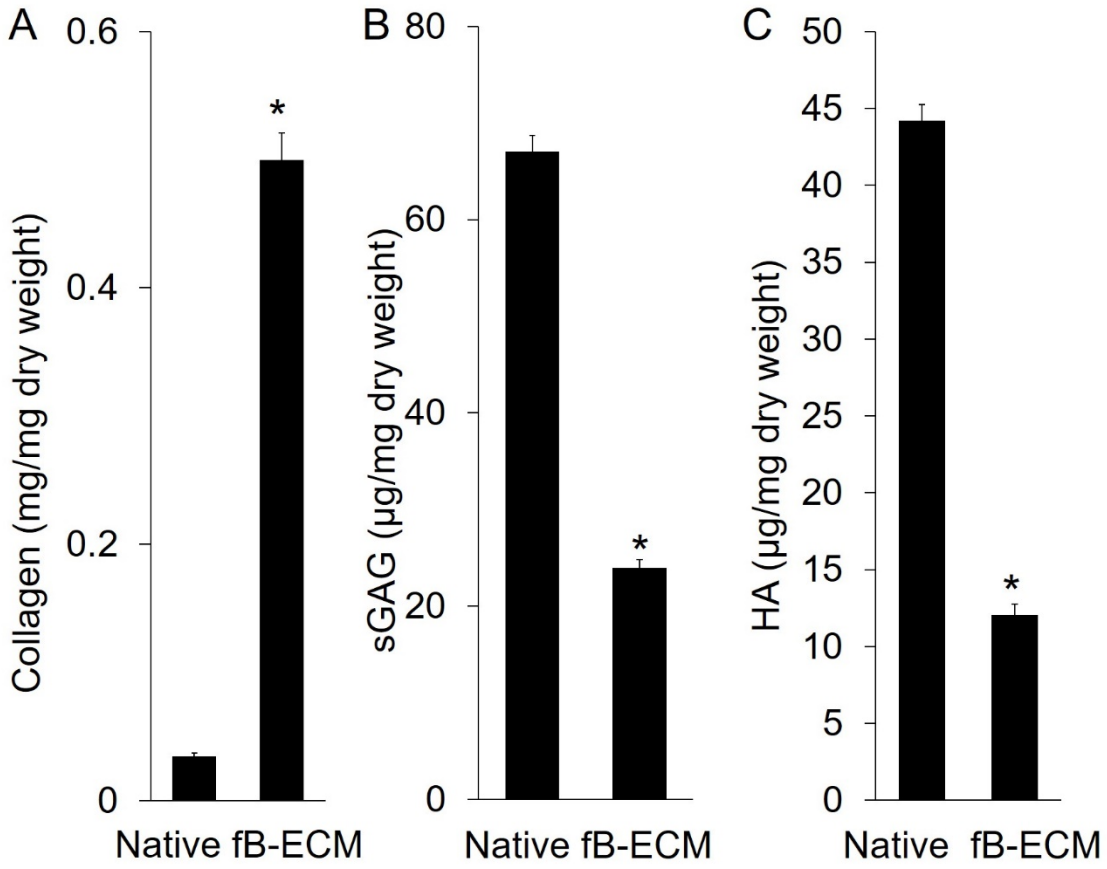

Figure 11. VAD differentially alters collagen, sulfated glycosaminoglycan (sGAG), and hyaluronic acid (HA) content. Compared to Native fetal brain, A. Collagen is increased and both B. sGAG, and C. HA are decreased in fB-ECM.

3.3.3 FB-ECM hydrogel morphology, gelation, and rheology

Consistent with other ECM hydrogels including adult brain [221], solubilized fB-ECM formed opaque hydrogels at 37°C that retained the cylindrical form of the mold (Figure 12A). Microscopically, SEM showed fB-ECM hydrogels have a fibrous morphology (Figure 12B) with dense, randomly oriented collagen fibrils (Figure 12C). Quantitative analysis of fB-ECM hydrogel gelation revealed a turbidimetric gelation curve with a sigmoidal shape and a gelation speed of 0.15± 0.05 min^{-1}. The gelation lag phase was 5.6±4.9 min, 50% gelation was reached at 12.4±2.7 min, and 95% gelation at 30.7±7.1 min (Figure 12D). The rheology of fB-ECM hydrogels was measured using a parallel plate rheometer (Figure 12E).

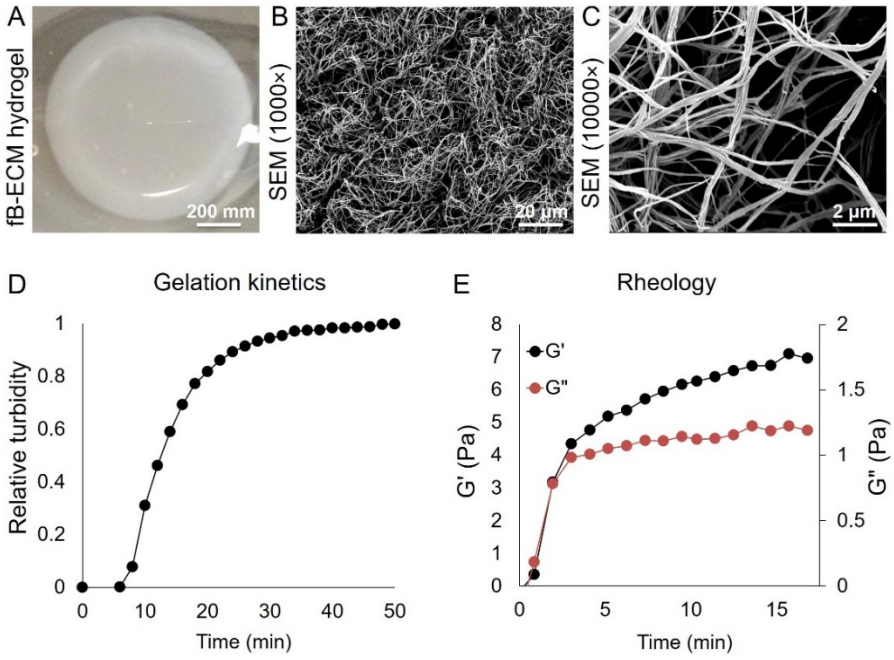

Figure 12. Macro- and microscopic 6mg/ml fB-ECM hydrogel properties. A. Macroscopic and scanning electron microscopy (SEM) images of fB-ECM hydrogel at B. 1000× and C. 10,000×. D-E. Representative fB-ECM hydrogel (6 mg/ml) D. gelation kinetics and E. rheology curves.

The viscosity of the pre-gel fB-ECM solution was 0.12±0.04 Pa. Rheological analysis showed the storage modulus (G') and loss modulus (G'') increased sigmoidally as a function of time from 10ºC to 37ºC. Once 37ºC was reached the pre-gel rapidly formed a gel. After 0.4±0.1 min, G' became greater than G'', indicating the gel became a solidified structure. G' and G'' maxima were reached at 14.7 ±0.5 min, with G' = 6.6±0.5 Pa and G'' = 1.1±0.1 Pa.

3.3.4 FB-ECM hydrogels and RGC viability and growth

To determine if fB-ECM hydrogels can modulate RGC survival and growth, RGC viability and total neurite and axon growth were analyzed (Figure 13). Previous dose response studies showed CNS neuron viability and neurite growth were maximally stimulated by both non-CNS and CNS derived ECMs at 250 μg/ml [121]. Primary RGCs were cultured in media, pepsin control, or media spiked with fB-ECM at 250 μg/ml and visualized with either calcein green and propidium iodide (Figure 13A) or anti-βIII tubulin and the nuclear marker DAPI (Figure 13B-D). Dose response studies were done with fB-ECM at 125, 250, and 500 μg/ml. Live/dead analysis showed RGC viability was unaltered by either pepsin or fB-ECM at 250 μg/ml. RGC viability in media at 3 DIV was 55.2 ± 7.8%. Normalized to media, viability was 93.48 ± 14 % in pepsin control and 99.1 ± 14.5 % in fB-ECM media (Figure 13E). In contrast to viability, fB-ECM increased total neurite growth by approximately 45% to 293.1 ± 18.9 μm compared to 202.3 ± 19.2 μm in media and 191.9 ± 19.9 μm in pepsin (Figure 13F). Similar to total neurite growth, fB-ECM increased the longest neurite, the presumptive axon, by approximately 35% to 154.4 ± 10.6 μm, compared to 121.5 ± 10.8 μm in media and 113.1 ± 11.2 μm in pepsin (Figure 13G). When cultured with 125, 250, or 500 μg/ml fB-ECM, RGC did not show a dose response for viability at 113.2 ± 13.8%, 99.1 ± 14.5%, and 116.5 ± 13.6%, respectively. Similar to viability, total neurite

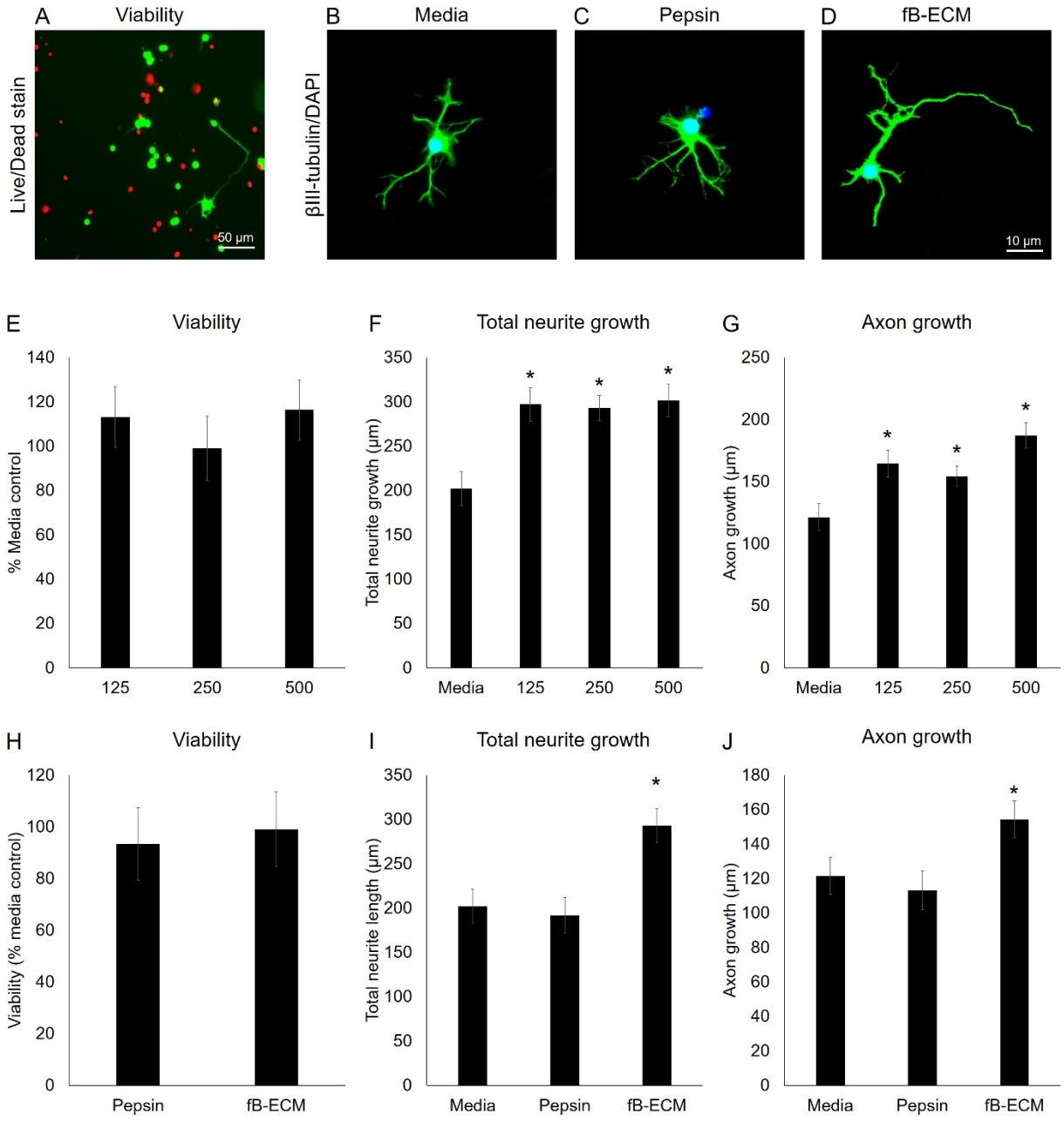

Figure 13. FB-ECM differentially regulates primary RGC viability and neurite growth. E-G. Dose response using 125, 250, and 500 µg/ml fB-ECM for E. Viability, F. Total neurite growth, and G. Axon growth. H. Viability was unchanged by fB-ECM. I. Total neurite growth increased in fB-ECM and most of this increased growth was due to J. increased axon growth.

growth for 125, 250, or 500 μg/ml fB-ECM did not show a dose response with neurite growth at 3 DIV at 297.2 ± 18.9 μm, 293.1 ± 14.3 μm, and 301.7 ± 18.3μm, respectively. Lastly, longest neurite growth also did not show a significant dose response, with longest neurites for 125, 250, or 500 μg/ml fB-ECM being 164.7 ± 10.6 μm, 154.4 ± 8.03 μm, and 187.3 ± 10.3 μm, respectively.

3.3.5 FB-ECM hydrogels decrease glial fibrillary protein expression

To determine if fB-ECM hydrogels can alter the default glial response to CNS trauma, fB-ECM hydrogel was injected retrobulbarly after acute optic nerve (ON) ischemia (Figure 14). Immediately after ischemic injury, the optic nerve sheath was fenestrated, and the hydrogel injected into the cavity where it formed a hydrogel. Glial fibrillary acidic protein (GFAP) immunoreactivity was analyzed two weeks post injury (Figure 15). Compared to GFAP expression in uninjured ONs (Figure 15A), GFAP was elevated at the injury site in untreated injured ONs (Figure 15B). In contrast, GFAP was noticeably lower at injury sites in fB-ECM treated ONs (Figure 15C). Higher magnification images showed the typical linear organization of GFAP expression and DAPI positive nuclei in uninjured nerves. In untreated, injured nerves both GFAP and DAPI positive nuclei were elevated, consistent with typical inflammation and astrogliosis [222]. In contrast, GFAP and DAPI varied qualitatively from animal to animal in fB-ECM treated ONs. In some ONs, GFAP and DAPI were noticeably elevated compared to the surrounding ON (Figure 15F) though to a much lesser extent than untreated, injured ONs. In other fB-ECM treated ONs, GFAP expression and the number of DAPI positive nuclei were similar to uninjured nerves. Though, the organization of both markers was exhibited a less orderly organization (Figure 15G). However, despite the apparent variability and altered organization, GFAP expression in fB-ECM

ONs was quantitatively similar to untreated nerve compared to untreated nerves which were significantly higher (Figure 15H).

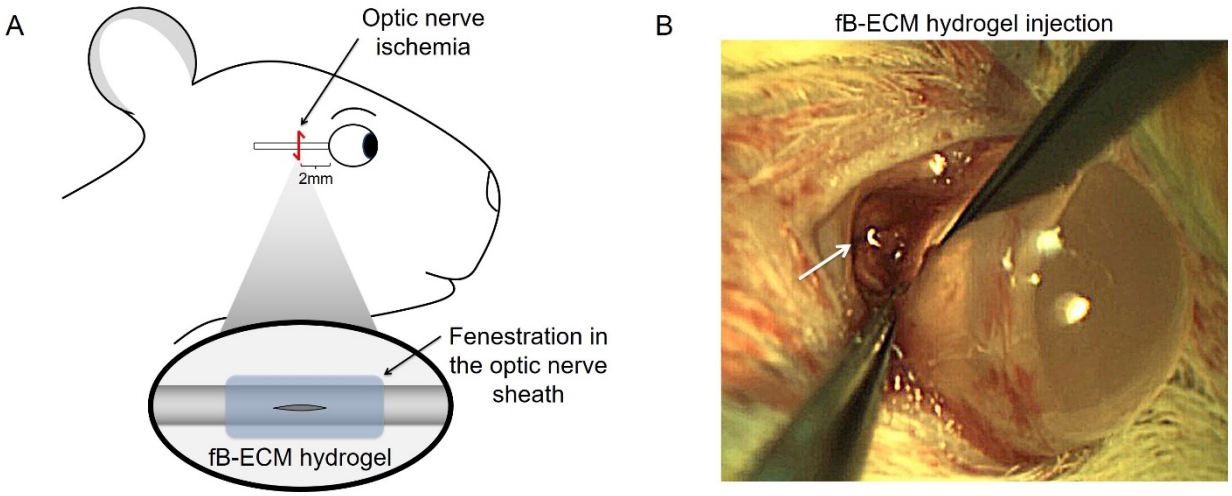

Figure 14. FB-ECM hydrogel injection after acute optic nerve ischemia. A. Schematic image of optic nerve injury, showing fenestration in the optic nerve sheath and fB-ECM hydrogel placement. B. Image showing minimally invasive optic nerve crush procedure and fB-ECM hydrogel filling the retrobulbar space.

To determine if fB-ECM stimulated RGC axon growth *in vivo* growth associated protein-43 (GAP-43) immunoreactivity was analyzed (Figure 16). Compared to uninjured ONs and untreated injured ONs (Figure 7A-B), GAP-43 was elevated in some but not all ONs treated with fB-ECM (Figure 16C-D). Similar to GFAP expression, GAP-43 expression varied qualitatively in intensity between animals (compare Figure 16 C-D). However, despite the apparent qualitative variability, the quantified intensity of GAP-43 immunoreactivity was approximately two-fold greater than uninjured and untreated ONs (Figure 16E). However, even in those animals with increased GAP-43 expression, the expression pattern was atypical and inconsistent with the patterning of RGC

axons in the ON. In GAP-43 positive animals, GAP-43 was localized to clusters that often appeared to have fine processes emanating from them and were spaced uniformly along the length of the ON. Moreover, these clusters failed to co-localize with GFAP, CD11b, SOX2, and doublecortin, suggesting the GAP-43 positive clusters were acellular remnants of degenerated RGC axons that in some cases may have activated a pro-growth program that initially increased GAP-43 expression but ultimately degenerated.

To visualize RGC axon organization, ON sections were stained with βIII-tubulin (Figure 17). Though the anterograde tracer cholera toxin subunit B is the gold standard for visualizing regenerated RGC axons in the optic nerve, βIII-tubulin localization is a reliable marker for evaluating RGC axon organization in ON sections. In the ON, RGC axons are bundled in highly ordered fascicles that are visibly and quantifiably disrupted by significant RGC axon degeneration. Compared to uninjured ONs (Figure 17A), βIII-tubulin immunoreactivity in untreated injured ONs was fragmented and disordered (Figure 17B). In contrast and similar to both GFAP and GAP-43 expression, βIII-tubulin was variable from animal to animal. βIII-tubulin immunoreactivity appeared fragmented in all fB-ECM treated animals. However, βIII-tubulin positive fascicles were identifiable to varying degrees in all fB-ECM treated ONs (Figure 17 C-D), suggesting RGC axons degenerated at a slower rate in fB-ECM treated ONs.

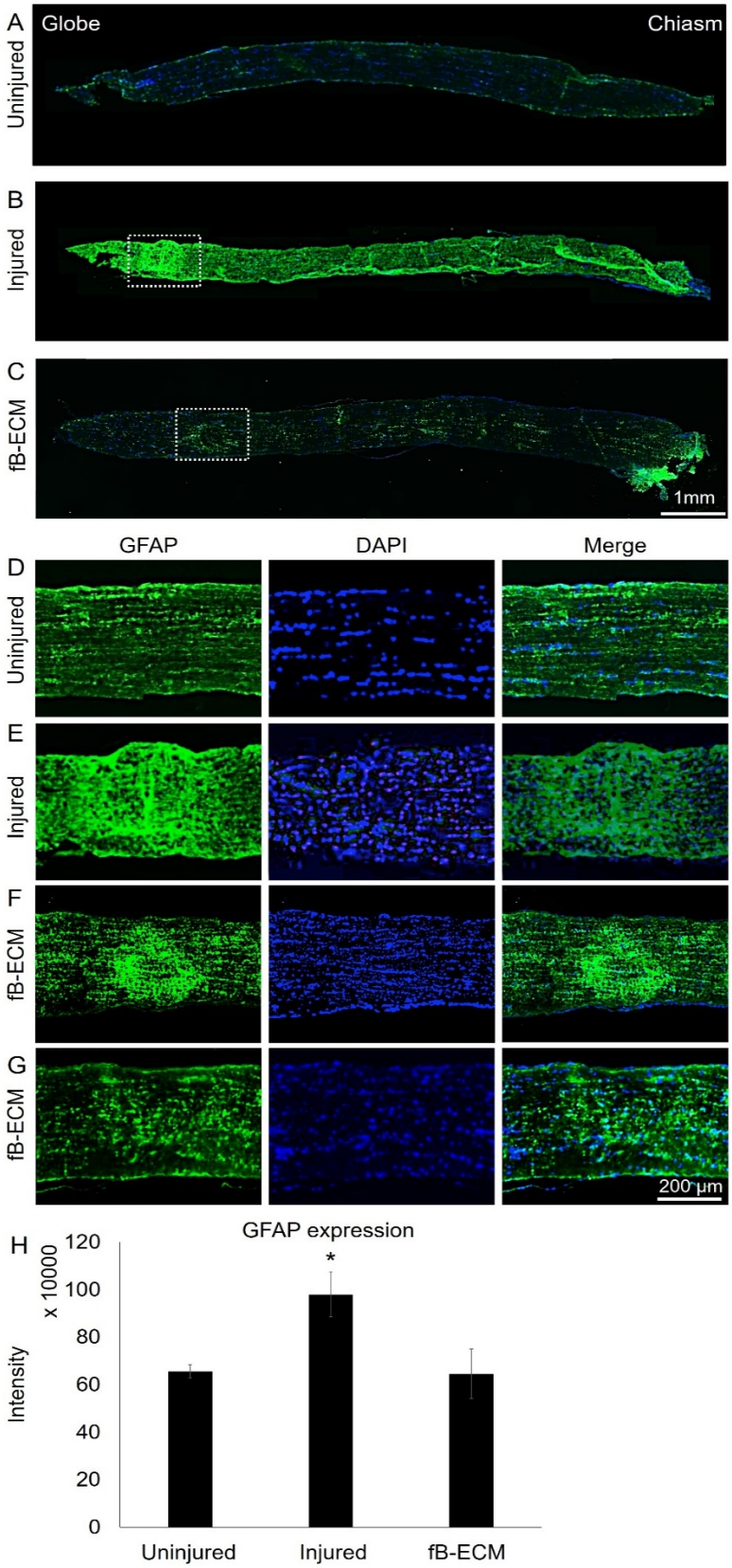

Figure 15 After acute optic nerve ischemia in rat, fB-ECM hydrogels decrease GFAP expression at the injury site.

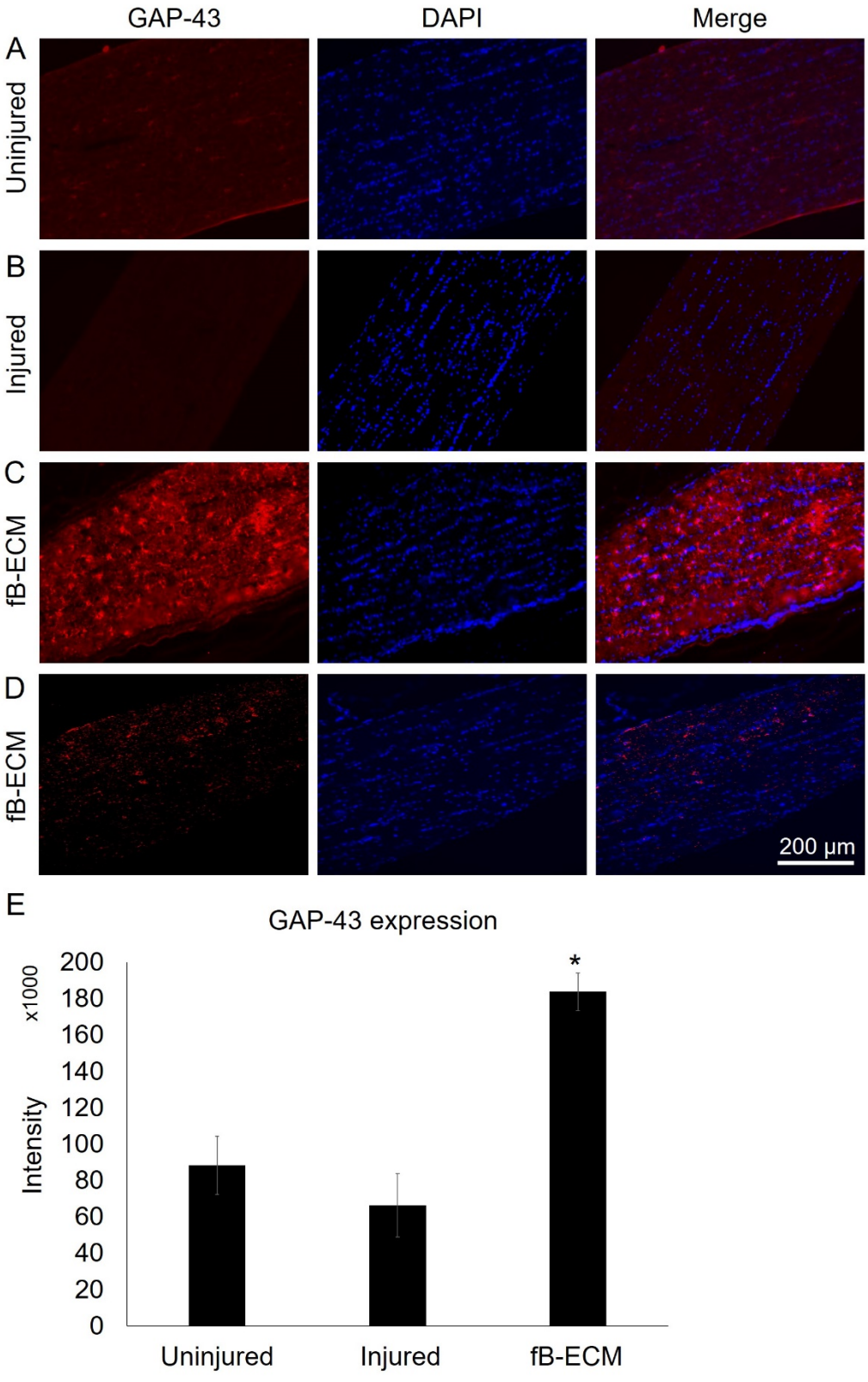

Figure 16. After acute optic nerve (ON) ischemia, fB-ECM increases GAP-43 immunoreactivity.

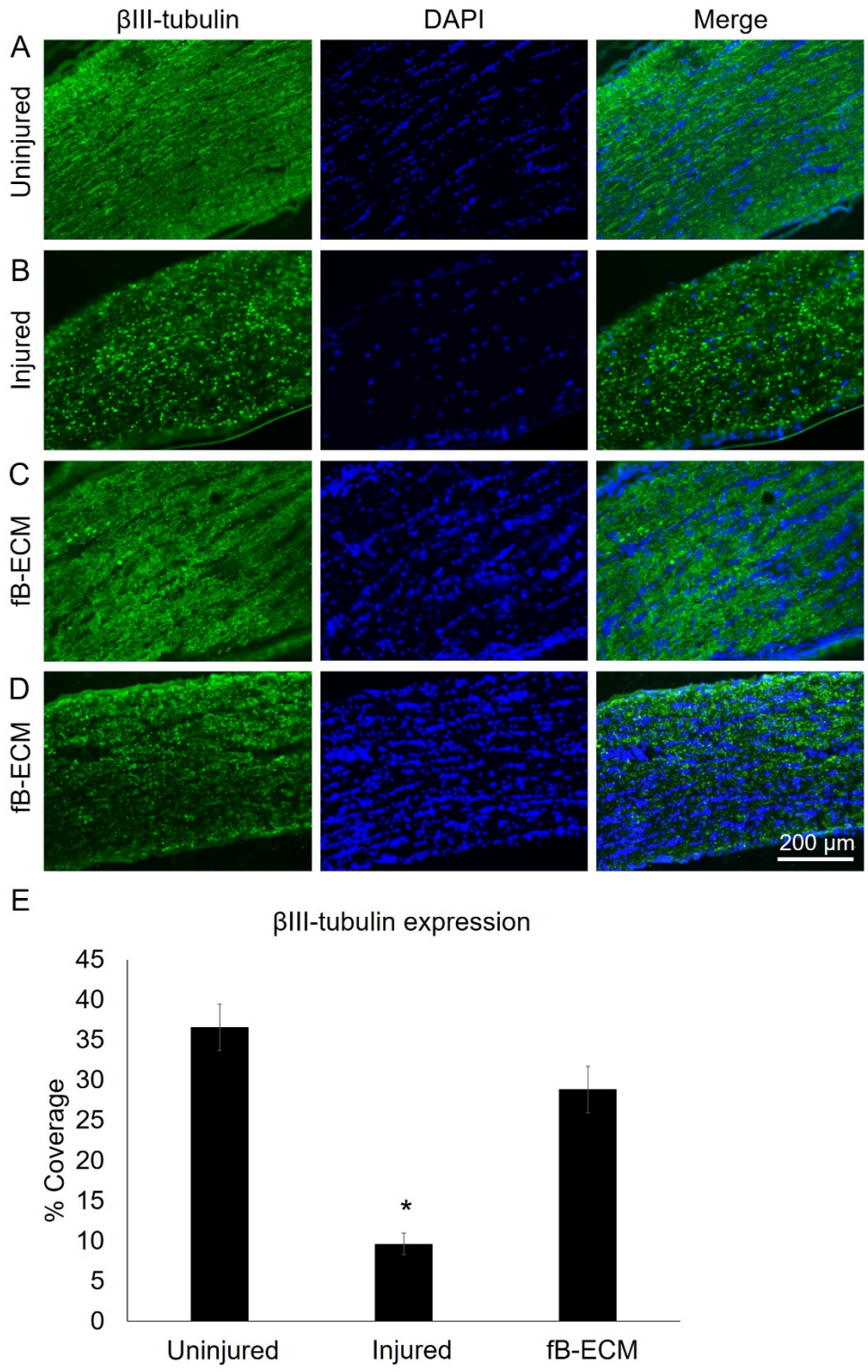

Figure 17. FB-ECM increases βIII-tubulin expression after optic nerve ischemia. B. Optic nerve ischemia alters the βIII-tubulin expression pattern, while C. fB-ECM treatment maintains an expression pattern resembling uninjured control.

3.4 DISCUSSION

This study reports on the decellularization of fetal brain tissue by VAD, initial material properties, and initial effects *in vitro* on purified RGCs and *in vivo* on the expression of markers of optic nerve remodeling after injury. The resulting fB-ECM had low dsDNA and high sGAG content, and successfully formed a hydrogel. The delicate nature of the fetal brain tissue makes standard agitation decellularization unfavorable due to its disruptive effects on the ECM microstructure, while the differential pressure used in VAD helps solutions penetrate deep into tissues to remove cellular content, thereby effectively decellularizing tissue while preserving ECM organization [204, 223, 224].

Collagen is one of the main components in ECM and plays a vital role in the ability of ECM to form a hydrogel. Relative collagen content is calculated based on total weight, and decellularization therefore increases the relative collagen content due to the removal of cellular components and conservation of collagen. Although FB-ECM had a relatively lower collagen content compared to AB-ECM [221], FB-ECM successfully formed a hydrogel. sGAGs help with maintaining tissue hydration, binding growth factors, and regulating cellular behavior *in vivo*. Native fetal brain has a higher sGAG content than AB-ECM [221], and approximately one third of the sGAG content remains in the FB-ECM after decellularization, resulting in the FB-ECM having a significantly higher sGAG content than AB-ECM. The increased sGAG content suggests that that FB-ECM retains a higher ratio of functional components that can alter cellular function, survival, and growth [225].

VAD allows decellularization of delicate fetal brain tissue, and the resulting FB-ECM forms hydrogels with desirable characteristics. ECM is being investigated as a treatment for stroke,

and the gelation ability of ECM hydrogels *in vivo* is a critical factor that affects the host-biomaterial interface, distribution of the ECM within the cavity, and cell infiltrate composition at the injury site [98, 211, 226]. Injectable ECM hydrogels have also been investigated for spinal cord injuries, where ECM provides a platform for cell infiltration while providing neurotrophic factors to the surrounding tissue [227, 228]. AB-ECM treatment after traumatic brain injury showed decreased lesion volume, decreased white matter disruption, and increased behavioral outcomes [112]. Results show FB-ECM successfully forms a hydrogel, indicating FB-ECM hydrogels have a favorable composition to promote CNS remodeling *in vivo.*

To examine the effects of FB-ECM on primary neurons, RGC neuron survival and growth was tested *in vitro*. After 3 days in culture, there was no difference in viability between RGCs treated with FB-ECM and the media control indicating an undetectable effect on RGC viability. FB-ECM increased total neurite growth and longest axon growth, indicating factors FB-ECM regulates neuronal architecture in cultured RGCs. Embryonic RGCs have the intrinsic ability to regenerate, however this ability is lost soon after birth [78], partially due to amacrine signaling inhibiting RGC growth [26] and changes in gene expression [79, 80], and after birth RGCs only extend neurites by default when receiving peptide trophic factor signaling neurite growth [81]. In addition to loss of intrinsic growth ability, the embryonic ECM environment supports robust axon growth and development. During CNS development, ECM components regulate progenitor cell migration and differentiation [229, 230]. ECM composition changes during development and adulthood, with fetal ECM encouraging robust *de novo* cell and tissue growth and development due to the ECM constituent composition. Studies have shown that ECM derived from younger sources are more beneficial for cellular growth and proliferation, and thus may be more effective at promoting constructive remodeling after injury [113]. In a study comparing fetal, neonatal, and

adult cardiac ECM, fetal derived cardiac ECM showed the lowest cellular adhesion, but was able to induce significantly more cardiomyocyte differentiation compared to neonatal and adult derived ECM [116]. Matrix metalloproteases (MMPs) are highly expressed in the developing brain and during neural development. However, MMP expression levels rapidly declined during the first weeks after birth [231]. MMPs are suggested as regulators of synaptic activity [232], neurogenesis [233], cell migration, and axon guidance [234, 235]. Although not tested in this study, a higher concentration of MMPs in FB-ECM compared to AB-ECM could explain the differential regulation in axon growth observed *in vitro*.

After optic nerve crush, FB-ECM treatment can alter the default healing response. Previous studies have shown a significant increase in GFAP positive astrocyte activation after axonal injury [236, 237] which leads to increased glial scarring and axon growth inhibition. This study shows GFAP expression was decreased at the injury site following FB-ECM treatment, indicating FB-ECM may decrease scarring at the injury site. After CNS injury, reactive astrocytes contribute to glial scar formation. The response of reactive astrocytes depends on the location of the astrocytes relative to the injury. Soon after injury, the astrocytes closest to the injury site become hypertrophic and elongated, and start forming dense scar tissue [238]. The cellular composition of the scar varies, with the center populated with macrophages and microglia, while the periphery is densely populated with reactive astrocytes [239] that double in number compared to healthy tissue [240]. While the glial scar with high CSPG concentrations in the periphery prevents axonal outgrowth and regeneration, the scar is necessary to prevent injury from spreading to surrounding tissue. Additionally, ablating astrocytes have been shown to prevent glial scarring. However, astrocyte ablation increased chronic leukocyte infiltration, neuron degeneration, and inflammation, and prevented BBB repair [74, 241, 242]. These studies

indicate that astrocytes have a complex role in promoting adequate wound healing and they are partially responsible for neuronal regeneration failure.

Recently, matrix-bound vesicles (MBV) were found in all commercially and laboratory produced ECM [118]. MBV contain RNA cargoes, are bioactive, and have been shown to recapitulate cell responses induced by parent ECM [118, 119], including macrophage polarization [243]. Recent studies have shown pro-inflammatory microglia release cytokines, including IL-1α, TNF-α, and C1q, that act on astrocytes to polarize them to an A1 activation state, which in turn promotes RGC apoptosis [38]. Since MBV influence macrophage phenotype, it is hypothesized that MBV can also affect microglia phenotype and consequently astrocyte phenotype after injury. Although outside the scope of this study, MBV isolated from FB-ECM or cells treated with FB-ECM may offer an alternative to FB-ECM hydrogels [244] for CNS injury treatment. MBV can be delivered directly to the injured RGCs in the retina through minimally invasive intravitreal injections and future studies will investigate the application of MBV to injured RGCs after optic nerve crush.

FB-ECM application after optic nerve crush increases GAP-43 expression along the length of the optic nerve. The GAP-43 expression pattern observed in FB-ECM treated animals was not typical for that of a regenerating optic nerve axon as reported in previous studies [245, 246]. Several possible answers can be speculated to this observed pattern, and it is hypothesized the pattern may be due to an initial increase in axon regeneration, coupled with GAP-43 expression, followed by cessation of the regenerative response. At the point of tissue harvesting at day 14, there are no traces of FB-ECM remaining at the injury site or ocular cavity where the hydrogel is applied. It is possible that an initial axon growth response follows FB-ECM application while bioactive factors are actively secreted into the microenvironment. However, as the hydrogel

degrades and no longer secretes bioactive factors into the environment, there was no persistent regenerative response observed.

In this study, only one time point was included at day 14, therefore future studies will include earlier time points to determine whether there is an initial burst in axon growth as shown by GAP-43 staining. Additionally, co-labeling with cholera toxin subunit-B (CtxB) and GAP-43 will be done in future studies to determine whether the observed GAP-43 labeling is specific to neurons.

The GAP-43 labeling results were variable for FB-ECM treated animals, indicating FB-ECM treatment has the potential to alter the default healing response and promote axon regeneration after injury. However, ECM alone may not be an optimal solution. In order to deliver ECM to the injured optic nerve, the optic nerve sheath was fenestrated. Preliminary studies showed direct contact is needed between the ECM and optic nerve axon to elicit favorable cellular responses. However, the fenestration causes an additional injury, and the loss of cerebral spinal fluid from the incision can cause a decrease in pressure along the optic nerve and retina. Intravitreal delivery of MBV directly to the retina will offer an alternative approach to deliver bioactive factors within ECM to the injured ocular tissues.

In this study, used VAD was used to effectively decellularize fetal brain tissue, resulting in a biocompatible, injectable hydrogel. The FB-ECM increased RGC axon growth *in vitro* and altered the default healing response *in vivo* following optic nerve crush. These results permit new investigations into the mechanisms regulating healing in the CNS.

4.0 MATRIX BOUND NANOVESICLES PROMOTE RGC SURVIVAL AFTER ACUTE OPTIC NERVE INJURY

4.1 INTRODUCTION

CNS neurons fail to regenerate after injury, leading to permanently lost neurologic function. The visual system, including retinal ganglion cells (RGCs), forms part of the central nervous system (CNS), and injury and disease usually results in neuronal death and permanently lost visual function. The inability to regenerate is due to numerous intrinsic and extrinsic injury-induced factors that suppress axon regeneration. Constructive and functional tissue remodeling can be facilitated in the CNS by modulating the default innate immune response, especially in the acute post-injury period [211].

The pro-inflammatory innate immune response is an early factor that appears to modulate not only tissue remodeling but also neuronal connectivity and CNS neuron survival. Macrophage and microglia play a critical role in response to injury. After trauma, damaged cells release chemokines and other molecules [247, 248] that elicit inflammatory responses from neutrophils [249, 250], macrophages [251-254], and microglia [255] in the CNS. Depending on factors released in the local microenvironmental milieu, resident microglia and macrophages derived from circulating mononuclear cells can polarize toward either an M1-like, pro-inflammatory phenotype or an M2-like, anti-inflammatory, pro-repair phenotype [256]. After optic nerve injury, retinal microglia polarize toward an M1-like phenotype and secrete, among other factors, tumor necrosis factor-α (TNF-α), interleukin-1 α (IL-1 α), and complement protein C1q, which cause retinal

astrocyte polarization toward an A1-like, pro-inflammatory state which causes RGC cell death. Blocking TNF- α, IL-1 α, and C1q prevents microglial activation and increases RGC survival [38].

The innate immune response can be positively modulated by extracellular matrix (ECM) derived factors that modulate the phenotypic transition of macrophages and T-helper cells from a pro-inflammatory to a pro-remodeling, anti-inflammatory state. ECM bioscaffolds and their resident MBV have been shown to differentiate macrophages toward an M2-like, pro-remodeling phenotype [120], and MBV isolated from tissues such as porcine urinary bladder (UBM-ECM) can increase primary CNS neuron growth *in vitro* similar to UBM-ECM hydrogels [119]. Regenerative medicine strategies using inductive biologic scaffolds composed of ECM have been successful in numerous pre-clinical and clinical studies, and until recently the mechanism and factors contributing to the functional remodeling have been largely unknown. MBV are nano-sized lipid bound bodies found within in the ECM and recapitulate effects of the parent ECM from which they are derived [118, 120]. MBV are similar in size and structure to exosomes, but distinct with respect to cargo, surface markers, and compartmentalization. Whereas exosomes primarily exist in bodily fluids, MBV are localized to the collagen fibrils within all experimental and commercial ECM bioscaffolds analyzed to date [118]. Recent studies show MBV release during ECM scaffold degradation, suggesting MBV may be critical to promoting reparative, anti-inflammatory macrophage phenotypes [108]. Since MBV promote an anti-inflammatory phenotype in macrophages, the hypothesis for this study is that MBV will also promote an anti-inflammatory phenotype in microglia, thereby preventing A1-like astrocyte polarization and RGC cell death.

This study shows MBV are bioactive *in vitro* and *in vivo*. The effects of MBV derived from UBM-ECM were determined on primary RGC, microglia, and astrocytes *in vitro*, and RGC viability after acute ocular ischemia *in vivo*. MBV were non-cytotoxic to RGCs and increased RGC

neurite outgrowth after 3 days *in vitro* and suppressed the release of pro-inflammatory markers from primary microglia and astrocytes *in vitro.* MBV were injected intravitreally after acute ocular ischemia and, compared to controls, MBV increased RGC survival and photopic negative response (PhNR) amplitude as shown by electroretinography. These data support the hypothesis that MBV can modulate the default healing response in the CNS after injury and provide a minimally invasive approach to treating ocular and CNS trauma.

4.2 MATERIALS AND METHODS

4.2.1 Animals

Sprague-Dawley rats were provided by Charles River Laboratories (Wilmington, MA). Animal care and protocols complied with the University of Pittsburgh Institutional Animal Care and Use Committee and followed guidelines from the Guide for the Care and Use of Laboratory Animals published by the National Institutes of Health.

4.2.2 Urinary bladder extracellular matrix decellularization and hydrogel formation

Porcine urinary bladders from adult market weight pigs were provided by a local abattoir (Thoma's Meat Market, Saxonburg, PA, USA). Urinary bladders were decellularized as described [103, 121, 257]. Decellularization was confirmed using established methods to quantify DNA, including H&E staining and visualization through gel electrophoresis [121]. Decellularized urinary bladder extracellular matrix (UBM-ECM) was frozen, lyophilized, and stored at -20ºC until use. UBM-

ECM hydrogels at 10 mg/ml were made as previously described [121, 221]. Briefly, lyophilized UBM-ECM was milled to a powder, digested at 10 mg/ml with 1 mg/ml pepsin for 48 hrs, and the pH adjusted to 7.4.

4.2.3 Matrix bound nanovesicle (MBV) isolation

Lyophilized UBM-ECM was digested with Liberase TL (5401020001, Sigma-Aldrich) in Tris buffer (50mM Tris pH7.5, 5mM $CaCl_2$, 150mM NaCl) for 24 hrs at room temperature (RT) on an orbital rocker. Digested UBM-ECM was centrifuged at (10,000*g*, 30 mins). The MBV were pelleted by ultracentrifugation (100,000*g*, Beckman Coulter Optima L-90K Ultracentrifuge) at 4ºC for 2 hrs and further purified by size exclusion chromatography, using a Sepharose CL-2B resin. Purified MBV were stored at -80ºC until use. All MBV isolations were analyzed morphologically by transmission electron microscopy (TEM) as described [118]. MBV on TEM grids were observed at 80kV with a JEOL 1210 transmission electron microscope equipped with a high-resolution AMT digital camera.

4.2.4 Retinal ganglion cell isolation

RGCs were isolated from postnatal day three Sprague-Dawley rat pups as described [215]. Purified RGCs were seeded in neurobasal-SATO (nb-SATO) media at 3,000 RGCs per well in 96-well culture plates (087723B, Falcon) coated with poly-D-lysine for 1 hr at RT (70 kDa, 10 μg/ml, Sigma-Aldrich Corp., St. Louis, MO, USA) and laminin overnight (37ºC, 2 μg/ml, Sigma-Aldrich Corp.). MBV were resuspended in sterile PBS and added to RGC cultures in triplicate wells at

concentrations ranging from 5-80 μg/ml. UBM-ECM hydrogel (250 μg/ml) and nb-SATO media were used as controls. RGCs were cultured at 37°C, 10% CO_2 for 3 days.

4.2.5 RGC viability

RGC viability was analyzed using a calcein and propidium iodide live/dead kit per the manufacturer's instructions (Life Technologies, R37601). Briefly, the calcein and propidium iodide were mixed and incubated with the RGCs for 15 mins at RT. Five random non-overlapping fields were imaged per well at 20X using epi-fluorescence fluorescein and rhodamine filter sets (Zeiss, Axio Observer). Live and dead RGCs were quantified using ImageJ (National Institutes of Health, Bethesda, MD, USA). Data represent triplicates from three independent experimental repeats totaling at least 45 fields of view.

4.2.6 RGC neurite growth quantification

Neurite growth was analyzed as described [216, 258]. Briefly, RGCs were fixed with 4% paraformaldehyde (Alfa Aesar, 30525-89-4) in PBS for 15 min and then washed with PBS (3X). RGCs were permeabilized with 0.2% Triton X-100 in PBS for 15 mins, blocked with 1% BSA (Fisher Scientific) in PBS for 15 mins, and incubated overnight at 4ºC with anti-β III tubulin (1:300, TUJ-1, Millipore) in PBS. After incubation, RGCs were washed with PBS (3X), incubated in FITC-rabbit anti-chicken IgY H+L (1:150, Thermo Scientific) for 3 hrs at RT, washed with PBS (3X), and stained with DAPI (1:3000, Invitrogen) for 15 mins at RT. RGCs were washed with PBS (3X) and imaged at 20X (Zeiss, Axio Observer). For each well, total neurite growth was measured for the first ten RGCs randomly encountered that were not contacting another RGC using the

ImageJ plugin NeuronJ. Data represent total RGC neurite growth from triplicate wells in three experimental repeats, totaling at least 90 neurons per group.

4.2.7 Microglia cultures

Primary rat microglia (Lonza, R-G-535) were plated at 50,000 cells per well in 96-well plates per the supplier's recommendation. For all experiments, microglia were initially incubated for 24 hrs at 37ºC, 5% CO_2 to facilitate adherence. After 24 hrs, the supernatants were removed and replaced with fresh microglia media.

For unprimed microglia cultures, the following reagents were added to triplicate wells: microglia media only, lipopolysaccharide (LPS, 100 ng/ml) and interferon gamma (IFNγ, 20 ng/ml), interleukin-4 (IL-4, 20 ng/ml), UBM-ECM hydrogel (250 μg/ml), or MBV (5 μg/ml). After 24 hours, media was collected for ELISA analysis or to treat astrocytes.

For primed microglial cultures, microglia were treated with LPS (100 ng/ml) and IFNγ (20 ng/ml) for 6 hrs, supernatants removed, microglia rinsed with microglia media, and treated with the following in triplicate wells for an additional 24 hrs: microglia media, UBM-ECM (250 μg/ml), or MBV (5 μg/ml). After the additional 24 hrs incubation, supernatants were collected for ELISA assays or to treat astrocytes.

4.2.8 Astrocyte cultures

Primary rat astrocytes (ScienCell Research Laboratories, R1800) were plated at 5,000 cells per well in a 96-well plate per the supplier's instructions. Astrocytes were allowed to adhere for 24 hrs at 37ºC, 5% CO_2.

To determine the effect that microglia polarization has on astrocytes, microglia conditioned media, as described above, was added to triplicate astrocyte wells and incubated for 24 hrs. After initial 24 hr incubation with microglia conditioned media, astrocytes were rinsed with astrocyte media, incubated with fresh astrocyte media for an additional 24 hrs, and supernatants collected for ELISA assays.

To determine the effect of astrocyte supernatants on RGC viability, a transwell plate was used. Astrocytes were plated on the transwell insert at 5,000 cells per insert per the supplier's instructions, and the bottom chamber filled with astrocyte media. Astrocytes were allowed to adhere for 24 hrs at 37ºC, 5% CO_2. After initial 24 hr incubation, microglia conditioned media was added in triplicate to astrocytes in the insert and incubated for 24 hrs. After 24 hrs, the astrocytes were rinsed, and media replaced with fresh nb-SATO media for an additional 24 hrs. After incubation, the nb-SATO media in the bottom wells were collected for RGC cultures.

4.2.9 ELISA analysis

Microglia and astrocyte supernatants were analyzed IL-1β (R&D Systems, DY501), IL-6 (R&D Systems, DY506), and TNF-α (BioLegend, Cat. # 438204) expression according to manufacturer's instructions. Duplicate samples were analyzed from three independent experimental repeats.

4.2.10 Retinal ganglion cell responses to astrocyte conditioned media

RGCs were isolated and plated as described above and allowed to adhere for 24 hrs at 37ºC, 10% CO_2. To determine the effects of astrocyte conditioned media on RGC survival, supernatants from astrocytes were collected as described and added to RGC wells in triplicate and incubated for 72

hrs at 37ºC, 10% CO_2. RGC viability from three independent experiments was analyzed as described above.

4.2.11 In vivo MBV dose response

RGC survival was tested with three doses of MBV *in vivo:* 5, 10, and 20 μg/ml (n=5 animals per group). Animals were anesthetized via isoflurane inhalation (3% induction, 1.5% maintenance). One drop proparacaine hydrochloride ophthalmic solution (Bausch & Lomb, Inc., Rochester, NY) and one drop tropicamide ophthalmic solution (Akorn, Lake Forest, IL) were topically applied to both eyes of twenty animals to induce analgesia and pupil dilation, respectively. An 18g needle was used to make a small hole in the sclera immediately posterior to the limbus. Under a surgical microscope, a Hamilton micro-syringe was inserted into the vitreous through the scleral opening. The needle tip was placed as close as possible to the optic nerve head, and care was taken not to touch the retina or lens. MBV were diluted in sterile PBS to the appropriate concentrations. All injection volumes were 1 μl, and sterile PBS was used as vehicle control (n=5 per group). 1 μl of MBV or PBS were injected into the vitreous and the needle was held in place for 30 secs to allow the MBV or PBS to diffuse into the vitreous. The needle was removed and one drop gentamicin antibiotic ointment (Akorn, Lake Forest, IL) was applied topically immediately after removal of the needle. The animals received two additional injections at days 2 and 7 using the same techniques described. Animals were sacrificed 14 days after MBV injection and retinas removed for RGC quantification.

4.2.12 Intraocular pressure elevation with MBV treatment

Acute intraocular pressure (IOP) elevation was induced as previously described in chapter 2. Fifty-seven animals received IOP elevation in the right eye only via saline anterior chamber perfusion and the left eyes served as uninjured control. Animals were anesthetized with an intraperitoneal injection of a 75:10 mg/kg ketamine/xylazine cocktail, and anesthesia was confirmed with a toe pinch reflex. One drop each of proparacaine and tropicamide were applied to the right eyes to induce analgesia and pupil dilation, respectively. A 30g needle was connected to a sterile saline reservoir (0.9% sodium chloride; Baxter International Inc., Deerfield, IL) and the needle tip inserted into the anterior chamber. The needle was inserted parallel to the iris using a surgical microscope and secured in place. The saline reservoir was elevated to increase the IOP from 15 mmHg to 130 mmHg and secured in place for 60 mins. The IOP was measured using a pressure transducer (BIOPAC Systems, Goleta, CA, USA) and a handheld tonometer. After 60 mins, the saline reservoir was lowered, and the needle removed from the anterior chamber. One drop gentamicin was applied to the eye immediately after removing the needle. Nineteen animals (n=10 for histology, n=5 for ERG, n=4 for MEMRI) received 1 µl of 5 µg/ml MBV treatment immediately after IOP elevation, and at days 2 and 7 after IOP elevation, using the injection technique described in the previous section. Nineteen animals (n=10 for histology, n=5 for ERG, n=4 for MEMRI) were used for vehicle controls and received 1 µl of sterile PBS injected intravitreally immediately after IOP elevation and at days 2 and 7 after IOP elevation. Nineteen animals (n=10 for histology, n=5 for ERG, n=4 for MEMRI) received IOP elevation without any injections.

4.2.13 Cholera toxin subunit B injection

Five animals per group received cholera toxin subunit B (CtxB) injections on day 11, three days prior to sacrifice on day 14. Cholera toxin subunit B (recombinant), Alexa Fluor 594 Conjugate (LifeTech, Cat # C3477) was resuspended in sterile PBS to yield a 1% solution. Animals were anesthetized via isoflurane inhalation (3% induction, 1.5% maintenance). Intravitreal injection technique was used as described in the previous section, and 2 µl of the 1% CtxB solution was injected into the vitreous. The Hamilton syringe needle was held in place for 30 secs before removal, and one drop gentamicin applied topically after removing the needle from the eye.

4.2.14 Immunohistochemistry

Ten animals per group were used for immunohistochemistry. Animals were sacrificed, and the retinas and optic nerves removed and fixed in 4% paraformaldehyde in PBS for 30 mins. Retinas and optic nerves were rinsed three times in PBS for 5 mins each.

Retinas were quartered and permeabilized/blocked in IHC blocking buffer (3% Triton X-100, 0.5% Tween-20, 1% BSA, and 0.1% sodium azide in PBS) for 2 hrs at RT on a shaker at 60 RPM. Retinas from animals that received CtxB injections were labeled with 1:250 anti-CtxB (Mouse anti-CtxB, Abcam, AB62429) in IHC blocking buffer, and remaining retinas were co-labeled with 1:250 anti-RNA-binding protein with multiple splicing (Rabbit anti-RBPMS, Phosphosolutions, 1830-RBPMS) and 1:250 anti-Brn3A (Mouse anti-Brn3A, Santa Cruz, SC-8429) in IHC blocking buffer for 48 hrs at 4ºC on a shaker at 60 RPM. Retinas were rinsed three times with 0.3% Tween-20 in PBS and incubated in 1:500 Alexa Fluor 488 donkey anti-rabbit (Abcam, AB150073) and Alexa Fluor 555 goat anti-mouse (Abcam, AB150114) in IHC blocking

buffer for 24 hrs at 4ºC on a shaker at 60 RPM. Retinas were rinsed three times with 0.3% Tween-20 in PBS, mounted on glass microscope slides, coverslipped with Vectashield (Vector Laboratories, H-1200), and imaged with epi-fluorescence (Zeiss, Axio Observer). Previous studies showed IOP elevation causes higher RGC cell death at the periphery of the retina [259], therefore RGC survival was analyzed at two locations. Similar to previous quantification methods[260], retinas were quartered prior to staining and three images were taken at the periphery and the center retina (around the optic nerve head) on each quarter section, thereby totaling 12 images at the periphery and 12 images at the center per retina..

Optic nerves were embedded in paraffin and sectioned on a cryostat in 15 µm sections. Sections were blocked/permeabilized in IHC blocking buffer for 2 hrs at RT and rinsed twice with 0.3% Tween-20 in PBS. Sections were labeled with 1:500 anti-GAP43 (Rabbit anti-GAP-43, Abcam, AB16053), 1:500 anti-GFAP (Rabbit anti-GFAP, 1:500, Abcam, AB7260), or 1:250 anti-CtxB (Mouse anti-CtxB, Abcam, AB62429) for 24 hrs at 4ºC. The sections were rinsed three times with 0.3% Tween-20 in PBS and incubated in 1:500 Alexa Fluor 488 donkey anti-rabbit (Abcam, AB150073) or Alexa Fluor 555 goat anti-mouse (Abcam, AB150114) in IHC blocking buffer for 24 hrs at 4ºC. Sections were rinsed twice with 0.3% Tween-20 in PBS and incubated with 4 µg/ml Hoechst stain (Sigma-Aldrich, H6024) in IHC blocking buffer for 15 mins at RT. The sections were rinsed three times with 0.3% Tween-20 in PBS, mounted on a cover slip with Vectashield, and imaged with epi-fluorescence (Zeiss, Axio Observer). The signal intensities were measured with ImageJ as previously described [218, 258]. Fifteen regions of interest (ROIs) were drawn evenly distributed along the optic nerve and four ROIs were drawn on the image background. The area, mean fluorescence and integrated density was measured for each image and the signal

intensity calculated based on the following equation: CTCF = integrated density – (area x mean background fluorescence).

4.2.15 Electroretinography

ERG functional analysis was done according to an established protocol [261]. In brief, animals were anesthetized with an intraperitoneal injection of a 75:10 mg/kg ketamine/xylazine cocktail, and anesthesia was confirmed with a toe pinch reflex. One drop each of proparacaine and tropicamide were applied to each eye to induce analgesia and pupil dilation, respectively, and eyes were kept lubricated with Goniovisc 2.5% (Sigma Pharmaceuticals, Item #9050) during recordings. Two gold loop electrodes were placed on the cornea, the reference electrode was inserted into the inside of the cheek, and the ground lead electrode was inserted into the quadricep. Bilateral ERG recordings were done simultaneously from both eyes during the trials using a color-light dome. In general, one step of a fixed intensity light was illuminated for 1 ms and the ERG response recorded as a sweep over multiple steps of increasing illumination. Fifty ERG responses were recorded per trial, and a total of three trials were done per light intensity step. The data were analyzed by measuring the Photopic Negative Response (PhNR) and the implicit time of the different waves recorded.

4.2.16 Manganese enhanced MRI

Manganese enhanced MRI (MEMRI) was used to analyze active axonal transport along the visual pathway. Mn^{2+} ions act as calcium analogue and enter calcium channels during neuronal activity from where they are transported along axonal pathways via microtubules. MEMRI was done on

for n=4 animals per group. Each animal received 1.5 µl bilateral injections of 100 mM $MnCl_2$. T1-weighted MEMRI was done before $MnCl_2$ injections, and again at 8 hours after injections with a fast spin echo imaging sequence. Slices were oriented orthogonal to the pre-chiasmatic optic nerve. Other imaging parameters include: TR/TE = 600/8 ms, echo train length = 8, number of slices = 8, and slice thickness = 1 mm. A saline phantom was placed next to the rodent head for signal normalization. Signal intensities were measured in the left and right optic nerves, lateral geniculate nucleus (LGN), and superior colliculus (SC) using ImageJ. Mn signal enhancement was calculated as percentage difference in normalized T1-weighted signal intensity between injured and uninjured optic nerves, LGN, and SC and compared between groups.

4.2.17 Statistical analysis

All analysis and measurements were done by blinded individuals. One-way analysis of variance (ANOVA) and post-hoc Tukey's test was used to determine significant differences between groups with $p<0.05$. Graphs represent the mean with error bars indicating standard error of the mean (SEM) unless otherwise noted.

4.3 RESULTS

4.3.1 MBV are non-cytotoxic to RGC and increase RGC neurite growth in vitro

Consistent with previous studies investigating the effects of MBV on primary neuronal cultures [119], *in vitro* studies suggest MBV derived from UBM-ECM are non-cytotoxic and increase RGC

neurite growth compared to media and UBM-ECM hydrogels (Fig. 18). After 3 days *in vitro,* there was no difference in RGC survival between groups treated with any of the five MBV concentrations, UBM-ECM, or media, indicating UBM-ECM and MBV are non-cytotoxic at the concentrations tested (Fig. 18B). In contrast to RGC viability studies, MBV increased RGC neurite length after 3 days *in vitro* (Fig. 18C). 5, 10, or 20 µg/ml MBV significantly increased RGC neurite growth to 621.5 ± 35.2 µm, 652.4 ± 23.2 µm, and 596.0 ± 32.3 µm, respectively, compared to media (275.2 ± 11.6 µm) and UBM-ECM (348.3 ± 12.1 µm) controls. 50 and 80 µg/ml MBV did not increase RGC neurite growth at 191.6 ± 9.9 µm and 76.4 ± 4.3 µm, respectively.

4.3.2 MBV suppress pro-inflammatory cytokine secretion from microglia and astrocytes

In vitro studies show MBV suppress pro-inflammatory cytokine secretion from microglia and astrocyte (Fig. 19). Primary microglia were primed with LPS/IFNγ to induce a pro-inflammatory M1-like phenotype, and subsequently treated with media (control), UBM-ECM, or MBV isolated from UBM-ECM to determine whether UBM-ECM and MBV can suppress pro-inflammatory cytokine secretion (Fig. 19 A, B, C, G). Microglia treated with LPS/ IFNγ for 24 hrs (unprimed) had increased release of IL-1β, IL-6, and TNF-α in the secretome. Analysis of the secretome of microglia primed with LPS/IFNγ for 6 hrs and then treated with media resulted in a comparable increased release IL-1β, IL-6, and TNF-α, indicating the microglia continued to release pro-inflammatory cytokines after the supernatant was removed and replaced with media. Finally, microglia primed with LPS/IFNγ for 6 hrs and treated with UBM-ECM or MBV showed IL-1β, IL-6, and TNF-α expression levels similar to microglia only treated with media for 24 hrs, indicating the UBM-ECM and MBV treatment for 24 hrs after LPS/IFNγ priming suppresses the release of pro-inflammatory cytokines

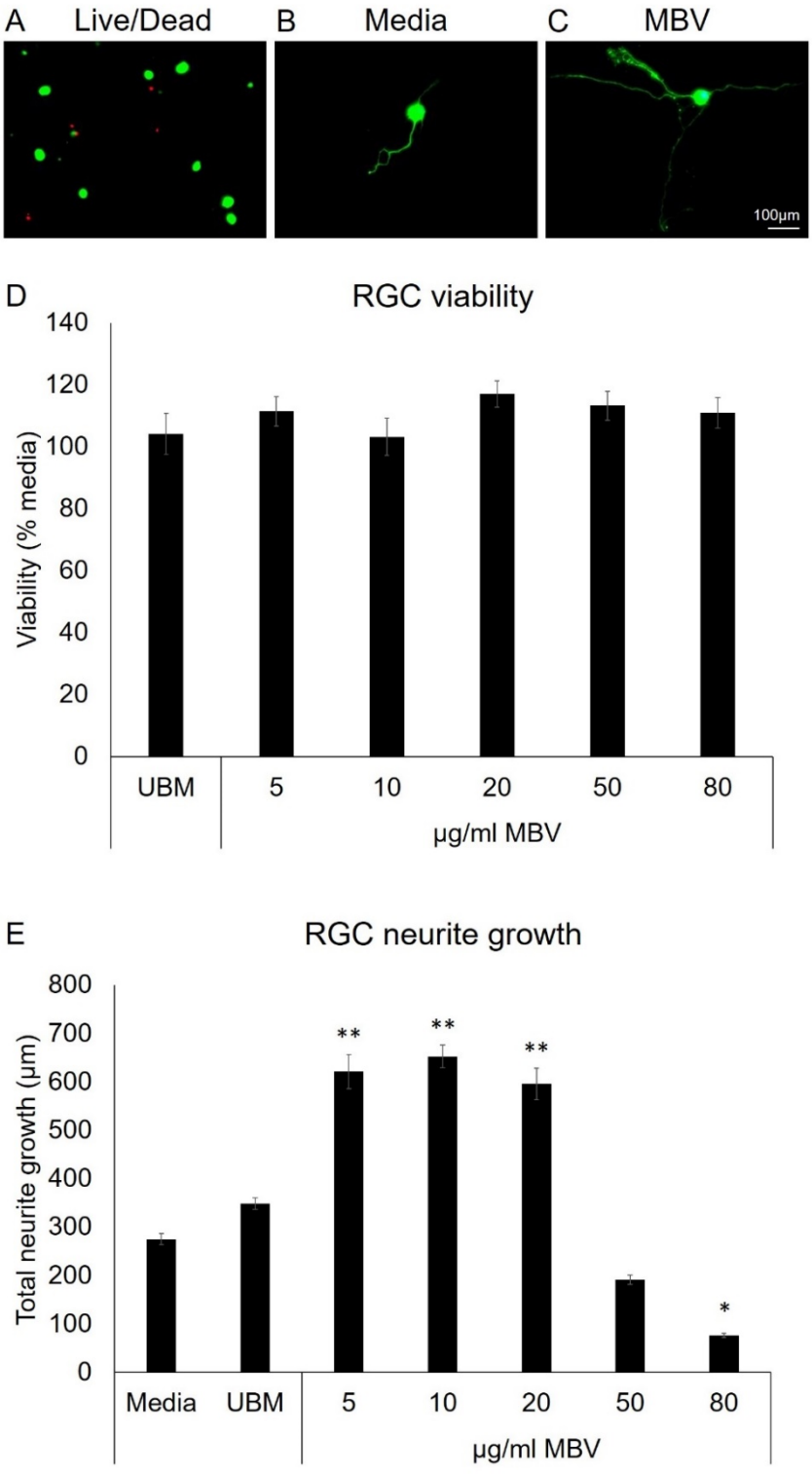

Figure 18. MBV increases RGC neurite growth. A-C representative images of RGC A. survival and growth in B. media and C. MBV. D. RGC viability was unchanged by UBM-ECM and MBV Data is normalized to media control. E. Total neurite growth was increased by 5, 10, and 20 µg/ml MBV.

Analysis of the astrocyte secretome showed comparable results and trends as the microglia results (Fig. 19 D, E, F, H). Astrocytes treated with supernatants from unprimed microglia treated with LPS/IFNγ showed increased expression of IL-1β, IL-6, and TNF-α, indicating the secretome from pro-inflammatory microglia upregulate the release of pro-inflammatory markers from astrocytes. The secretome from LPS/IFNγ primed microglia treated with media induced a similar upregulated expression of IL-1β, IL-6, and TNF-α from astrocytes, while the secretome from microglia primed with LPS/IFNγ and treated with UBM-ECM or MBV did not increase the expression of pro-inflammatory markers by astrocytes. These results indicate UBM-ECM and MBV treatment following microglia priming can down regulate microglia pro-inflammatory cytokine secretion and prevent secretion of pro-inflammatory cytokines by astrocytes.

4.3.3 MBV suppress pro-inflammatory cytokine secretion which increases RGC survival in vitro

RGC were treated with astrocyte supernatants, and results showed treating microglia with LPS/IFNγ, or priming with LPS/IFNγ, and subsequent treatment with media resulted in 100% RGC cell death, while UBM-ECM or MBV treatment after microglia priming increased RGC viability and prevented RGC cell death (Fig. 20). These results correspond with previous studies showing microglia M1-like polarization affects RGC viability via astrocyte A1-like polarization [38], and support the hypothesis that promoting an anti-inflammatory microglia phenotype over a pro-inflammatory phenotype will increase RGC survival after injury.

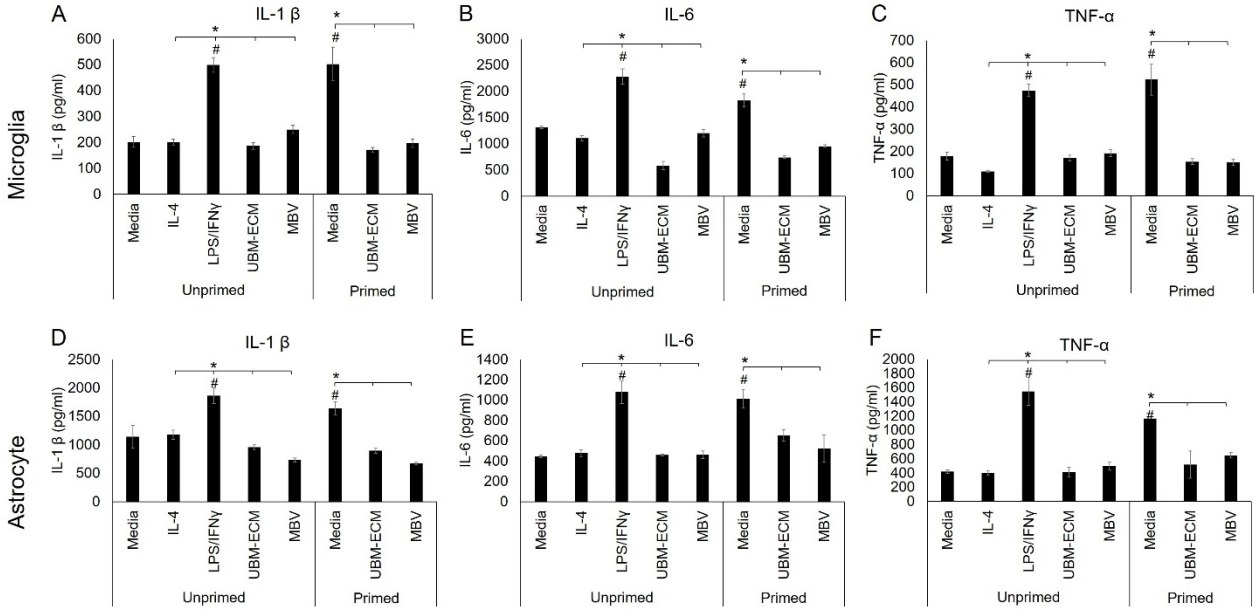

G

Microglia	Condition	IL-1β (μg/ml)	IL-6 (μg/ml)	TNF-α (μg/ml)
Unprimed	Media	202.4 ± 20.4	1314.8 ± 26.7	178.2 ± 18.2
	IL-4	201.6 ± 12.7	1105.5 ± 48.2	109.5 ± 5.9
	LPS/IFNγ	499.6 ± 28.4	2283.0 ± 142.9	474.5 ± 27.6
	UBM-ECM	186.4 ± 13.9	584.3 ± 76.3	169.8 ± 13.5
	MBV	250.2 ± 16.0	1199.4 ± 69.6	191.9 ± 16.4
Primed	Media	502.6 ± 65.1	1825.9 ± 120.4	524.6 ± 70.6
	UBM-ECM	171.3 ± 9.6	737.2 ± 26.4	153.5 ± 13.45
	MBV	197.2 ± 17.1	952.3 ± 24.9	150.0 ± 12.7

H

Astrocytes	Condition	IL-1β (μg/ml)	IL-6 (μg/ml)	TNF-α (μg/ml)
Unprimed	Media	1141.3 ± 201.3	446.1 ± 13.3	421.0 ± 21.6
	IL-4	1176.0 ± 79.5	477.6 ± 30.8	399.5 ± 36.5
	LPS/IFNγ	1860.4 ± 140.6	1080.1 ± 113.1	1546.2 ± 196.5
	UBM-ECM	957.8 ± 42.8	461.4 ± 8.0	413.6 ± 67.1
	MBV	731.2 ± 33.4	463.1 ± 36.6	497.9 ± 53.1
Primed	Media	1642.0 ± 110.3	1013.2 ± 88.8	1165.7 ± 190.0
	UBM-ECM	893.9 ± 46.9	652.3 ± 55.8	517.2 ± 39.7
	MBV	671.5 ± 24.0	523.3 ± 136.9	678.7 ± 15.5

Figure 19. MBV decrease pro-inflammatory cytokine secretion from both microglia and astrocytes. A-C. In unprimed microglia, LPS/IFNγ increased pro-inflammatory cytokine secretion. In primed microglia, IL-1β, IL-6, and TNF-α secretion remained elevated when treated with media, but the secretion of all three cytokines was reduced by both UBM-ECM and MBV. D-F. Similar to microglia, LPS/IFNγ increased pro-inflammatory cytokine secetion from astrocytes and these increases were decreased by both UBM-ECM and MBV.

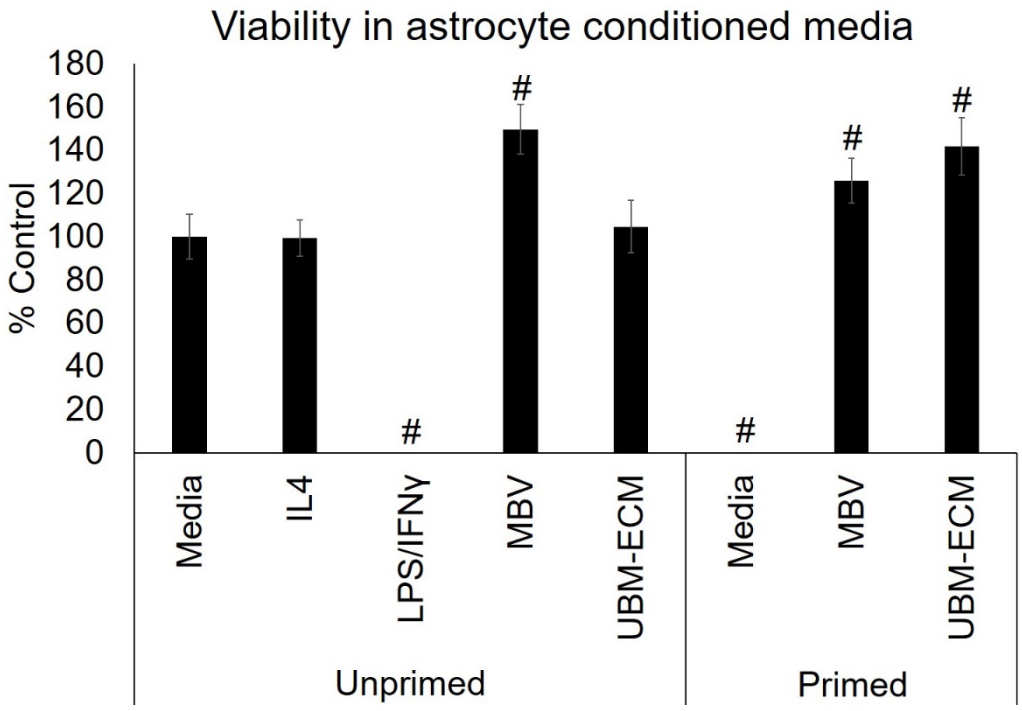

Figure 20. MBV increase RGC survival in conditioned media from pro-inflammatory astrocytes. RGCs were treated with media from astrocytes cultured with microglia primed and unprimed media. RGCs treated with primed-MBV or primed-UBM-ECM media showed increased survival compared to primed-media group.

4.3.4 MBV are non-cytotoxic at low concentrations in vivo

Initial *in vivo* studies were conducted to determine which concentrations of MBV are non-cytotoxic after intravitreal injection. RGC viability was quantified around the optic nerve head (Central) and around the periphery of the retina (Periphery) and results shown as percentage viable RGC as compared to uninjected control (Fig. 21). RGC viability around the periphery was unchanged after MBV and PBS injections compared to uninjected control. RGC viability in the central region was decreased to 82.8 ± 1.9% and 80.7 ± 4.4% of the uninjected control eyes

following the injection of 10 µg/ml and 20 µg/ml, respectively, while injection of 5 µg/ml MBV (104.4 ± 4.1%) and PBS (97.4 ± 3.0%) had no effect on RGC viability. The 5 µg/ml MBV concentration was therefore chosen for IOP elevation *in vivo* experiments.

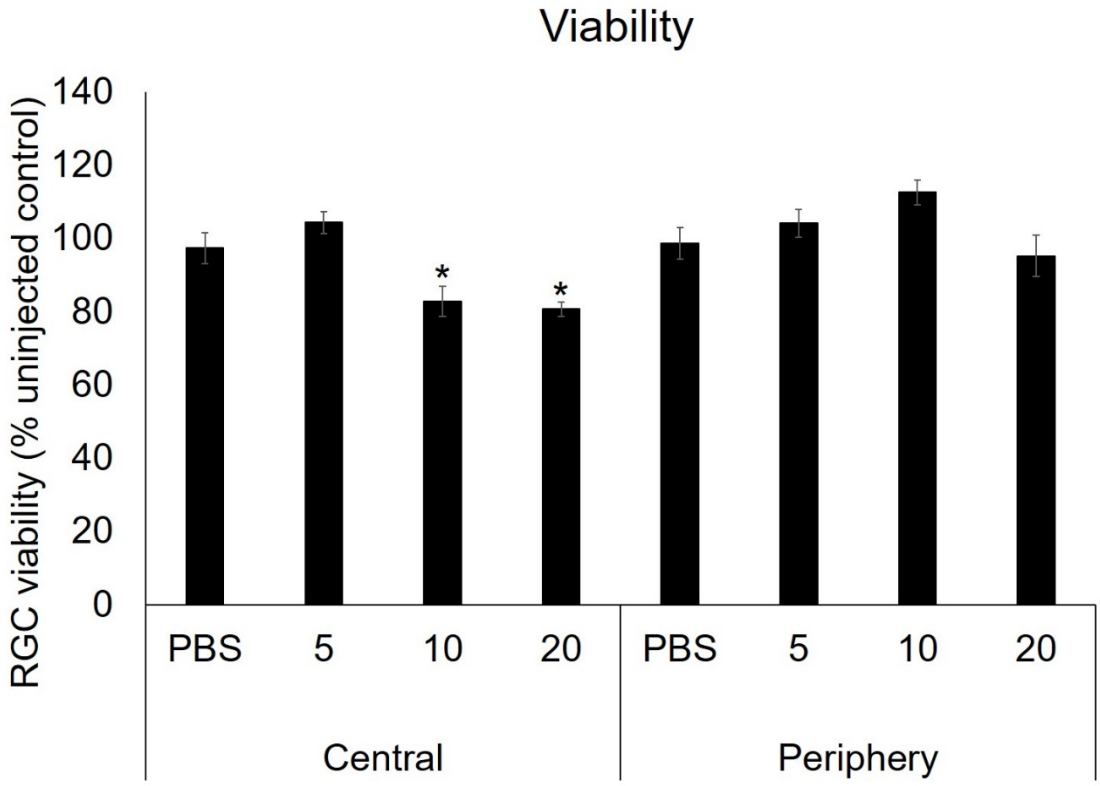

Figure 21. MBV toxicity in vivo. Three concentrations of MBV, 5, 10, and 20 ug/ml, were injected intravitreally at 0, 2, and 7 days into healthy, uninjured eyes. Compared to uninjected control, RGC viability was unaffected by either PBS or MBV at 5 ug/ml.

4.3.5 MBV increase RGC survival after IOP elevation

Following IOP elevation, 5 µg/ml MBV were injected intravitreally immediately after IOP elevation, and at days 2 and 7 and resulted in a significant increase in RGC viability (Fig. 22). RGC viability was analyzed 14 days after IOP elevation, and IOP elevation only and IOP elevation with PBS injection resulted in significantly decreased RGC viability in the central retina with 47.4 ± 2.3% and 41.8 ± 2.3% RGC survival compared to uninjured control. MBV treatment caused significant increase in RGC survival in the central retina compared to the two untreated groups, with 79.5 ± 3.8% survival. Similarly, in the peripheral retina, IOP elevation only and IOP elevation with PBS caused a significant decrease in RGC viability at 36.3 ± 3.6% and 26.4 ± 2.8% RGC survival, respectively, compared to uninjured controls. MBV treatment significantly increased RGC survival to 75.9 ± 4.2% compared to uninjured controls.

4.3.6 MBV increase RGC axon survival after IOP elevation

CtxB labeling in the retina showed intact axon labeling in the central and peripheral retina in the healthy control group and decreased axonal labeling in the IOP elevation and IOP elevation with PBS injection groups (Fig. 23A). Animals treated with MBV showed intact axon labeling similar to healthy control groups, indicating the MBV treatment preserves RGC axons in addition to RGC cell bodies in the retina. In the optic nerves (Fig. 23B), the IOP elevation and IOP elevation with PBS injection groups showed significantly decreased CtxB labeling at 32.5 ± 6.3% and 26.8 ± 4.4% of uninjured control, respectively (Fig. 23C). CtxB labeling in the MBV treated optic nerves was significantly decreased compared to uninjured controls at 78.6 ± 6.1% of controls and was

significantly increased compared to both IOP elevation and IOP elevation with PBS injection groups.

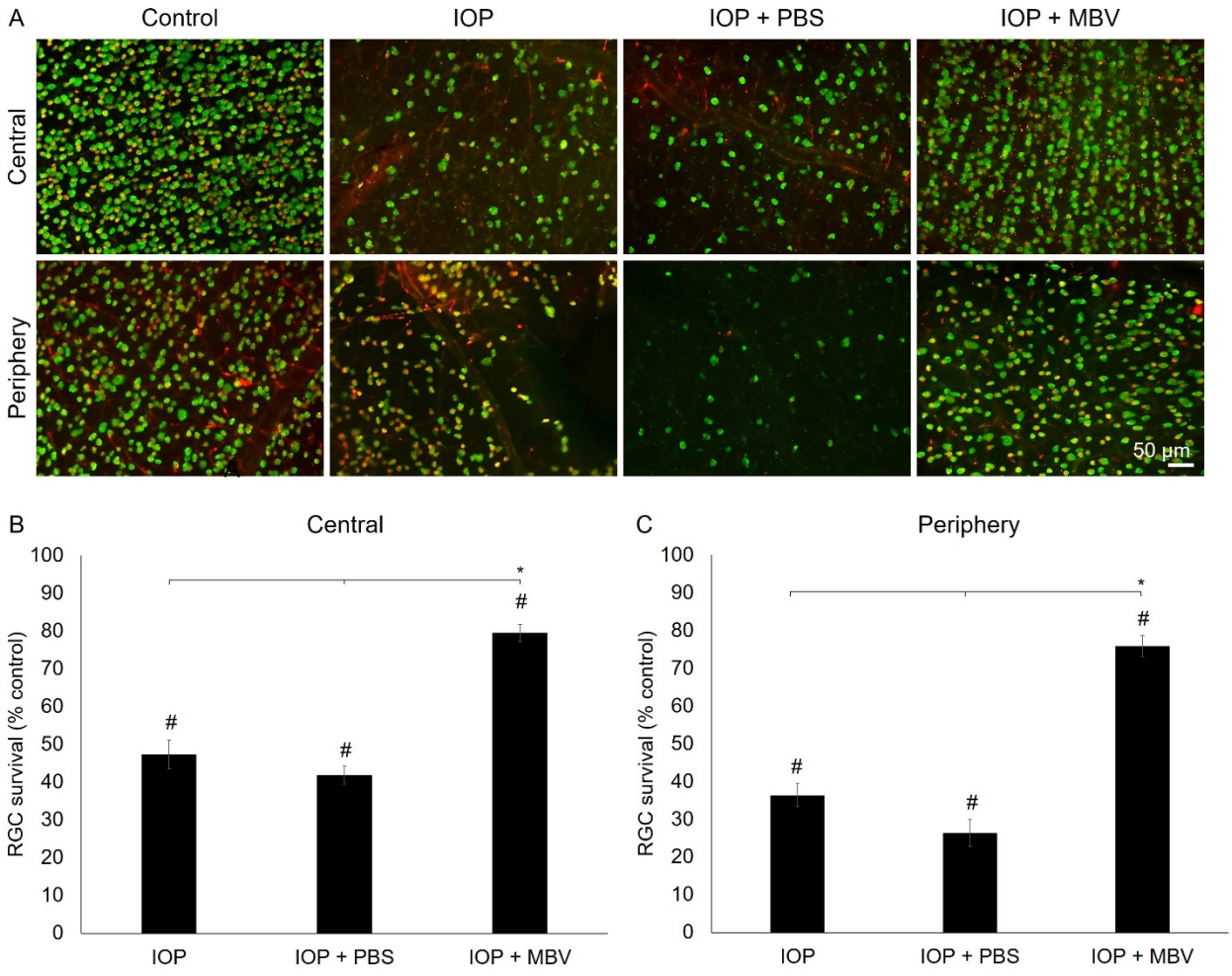

Figure 22. MBV reduced RGC loss induced by elevated IOP. A. Representative images showing RGC cell bodies co-labeled with RBPMS and Brn3A. B, C. IOP elevation and IOP elevation with PBS injections caused a significant decrease in RGC survival. IOP elevation with MBV injections caused significant increase in RGC viability compared to IOP elevation only and IOP elevation with PBS injections

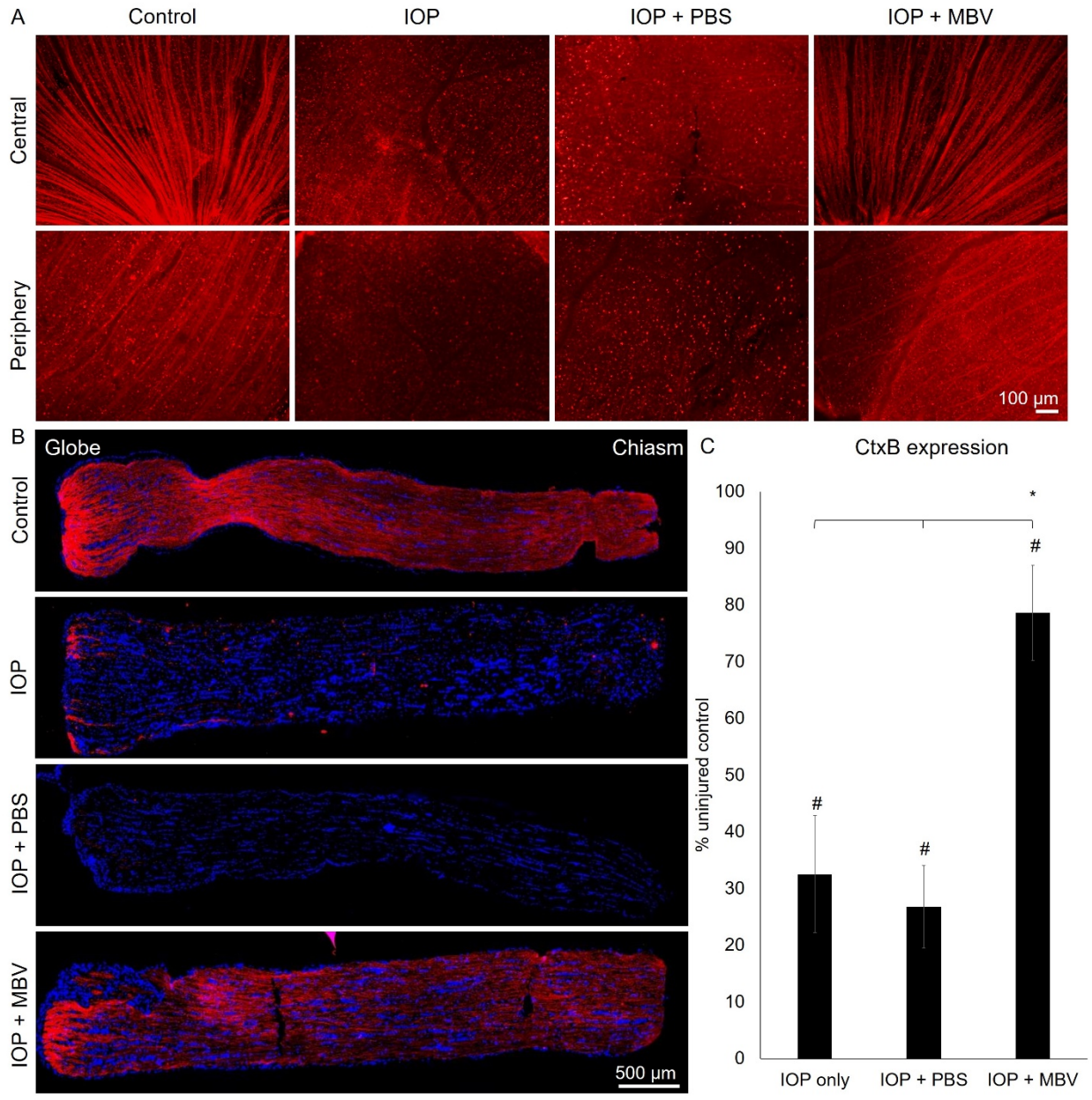

Figure 23. After IOP elevation, MBV decreases RGC axon degeneration. Representative images showing RGC axons labeled with CtxB in the A. retina and B. optic nerve. C. IOP elevation and IOP elevation with PBS injections caused a significant decrease in RGC axon survival, IOP elevation with MBV injections caused significant increase in RGC axon viability

4.3.7 MBV decrease GFAP expression after IOP elevation

To analyze the effect of MBV on astrocyte activation *in vivo*, GFAP expression along the length of the optic nerve was analyzed (Fig. 24A). Compared to uninjured control nerves, GFAP expression significantly increased in the IOP elevation and IOP elevation with PBS injection groups, which is consistent with typical astrocyte migration and activation after optic nerve injury. Quantitatively, IOP elevation and IOP elevation with PBS significantly increased GFAP expression to 393 ± 22.7% and 413.7 ± 26.3%, respectively, compared to uninjured control (Fig. 24B). Qualitatively and quantitatively the optic nerves of animals treated with MBV after IOP elevation showed decreased GFAP expression, and there was no significant difference (107.7 ± 6.4% increase) in GFAP expression between uninjured control optic nerves and MBV treated optic nerves.

4.3.8 MBV increase GAP43 expression after IOP elevation

To determine if MBV can increase RGC axon growth *in vivo,* the expression of the axon growth marker GAP-43 was analyzed (Fig. 25A). Compared to uninjured control nerves, GAP43 expression was significantly decreased in IOP elevation and IOP elevation with PBS injection groups at 77.5 ± 7.2% and 77.8 ± 8.4% of uninjured controls, respectively (Fig. 25B). Optic nerves of animals treated with MBV showed increased GAP43 expression, and there was no difference (108.6 ± 6.1%) in GAP43 expression between uninjured control and MBV treated optic nerves.

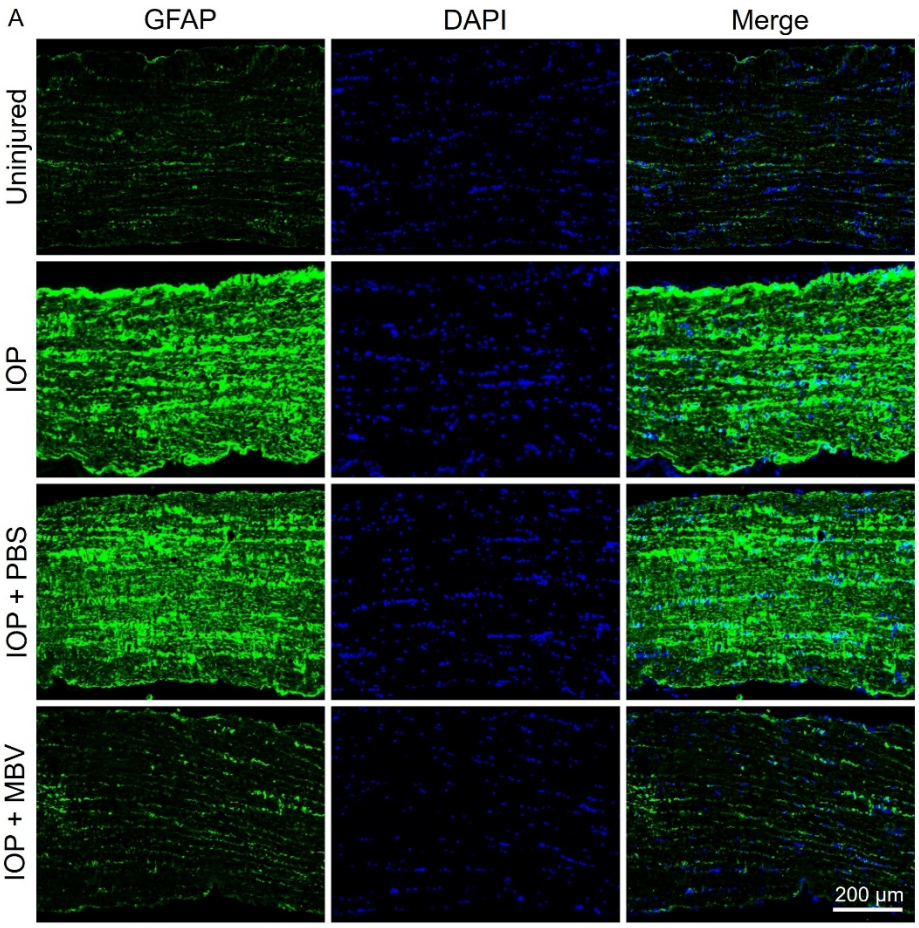

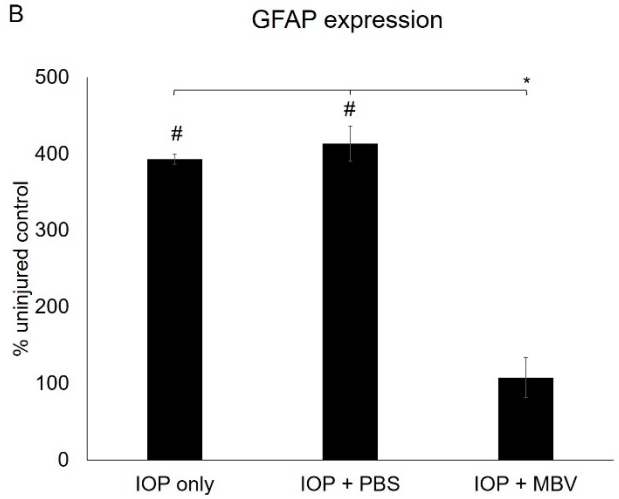

Figure 24. MBV decreases IOP induced GFAP expression in the optic nerve. A. Representative images of optic nerves labeled with GFAP. B. GFAP expression was increased following IOP elevation and IOP elevation with PBS injections. MBV injections decreased GFAP expression compared to untreated groups, and there was no difference in GFAP expression between MBV treated and uninjured animals.

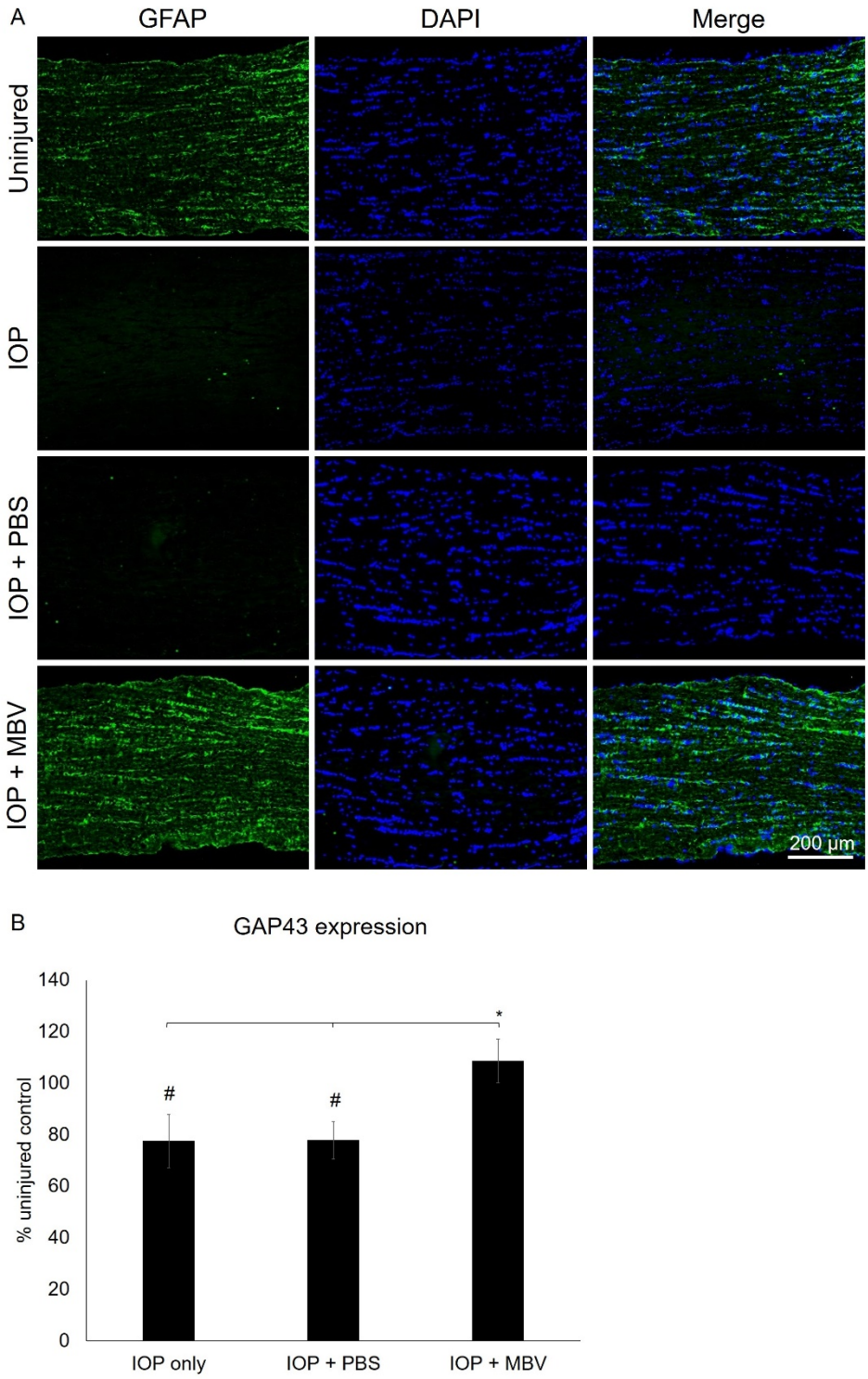

Figure 25. MBV increases GAP-43 expression in the optic nerve. A. Representative images of optic nerves labeled with GAP-43. B. GAP-43 expression was decreased following IOP elevation and IOP elevation with PBS injections. MBV injections increased GAP-43 expression compared to untreated groups, and there was no difference in GAP-43 expression between MBV treated and uninjured animals.

4.3.9 MBV improve retinal electrical function after IOP elevation

Photopic negative response (PhNR) amplitude and latency were recorded using electroretinography (ERG) (Fig. 26). Compared to uninjured control eyes, IOP elevation and IOP elevation with PBS injection significantly decreased PhNR amplitude by 32.8 ± 4.4% and 42.0 ± 16.8%, while there was no difference in PhNR amplitude between uninjured control and MBV treated eyes (Fig. 26C). Latency analysis showed IOP elevation significantly increased latency by 16.6 ± 4.0% compared to uninjured control group, while IOP elevation with PBS injection and MBV treatment had no significant effect on latency (Fig. 26D).

4.3.10 MBV decrease Mn transport deficits in the visual system

Mn transport along the visual pathway was assessed in the optic nerve, LGN, and SC projected from the left and right eyes by quantifying the normalized signal intensity before (pre-MEMRI) and 8 hours after (post-MEMRI) $MnCl_2$ injections (Fig. 27). No differences in percentage signal intensity were observed in the optic nerves for any of the three groups. In both the LGN an SC, percentage signal intensity differences were observed for the IOP only and IOP with PBS animals, and there was no difference in the LGN or SC for the IOP with MBV animals.

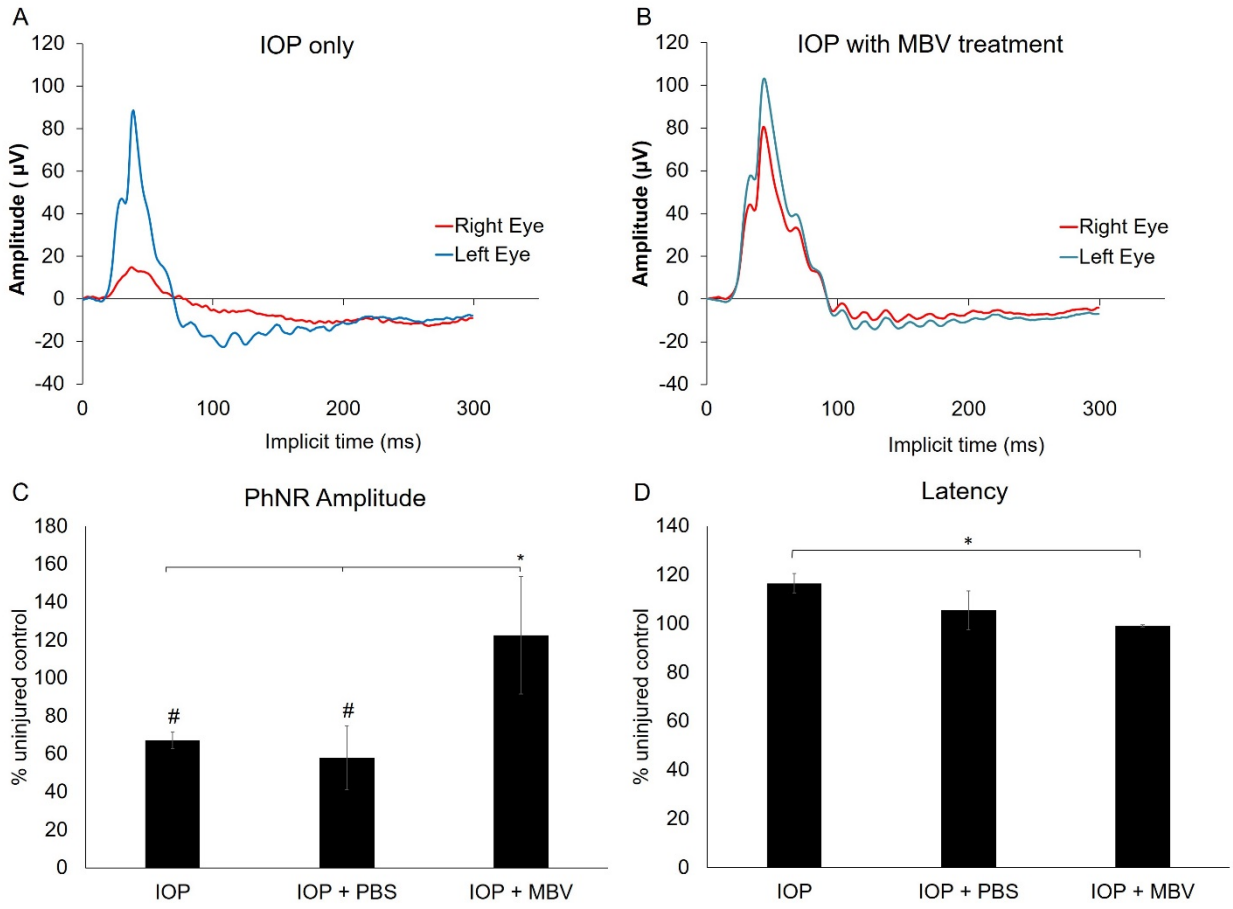

Figure 26. MBV prevents IOP induced decreases in the retinal photopic negative response (PhNR) and increases in the PhNR latency. IOP elevation with and without PBS injection decreased the photopic negative response (PhNR) amplitude. MBV treatment increased the PhNR amplitude compared to untreated groups and there was no difference in PhNR amplitude between uninjured and MBV treated groups. IOP elevation decreased latency of the PhNR and was significantly increased compared to IOP elevation with MBV treatment.

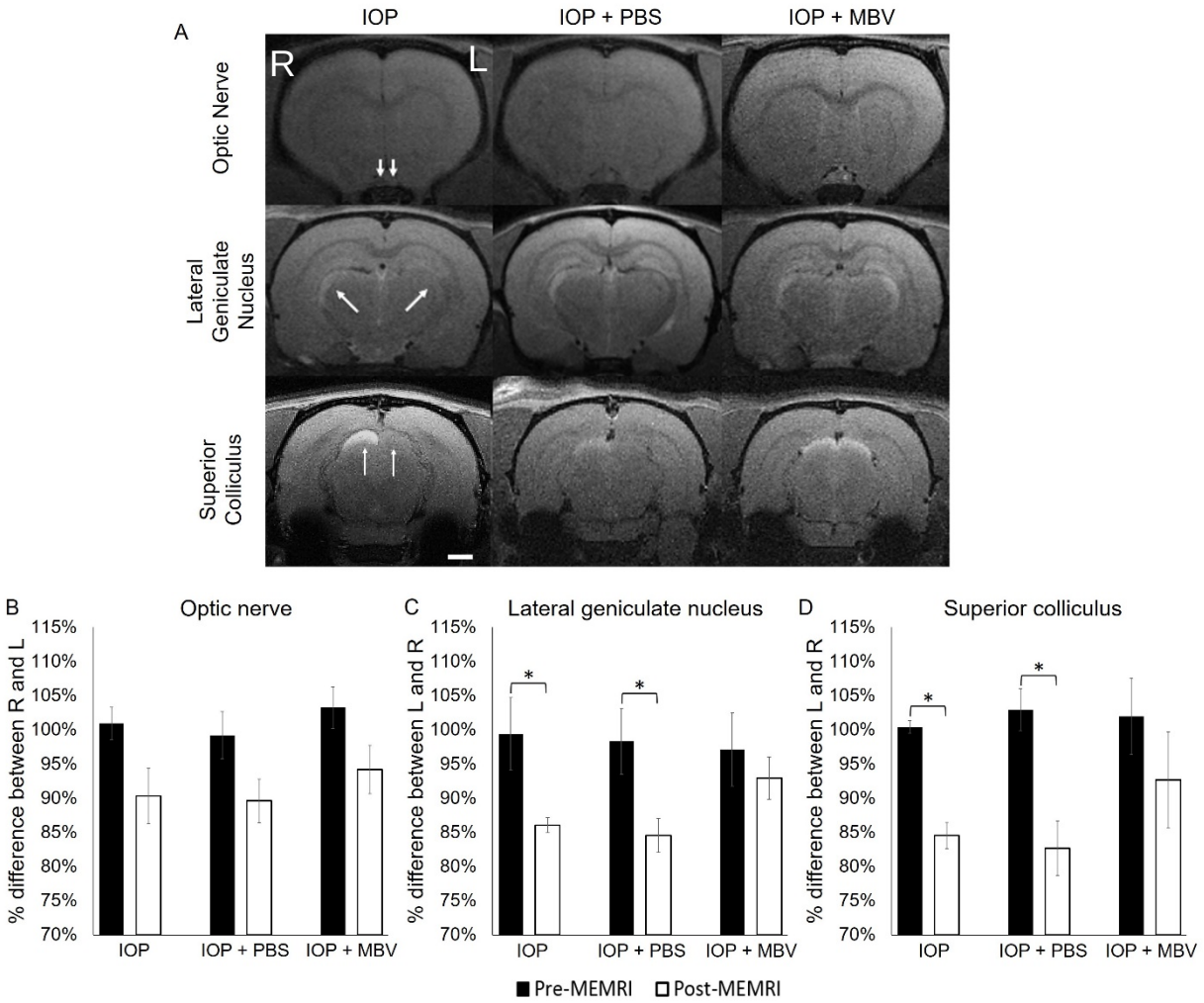

Figure 27. After IOP elevation, MBV increase anterograde Mn transport. A. Representative images of the optic nerve, lateral geniculate nucleus, and superior colliculus (SC) after IOP elevation, IOP elevation with PBS injection, and IOP elevation with MBV injections. Signal intensities were normalized to saline nearby saline phantom to account for system instability. Percent difference in manganese enhancement was calculated between right and left B. ON, C. LGN, and D. SC. Post-hoc Tukey's tests between pre- and post-MEMRI (*p<0.05). Data represented as mean ± SEM. Scale bar = 4mm

4.4 DISCUSSION

This study shows MBV derived from UBM-ECM can increase RGC neurite growth *in vitro,* decrease secretion of pro-inflammatory markers from microglia and astrocytes *in vitro,* and increase RGC survival after acute ocular injury. MBV are highly stable and protect biologically active signaling cargo, including miRNAs and proteins, from degradation. MBV survive even harsh ECM decellularization processes and thus likely play a fundamental role in tissue and organ organization across species and a regulatory role in the tissue response to injury. Recognition of their presence and an understanding of their biologic activity provides for possible new therapeutic approaches that are otherwise untenable. Derived from healthy, pro-regenerative tissues, MBV have biologic potential that exceeds that of extracellular vesicles derived from cultured cell lines. MBV carry unique (i.e. tissue specific) and complex cargo, including miRNAs, lipids, proteins, cytokines, carbohydrates, and other small molecules, capable of activating a variety of extra- and intracellular signaling pathways. Initial studies indicate that the cellular response to MBV depends on both surface proteins and the intra-luminal miRNA cargo [121]. Interestingly, miRNA cargo in MBV, derived from different tissues, are enriched in highly conserved miRNAs involved in cell cycle regulation and differentiation [121, 122], suggesting MBV play a fundamental role in ECM mediated tissue and organ development, organization, and function, possibly by regulating cellular phenotypes in a site appropriate manner. Small RNA sequencing (RNA-seq) identified known and novel candidate miRNA packaged within MBV [118] and results showed a differential miRNA signature dependent on the anatomical origin of the source tissue. Moreover, a cohort of miRNA known to regulate neuronal signaling pathways involved in neuronal differentiation and neurite growth, including miRNAs -30b, -125b, and -133b [123-125], were identified to be highly enriched in MBV.

MBV are non-neurotoxic *in vitro* at all concentrations tested, and significantly increased total neurite growth at 5, 10, and 20 µg/ml. While higher concentrations, i.e. 50 and 80 µg/ml, had no effect on RGC survival, these two concentrations did significantly stunt neurite growth compared to media controls, suggesting different components, including miRNA, regulating neuronal growth and survival are contained within MBV. The pathways MBV regulate to effect cell behavior are unknown. Extracellular vesicles are widely used as vehicles to shuttle proteins, lipids, carbohydrates, and nucleic acids between cells and organs that regulate cellular migration, proliferation, and organization [262, 263]. The discrepancy between regulation of neuronal survival and growth indicate different factors or cellular pathways, both extra- and intra-cellular, could be regulated by MBV.

MBV suppressed pro-inflammatory cytokine secretion from microglia and astrocytes. Depending on factors released into the microenvironment after injury, microglia and macrophages polarize to either the pro-inflammatory M1-like or anti-inflammatory M2-like phenotypes, which in turn dictates astrocyte phenotype [256]. The macrophage and microglia M2/M1 ratio is a key determinant whether tissue forms a scar or promotes functional tissue remodeling events following injury. Generally, M1-like cells are pro-inflammatory and produce high levels of oxidative metabolites that damage healthy cells and tissues [59], contributing to scar tissue formation. In contrast, M2-like cells are generally anti-inflammatory and regulate functional tissue remodeling [256]. In CNS tissues, M1-like macrophages and microglia are neurotoxic and possess only moderate axon growth-promoting effects [256], whereas M2-like macrophages and microglia are non-neurotoxic and can promote long-distance axon growth, even in the presence of growth inhibitory molecules like chondroitin sulfate proteoglycans (CSPG) or myelin [256].

MBV recapitulate effects of the parent ECM from which they are derived. Pro-inflammatory microglia and astrocytes are characterized by increased expression of IL-1β, IL-6, and TNF-α [264, 265], and MBV and UBM-ECM treatment following pro-inflammatory polarization of microglia decreased the release of IL-1β, IL-6, and TNF-α, suggesting MBV elicit a similar anti-inflammatory as UBM-ECM. Previous studies with bone marrow derived macrophages (BMDM) showed polarization with LPS/IFNγ to a pro-inflammatory phenotype is ameliorated by subsequent treatment with UBM-ECM or sub-intestinal submucosa (SIS-ECM) and leads to a gene expression profile distinct from transformed human mononuclear cell line (THP-1 cells) [266]. MBV were isolated from UBM-ECM and SIS-ECM, cultured with BMDM, and gene and protein expression evaluated [243]. While MBV derived from UBM-ECM and SIS-ECM elicited distinct changes in gene and protein expression, the MBV did recapitulate some effects from the parent ECM, thereby indicating MBV may be responsible, in part, for changes in cellular behavior elicited by ECM. The transition from pro-inflammatory, M2-like to anti-inflammatory, M1-like phenotype is an important regulator of the tissue healing response and returns the microenvironment to homeostasis after injury [194, 267] and failure to regulate the M2/M1 ratio results in chronic inflammation and impaired wound healing [268]. The downregulation of pro-inflammatory M1-like microglia polarization in the CNS also prevents the pro-inflammatory polarization of astrocytes to the A1-like pro-inflammatory phenotype that is associated with RGC cell death.

MBV decreased pro-inflammatory cytokine secretion from microglia and astrocytes. TNF-α is a pro-inflammatory protein known to stimulate A1-like astrocyte polarization [38], and since the secretion of TNF-α by LPS/IFNγ primed microglia was down regulated after MBV treatment, the pro-inflammatory cytokine secretion from astrocytes was subsequently prevented. IL-1β and

IL-6 expression, markers of pro-inflammatory astrocytes [264, 265], were also downregulated following MBV treatment, suggesting astrocytes were redirected from a pro-inflammatory phenotype and can therefore potentially avoid inducing RGC cell death. In the CNS, astrocytes participate in numerous functions essential to neuronal health [65, 66], metabolism [67, 68] survival, and signaling [69]. During development, astrocytes begin to form connections with neurons and other non-neuronal cells [70, 71]. In response to CNS injury or degeneration, astrocytes show a marked change in gene expression, hypertrophy and proliferation [72, 73], a process called reactive astrogliosis. Reactive astrogliosis can lead to several beneficial functions, including sequestration of damaged tissue and the buffering of excess cations and neurotransmitters [74-76]. However, these changes in astrocyte activity and gene expression also have negative consequences including exacerbation of tissue damage and glial scarring which inhibits axon regeneration [32]. These negative effects may be due to the over-production of reactive oxygen species and inflammatory cytokines as well as the release of extrinsic inhibitory factors [72, 77]. As shown in a previous study, factors released by pro-inflammatory astrocytes induce RGC cell death and immobilizing secreted factors TNF- α, IL-1 α, and C1q significantly increases RGC survival after [38]. The initial studies suggest the effect of MBV on microglia ameliorates the initial response in the CNS inflammatory chain which can rescue RGCs downstream.

After acute ocular injury, three intravitreal injections of MBV increased RGC survival and modulated the typical healing response in the CNS. RGCs typically degenerate after injury [269]. However, the MBV treatment caused significant survival of RGC compared to untreated control. Following elevated IOP, RGCs typically undergo cell death to a higher extent in the periphery than around the ONH [259, 270], and similar results were seen in this study where the RGCs in the

peripheral retina of untreated animals had the lowest survival rate. A similar trend was observed in the MBV treated animals where the RGCs in the peripheral retina had a lower survival rate than RGCs around the ONH. There are around 30 RGC subtypes that exist throughout the retina and are susceptible to stresses to different degrees [271]. While the mechanism through which MBV effect RGC survival is unclear at the moment, the data suggests that MBV have an effect on all RGC subtypes since RGC survival throughout the retina was increased. In addition to RGC cell bodies, RGC axon survival was increased in the retina and down the length of the optic nerve as shown by positive CtxB staining. RGCs typically take 3-5 weeks to regenerate from the retina to the optic chiasm [272, 273], therefore since axons were observed the length of the optic nerve, the results are indicative of RGC axon preservation rather than regeneration of newly formed axons, although future studies will examine earlier time points to verify this conclusion. After injury in the CNS, immune cells, including astrocytes, migrate to and proliferate in the injury site, thereby increasing GFAP expression [32] and ultimately leading to gliotic scarring. The MBV treatment significantly decreased GFAP positive staining in the optic nerve, suggesting decreased astrocyte activation which will ultimately lead to decreased scarring in acute injuries and a decrease in secreted neurotoxic factors associated with glial scarring [72, 77] and neuronal death [38]. MBV after injury increased GAP-43 expression along the optic nerve, indicating an increased potential to regenerate. However, as previously mentioned, since the entire length of the optic nerve showed positive CtxB staining at 14 days after injury, the results suggest MBV increase RGC axon survival and preservation and not necessarily regeneration. Future studies will include earlier time points to confirm these conclusions.

ERG and MEMRI results indicated MBV increased electrical function in the retina after injury and decreased Mn transport deficits in the visual system after injury. ERG used in this study

measured electrical function of neuronal and non-neuronal cells, therefore the results are not specific to RGC only. However, the RGC electrical activity is included in the measured response. MEMRI examines anterograde Mn transport between the retina and the visual pathway [163-165, 274, 275]. As previously shown in the results from chapter 2, acute IOP elevation has no effect on Mn transport in the optic nerve, but causes detectable changes in Mn transport in the LGN and SC, and similar results were observed in these animals. One caveat to note is that Long Evans rats were used in chapter 2, while Sprague-Dawley rats were used in this study. While the same trends held between the two studies, slight differences in the percentage Mn transport deficits could be attributed to differences in strains of rats used for the two studies. MBV treatment after IOP elevation resulted in decreased Mn transport deficits, indicating MBV treatment preserves anterograde axonal transport after injury. ERG and MEMRI results suggest MBV treatment may increase visual function after injury, and future studies will include visual behavior analysis.

This study shows MBV derived from UBM-ECM significantly increase RGC survival following injury and offer a minimally invasive therapeutic to treat ocular trauma. However, the mechanism through which MBV effect cellular behavior is unelucidated and outside the scope of the present study. Future studies will determine through which mechanism MBV enter cells, e.g. through internalization, fusion, or endocytosis, and which molecular pathways are being regulated in each cell type. Future studies will also determine at which time points and by which cell types MBV are internalized, both by uninjured and injured animals. *In vitro* results show MBV have a direct effect on RGC. However, the same conclusion cannot be drawn from *in vivo* studies at this time since MBV may be internalized by activated microglia, macrophages, or other circulating cells in the vitreous prior to being taken up by RGC following injury. Additionally, the optimal treatment window during which MBV need to be delivered will be determined. After injury,

immune cells infiltrate the site at various time points, therefore there exists a window during which MBV need to be delivered to avoid irreversible RGC and ocular morbidity. The current treatment regimen starts immediately after injury. However, this treatment regimen is not realistic in a clinical setting, therefore future studies will determine the time point after injury at which MBV need to be administered to serve as an effective treatment. The current study analyzed the cellular response 14 days after injury, and future studies will include analysis of the cellular survival and immune response at additional time points, e.g. 1, 3, and 7 days, and 1, 3, and 6 months, to gather a comprehensive understanding of the temporal effects of MBV after injury.

MBV can easily be engineered to contain specific cargoes or combined with existing technologies to offer combinatorial devices. In addition to naturally containing bioactive factors that can positively regulate ocular tissue remodeling, MBV can be engineered to contain specific proteins, small molecules, and nucleic acids to further optimize constructive remodeling of injured ocular, and other, tissues [263]. MBV withstand harsh decellularization processes using mechanical agitation, detergents, and lyophilization, thereby making them rigid and robust delivery vehicles. The robust nature and small size of these vesicles make them good candidates to be incorporated into existing devices used for CNS and ocular repair after injury [219] to work in concert with and enhance the efficacy of existing devices.

CNS injuries typically lead to a destructive pro-inflammatory response which prevents functional recovery of damaged CNS tissue. This study shows that MBV derived from UBM-ECM suppress secretion of pro-inflammatory cytokines and increase RGC survival after injury. MBV are derived from FDA approved, commercially available products, therefore hold minimal risk of adverse response in pre-clinical and clinical trials. MBV are a versatile therapeutic that can be delivered in a minimally invasive manner, can be engineered to incorporate additional biologic

factors, and can be incorporated into and combined with existing devices to act in concert with other commercially available and experimental therapeutics. MBV thus offer a significant vertical advance for ocular and CNS functional remodeling.

5.0 DISSERTATION SYNOPSIS

5.1 MAJOR FINDINGS

The present work described the effects of elevated IOP on the visual system and the development of ECM bioscaffolds and MBV for ocular therapeutics. In the first section of work, the structural and functional changes in visual pathway integrity and function were described as a function of IOP elevation severity. The LGN was implicated in structural and functional changes, suggesting this region in the visual pathway is highly susceptible to damage following injury. Fetal brain tissue was decellularized using a vacuum assisted decellularization chamber to effectively remove cellular content from delicate fetal tissue. *In vitro,* fB-ECM was non-neurotoxic and increased neurite outgrowth, suggesting the fB-ECM would be suitable for *in vivo* applications. However, following optic nerve crush experiments, the fB-ECM hydrogels decreased astrocyte pro-inflammatory activation and increased axonal growth marker expression in some animals, but this was not seen in all animals. The variability seen in animals is hypothesized to be due to the necessity to fenestrate the optic nerve sheath after optic nerve crush and prior to treatment, therefore indicating that while fB-ECM is a promising treatment for CNS injuries, it may not be an optimal delivery platform in the visual system. MBV were isolated from UBM-ECM and *in vitro* experiments indicated MBV have strong anti-inflammatory properties and induce neurite outgrowth. *In vivo* studies show intravitreal delivery of MBV decrease as pro-inflammatory astrocyte polarization and increase RGC survival and function after IOP elevation. MBV offer a vertical advance in the field of regenerative medicine and offers the ability to treat ocular and other CNS injuries in a minimally invasive manner.

5.2 FUTURE WORK

This dissertation reports on multi-parametric neuroimaging of axon degeneration and the development of extracellular matrix (ECM) and matrix bound nanovesicles (MBV) therapeutics and their effects on the visual system after ocular injury. White matter integrity, active axonal transport, and functional connectivity were decreased following acute and chronic intraocular pressure (IOP) elevation, and these effects were ameliorated in the animals that received oral citicoline treatment prior to and after injury. ECM bioscaffolds have been used in many tissues and organs to increase functional remodeling after injury, and this dissertation reports on the derivation of fetal brain ECM (fB-ECM) and its application *in vitro* and *in vivo. In vitro* results using fB-ECM were promising, but *in vivo* studies showed variable results, indicating fB-ECM has the ability to promote functional remodeling but may not be the optimal solution to treat ocular injuries. The final section of work analyzed MBV derived from urinary bladder matrix (UBM) and their application *in vitro* and *in vivo* after ocular injury. MBV increase retinal ganglion cell (RGC) neurite growth and decreased pro-inflammatory cytokine secretion *in vitro.* Following ocular injury, MBV increased RGC survival, decreased astrocyte activation, increased electrical activity in the retina, and decreased axonal transport deficits. Although, these results indicate axonal degeneration and neuroprotection can be detected using MRI, and MBV may offer an easily administered therapeutic to preserve vision after injury, future work can expand on the findings included in this dissertation to further understand mechanisms of injury and refine MBV to be used as a clinical therapy.

MRI results included in the second chapter of this dissertation indicate oral citicoline can decrease neurodegeneration after chronic IOP elevation. Animals were treated daily 7 days prior to injury and every 48 hours for 14 days after injury which proved to be effective in decreasing

neurodegeneration. However, only one treatment paradigm was used and therefore may not be the optimal dosage or frequency. Future work will investigate different doses of citicoline with treatment starting at earlier time points as well as concurrently with IOP elevation to determine the treatment window during which citicoline treatment needs to be administered to be effective. While such results are promising, there is still much more to be learned about both citicoline, such as in treatment later in the disease course, and other possible neuroprotective agents. Since brain regions other than the eyes are affected, treatment mechanisms should focus on treating neural structures throughout the visual and nervous system. Chemical exchange saturation transfer (CEST) MRI has been used to track citicoline *in vivo,* and this technique can be used in future studies to investigate citicoline action and delivery in the visual system in experimental glaucoma. The study showed MRI can be used to detect neurodegeneration and neuroprotection, therefore the modalities can be used to assess efficacy of experimental glaucoma therapies.

MBV are bioactive, can regulate cellular processes, and can be administered in a minimally invasive manner. Extracellular microvesicles (EVs) are increasingly appreciated as important factors regulating intercellular communication in the visual system and are now being explored as biomarkers, therapeutics, and drug delivery vehicles. EVs are released by all cell types and comprise a several populations of sub-micron sized vesicles, including exosomes, ectosomes, oncosomes, shed vesicles or microvesicles, apoptotic bodies, and recently described matrix bound nanovesicles. Though the EV nomenclature is developing, EVs are generally classified by their origin and molecular profile into four main groups: exosomes, microvesicles, apoptotic bodies [276], and the recently described matrix bound nanovesicles [118]. The work included in this dissertation indicates ECM and MBV have the potential to modulate the immune response and promote functional remodeling in the visual system after injury. Aim 3 showed promising results

that indicate MBV derived from UBM-ECM have the potential to prevent RGC death after injury. However, UBM-ECM may not be the ideal source of MBV for ocular applications. Previous studies have shown there are negligible differences between ECM derived from different source tissues when analyzing effects on neurite outgrowth [221]. However, similar comparative studies have not been done using MBV derived from different tissue sources, and previous studies showed MBV derived from different source tissues contain different miRNA cargoes [118]. Therefore, future work should investigate the differences between MBV derived from different source tissue, e.g. dermal ECM, sub-intestinal submucosa, or CNS specific, as it pertains to neuronal cells to determine which tissue source will induce the greatest extent of RGC cell and axon survival after injury.

Chapter 4 indicated MBV increase RGC survival after ocular injury. However, no mechanisms have been identified to explain how MBV enter cells of elicit the responses observed in these studies. Future studies will determine through which mechanism MBV enter cells, e.g. through internalization, fusion, or endocytosis, and which molecular pathways are being regulated in each cell type affected by MBV. Two potential mechanisms that have been hypothesized to explain how MBV regulate cellular behavior include miRNA cargoes and IL-33. UBM MBV have previously been shown to contain miRNAs involved in cellular development, growth, and viability. Five specific miRNA were identified, including miRNA-29b, -30b, -34a, -125b, and -133b [118]. MiRNA-29b has been implicated in inhibiting apoptosis [277]. miRNA-30b and miRNA-125b have been shown to inhibit apoptosis and promote neuronal growth. miRNA-133b has been shown to promote neurite growth [124, 125, 278] and increase branch number [123, 279]. Conversely, miRNA-34a has been implicated in promoting apoptosis and decreasing neuronal growth [280]. Since miRNA are highly conserved, these miRNA contained in MBV from porcine

derived ECM can promote beneficial effects on cells from other species and can potentially explain the effects of MBV on RGC observed in Aim 3. Recently, MBV have been shown to be upregulated in IL-33. IL-33 has been shown to be downregulated after CNS injury, and the imbalance is associated with an imbalance in Th1/Th2 ratio which exarcerbates secondary injury [281]. Administration of recombinant IL-33 after CNS injury in mice has been shown to ameliorate the severity of CNS injury and improve functional recovery [282]. Future work will be focused on determining whether IL-33 is a key player in the immunomodulatory effect elicited by MBV.

In aim 3, MBV were adminstered immediately after injury, and at days 2 and 7. This initial paradigm was chosen to first identify whether MBV are effective when adinsitered at an optimal time after injury. However, this is not a realistic or translatable method of adminstration. Patients often report to emergency rooms hours to days after injury and based on the nature of other potentially life-threatening injuries, ocular injuries are often not immediately addressed. Future work needs to determine the treatment window after injury during which the first MBV dose needs to be administered, and whether repeated injections are necessary.

Although MBV increased RGC survival, the optimal combination of factors necessary to ameliorate damage after CNS injury and promote neuronal survival are yet to be determined. MBV are tunable and in addition to naturally containing bioactive factors that can positively regulate ocular tissue remodeling, MBV can be engineered to contain specific proteins, small molecules, and nucleic acids to further optimize constructive remodeling of injured ocular, and other, tissues [263], thereby making them ideal delivery vehicles to administer their own and loaded cargoes. Vesicles, or combinations of vesicles, can target and deliver diverse biomolecular cargoes to modulate distinct cellular populations, like immune cells, glia, and neurons, making them attractive developing combinatorial therapeutics to treat CNS and ocular injuries and diseases

clinically. Though clinical studies are in early development phases, this idea is supported by pre-clinical rodent studies reporting positive tissue remodeling and increased functional recovery in a stroke model [283]. In addition to being tunable, MBV are good candidates to be loaded into existing devices used for ocular and CNS repair to enhance efficacy of the devices [219]. MBV withstand harsh decellularization processes using mechanical agitation, detergents, and lyophilization, thereby making them rigid and robust entities that can be incorporated into existing devices through multiple manufacturing methods. For example, Appendix A describes a study fabricating a synthetic polymer loaded with an anti-inflammatory agent, tacrolimus, that decreases the pro-inflammatory response in the optic nerve after injury. Although outside of the scope of this dissertation, future studies can investigate incorporating MBV and tacrolimus into a one device aimed at promoting functional tissue remodeling after injury. Since MBV are tunable and robust, the vesicles can either be loaded with tacrolimus or incorporate into the synthetic polymer.

MBV are a natural component of the ECM in healthy tissues, have been shown to be non-cytotoxic, can promote CNS neurite growth, promote an anti-inflammatory macrophage and microglia phenotype, and can easily be administered *in vivo*, therefore making MBV an attractive option to promote neuroprotection and constructive remodeling in the CNS after injury.

5.3 OVERALL CONCLUSIONS

The work in this dissertation describes longitudinal MRI on the visual system after injury, and the development and effects of fetal derived ECM and MBV *in vitro* and *in vivo* after injury in rodent models. The decellularization process effectively decellularized delicate fetal tissue

which formed an injectable hydrogel capable of mitigating inflammatory responses and increasing neuronal growth. MBV were isolated from ECM bioscaffolds and successfully decreased the inflammatory response and increased RGC survival and retinal function after injury. MBV can be combined with other neurotrophic factors and bioactive components to deliver combinatorial approaches therapies. The work presented here offers an exciting opportunity to treat ocular and CNS injuries through a minimally invasive therapeutic.

APPENDIX A

A POLYMERIC TACROLIMUS-ELUTING NERVE WRAP MODULATES LOCAL TISSUE REMODELING AFTER EXPERIMENTAL ACUTE OPTIC NERVE ISCHEMIA

INTRODUCTION

In adult mammals, central nervous system (CNS) injury remains a persistent experimental and clinical challenge. Trauma to CNS tissues triggers a pro-inflammatory innate immune response that leads to secondary tissue damage, injury site expansion, and cellular and extracellular matrix (ECM) remodeling [31]. This default healing response contributes to failed axon regeneration [30, 284] and promotes scar tissue formation [32], often leading to irreversible CNS neuron death [285] and permanently lost neurological function. Thus, combinatorial approaches are needed that can positively modulate the innate immune response to promote functional tissue remodeling over scarring while also providing key neuroprotective and neuroregenerative support to CNS neurons.

Tacrolimus, also called FK506, is a macrolide immunosuppressive drug initially derived from *Streptomyces tsukubaensis* (Prograf ® Astellas, NJ) [286] used clinically to prevent organ transplant rejection [287] as well as to treat various dermatologic [288] and autoimmune diseases [289]. Tacrolimus binds to FK506-binding protein (FKBP) receptors of the immunophilin family, which comprises at least 15 members in humans. In humans, tacrolimus is thought to prevent organ transplant rejection by suppressing T-cell activation via binding to FKBP12 [290]. In the CNS,

FKBPs are widely expressed by numerous cell types, including both neurons and glia, with different cellular populations exhibiting distinct FKBP subtype expression patterns and pharmacokinetics. In the CNS, tacrolimus is hypothesized to modulate the innate immune response by reducing neutrophil and macrophage infiltration and microglial [291] and astrocyte activation [292-294], subsequently reducing oxidative stress, secondary damage, and injury site expansion [295].

Experimentally, tacrolimus can also provide both neuroprotective and neuroregenerative benefits to CNS neurons. Although FKBPs are widely expressed by CNS neurons, tacrolimus appears to modulate neuronal activities by multiple mechanisms, including by FKBP-dependent and -independent routes [296]. After optic nerve (ON) ischemia in rats, tacrolimus increases retinal ganglion cell (RGC) survival by suppressing apoptotic signaling [297]. After spinal cord injury in rats, tacrolimus increases axon growth and the expression of *growth associated protein-43 (GAP43),* an axon growth marker [298, 299] and can improve functional recovery [300]. In recent studies, tacrolimus has been shown to reduce ischemia reperfusion injury in white matter after cerebral artery occlusion surgery [295] and decrease apoptosis in hippocampal neurons [301]. However, most experimental studies have relied on systemic administration to deliver tacrolimus to CNS tissues [295, 301]. Tacrolimus is highly lipophilic and thus accumulates in fatty tissues throughout the body, including the myelin-based white matter in the CNS. However, systemic delivery to CNS tissues is complicated by preferential uptake by other organs, which requires higher systemic doses to effectively increase tacrolimus in CNS tissues. These increases in systemic tacrolimus often lead to often life-threatening toxicity in other tissues and organs.

Clinically, tacrolimus is administered systemically either orally or by injection [302, 303]. The chemical properties of tacrolimus require careful consideration with regard to systemic

administration. The method of administration, frequency, and dosage, must be carefully to maintain effective therapeutic tissue levels without inducing toxicity is off-target tissues. Improperly regulated systemic levels can lead to several life-threatening side effects, including but not limited to diabetogenicity, nephrotoxicity, neurotoxicity and oncogenicity [287, 304]. Moreover, tacrolimus administration is further complicated by tacrolimus the number of distribution of FKBP binding proteins. Tacrolimus acts on at least 15 FKBP binding receptors in humans differentially expressed by cellular populations in different tissues and organs. Therefore, tacrolimus administration must be carefully optimized to maintain effective concentrations within the tissues of interest to maximize efficacy while minimizing toxic side-effects both to targeted and to non-targeted cellular populations and tissues. Thus, strategies being developed to deliver tacrolimus locally. Local delivery approaches include hydrogels [305], inhalants [306], and micelle [307] or polymer encapsulation technologies [308]. However, these technologies are limited for many CNS applications due to ineffective and/or inconsistent tacrolimus delivery to specific CNS tissues, incompatible mechanical properties, and the inability to remain intact and/or localized to the injury site.

To deliver tacrolimus locally and controllably to CNS tissues, this study developed a biodegradable and elastic matrix using poly(ester urethane) urea (PEUU) [309]. PEUU polymers have desirable mechanical characteristics, including high elasticity and strength, good cell-adhesive properties, and controllable biodegradation, all of which can be tuned to match the tissue of interest. By modifying a previously developed PEUU electrospinning platform [310], tacrolimus and PEUU were successfully blended into PEUU polymer matrices. This method allowed precise control over both the PEUU and tacrolimus concentrations as well as control over the size and the thickness of the PEUU-Tac matrices. PEUU-Tac material properties and release

kinetics were analyzed *in vitro*. The dose-dependent effects of tacrolimus on primary RGC viability, toxicity, and differentiation were analyzed *in vitro*. Finally, PEUU-Tac matrices were used as ON wraps to analyze local, trans-dural tacrolimus delivery to CNS tissues and to the blood in an acute ON ischemia model in rat.

MATERIALS AND METHODS

Animals

Sprague-Dawley rats were purchased from Charles River Laboratories (Wilmington, MA). Animals were housed and maintained according to the guidelines set forth by the University of Pittsburgh Institutional Animal Care and Use Committee (IACUC) and the DOD Animal Care and Use Review Office (ACURO). All procedures complied with the American Association for the Accreditation of Laboratory Animal Care (AALAC).

Retinal ganglion cells

Primary RGCs were isolated from female and male postnatal day three (P3) Sprague-Dawley rat pups, purified by immunopanning, and cultured in NB-SATO media as described [215]. RGCs were seeded ($5 \times 10^3/cm^2$) on cell culture plates coated with poly-D-lysine (70 kDa, 10 μg/mL; Sigma-Aldrich Corp., St. Louis, MO, USA) and laminin (2 μg/mL, Sigma-Aldrich Corp.). Tacrolimus (Invitrogen) was diluted in 100% EtOH to make a 20 mM stock. The tacrolimus stock

was then diluted in NB-SATO as specified and the RGC cultures maintained at 37°C in 10% CO_2 for 3 days *in vitro* (DIV).

RGC viability

Viability was analyzed after 3 DIV using a calcein and propidium iodide based live/dead kit per manufacturer's instructions (Life Technologies, R37601). For analysis, the first five non-overlapping fields of view per well, moving from the left well edge, were imaged at 20X using standard epi-fluorescence fluorescein and rhodamine filter sets (Zeiss, Axio Observer). Experimentally blinded individuals analyzed live and dead cells using ImageJ (National Institutes of Health, Bethesda, MD, USA). Data represent triplicates from four experimental repeats, totaling at least 27 fields of view and at least 300 neurons per group as previously described [121]. Significance between groups was determined by one-way analysis of variance (ANOVA) as noted in section 2.13.

RGC neurite growth

After 3 DIV, RGCs were fixed with 4% paraformaldehyde (Alfa Aesar; 30525-89-4) in PBS, washed with PBS (2X), and permeabilized with 0.2% triton X-100 in PBS for 15 min. After blocking for 1 hr (1% BSA in PBS, Fisher Scientific), the RGCs were incubated with anti-β III tubulin (1:300, TUJ-1, Millipore, RRID: AB 570918) at 4°C overnight, washed in PBS (3X), incubated with a FITC-rabbit anti-chicken IgY H+L secondary (1:150, #31501, Thermo Scientific) for 3 hrs, washed with PBS (3X), counterstained with the nuclear marker DAPI (1:3000, Invitrogen, D1306) for 20 min at room temperature, and washed in PBS (2X, 5 min each). The

RGCs were imaged randomly as described above and neurite growth measured by blinded individuals as described [311] using the ImageJ plugin, NeuronJ (National Institutes of Health, Bethesda, MD, USA). The first ten non-contacting RGCs encountered, moving right from the left edge of the well, were analyzed from triplicate wells in each of three independent experimental repeats, totaling at least 90 neurons per condition. Significance between groups was determined by ANOVA as noted in section 2.13.

PEUU-Tac

Poly(ester urethane) urea (PEUU) was synthesized from polycaprolactone diol (Mn = 2000), 1,4-diisocyanatobutane and putrescine, as described [309] and PEUU-Tac matrices fabricated by electrospinning as described [312]. Briefly, 10 mg or 20 mg of tacrolimus was dissolved in 500 μL of 1,1,1,3,3,3-hexafluoroisopropanol (HFIP). Each tacrolimus solution was mixed with 0.45 g PEUU (12% w/v in HFIP) and electrospun onto a rotating stainless-steel mandrel (19 mm diameter) by feeding through a charged capillary at a rate of 3 mL/hr. The mandrel was located 17 cm from the tip of the capillary and the voltage between the capillary and the mandrel was 19 kV. PEUU-Tac matrices were sterilized under UV light overnight and then with ethylene oxide (ETO) before use.

PEUU-Tac release kinetics

To determine tacrolimus release rate, PEUU-Tac matrices were cut into three equal weight sections (15 mg) and each section was placed in 25 mL of 0.5% Cremephor EL (C5135, Sigma, St. Louis, MO) in PBS (CrEL-PBS) [313] in Sigmacote (SL2, Sigma, St. Louis, MO) treated 50 mL glass

beakers with gentle agitation (60 RPM, Thermo Labline 2314 Orbital Shaker). At the indicated time points ranging from 1 hr to 14 days, 300 µl was removed for analysis and then replaced with 300 µl of fresh CrEL-PBS. For each sample, 50 µl was mixed with 450 µl of blood and analyzed by UPLC-tandem mass spectrometry as described below. Three additional 50 mL glass beakers were coated with Sigmacote. One PEUU-Tac section was placed in each beaker with 25mL CrEL-PBS with gentle agitation (60 RPM, Thermo Labline 2314 Orbital Shaker) for 24 hrs. The three PEUU-Tac sections were removed from the CrEL-PBS solution and each placed in 5 mL of HFIP with gentle agitation for 5 minutes to dissolve the PEUU scaffold. Three fresh PEUU-Tac sections of equal weight to the pre-release scaffold weight were also placed in 5mL HFIP. The tacrolimus concentration was then measured for each sample by HPLC. Significance between groups was determined by ANOVA as noted in section 2.13.

PEUU and PEUU-Tac degradation

The degradation rate of PEUU-Tac was analyzed at 37°C in PBS as described [314]. Briefly, equal size samples (10 × 5 × 0.1 mm) were cut from an unloaded PEUU matrix, 10 mg tacrolimus loaded, or 20 mg tacrolimus loaded PEUU-Tac and placed in 15 mL of PBS in a 20 mL vial. At each time point, the samples were removed from the buffer, washed with deionized water, and dried under vacuum at room temperature for 3 to 4 days before weighing to determine the mass lost, using the equation:

$$\text{Mass Remaining (\%)} = \left(\frac{m_d}{m_{orig}} \right) \cdot 100$$

where m_d is the sample after drying and m_{orig} is the original mass. After weighing, each sample was placed in fresh PBS. The time in PBS indicates the total time in PBS, independent of

the drying time. For visualization, the PEUU matrices were sputter-coated with gold/palladium and imaged using standard scanning electron microscopy methods (SEM; JSM-6330F, JEOL USA). Data represent triplicates from three experimental repeats. The average mass is reported with the error bars indicating one standard deviation. Significance between groups was determined by ANOVA as noted in section 2.13

PEUU-Tac mechanical properties

To test the mechanical properties of PEUU or PEUU-Tac, each matrix was cut into a dumbbell geometry (ASTM D1708) using a custom-made dog-bone cutting die with a 2.5 mm width, a 10 mm gauge length, and a total length of 20 mm. PEUU tensile properties were analyzed by uniaxial tensile testing using an MTS Insight (MTS Systems Corporation, MN, USA) with a 10 N (0.01 N resolution) load cell at room temperature. The samples were extensionally deformed at 10 mm/min, according to ASTM D638M. Young's modulus was calculated by finding the initial slope of the stress versus strain curve ($0<\varepsilon<10\%$) using linear regression. The ultimate stress was determined as the maximum stress and the strain-at-break recorded as the strain at the point where the force became zero. The averages and error bars, indicating one standard deviation, are reported. Data represent triplicates from three experimental repeats. Significance between groups was determined by ANOVA as noted in section 2.13.

ON ischemia and PEUU-Tac

Animals were anesthetized by injecting a 45:10 mg/kg ketamine/xylazine cocktail intraperitoneally. The ON was exposed by making a small incision in the conjunctiva and then

blunt dissecting a nearly bloodless plane back to the ON using #5 jeweler forceps. The muscle and connective tissues around the ON were gently separated to expose the ON sheath. Using a Yasargil aneurysm clip (Aesculap FT252T), the right ON was clamped approx. 2 mm behind the globe for 10 seconds [315]. After clamping, the ophthalmic artery was visualized to confirm integrity. A subset of animals (n=5) had the ON sheath fenestrated at the clamp site by making a 1-2 mm incision using an ultra-sharp scalpel (#681.01, Oasis Medical). For animals receiving PEUU-Tac, a 2 x 5 mm section of 10 mg PEUU-Tac was wrapped around the injury site and sutured to itself and to the sheath. The conjunctiva was then sutured closed and antibiotic ointment (NDC 24208-780-55, Gentamicin, Bausch & Lomb, Tampa, Florida) applied to the eye. In total, forty-six animals were used. The experimental groups included: 1. Injured. Nine animals received only ischemia to the right ON. 2. Injured, PEUU-Tac. After ischemia to the right ON of 14 animals, a 2 mm x 5 mm section of 10 mg PEUU-Tac was sutured around the injury site (no fenestration). 3. Injured, PEUU-Tac (fenestrated). After ischemia to the right ON of five animals, the ON sheath was fenestrated as described above before a 2 mm x 5 mm section of 10 mg PEUU-Tac was sutured around the injury site. 4. Systemic. After ischemia to the right ON, nine animals were injected intraperitoneally with tacrolimus (2.2 mg/kg/day) for 14 days with the first injection administered immediately after surgery. 5. Nine animals served as sham surgery controls. Five animals per group were used for tacrolimus tissue levels analysis and four were used for immunohistochemistry. The injured, PEUU-Tac group had five additional animals that were used for Tac tissue level analysis at 24 hrs. Power analysis was used to determine sample size. The number of experimental animals was determined using G*power software (G*power software 3.1.9.2, Germany). We calculated the effect size to be 0.6 according to our previous experiments. Power analysis for ANOVA dictates n=4 animals for histological analysis and n=5 animals for

tacrolimus tissue levels per group for *in vivo* studies to achieve 80% power for $\alpha = 0.05$. Animals were randomly assigned to groups by an experimentally blinded animal technician.

Tacrolimus blood tissue analysis

Twenty-four hours after surgery, 500 µl of blood was drawn via the tail vein. Additionally, at 24 hours, four PEUU-Tac treated animals were sacrificed and the ONs and retinas collected. At 14 days, the remaining thirty-six animals were sacrificed, and blood, retinas, and ONs collected. Tacrolimus tissue levels were analyzed from five animals per group and the remaining four animals per group were used for immunohistochemistry. The blood was collected in BD Microtainer blood collection tubes (Becton Dickinson, 363706) pre-coated with EDTA to avoid coagulation, and stored at 4ºC until analysis. Retinas and ONs were weighed, homogenized in 100% methanol (MeOH) using a Mini-BeadBeater-1 sonicator (Mini-BeadBeater-16, Thomas Scientific), and left overnight to ensure complete tacrolimus extraction. The homogenate was centrifuged at 2100 ± 100 rpm for 10 min, the methanol transferred to a microcentrifuge tube, and evaporated completely using a vacufuge (Eppendorf Vacufuge Plus 5305 Concentrator Vacuum). The residue was then reconstituted in 1 mL of naïve rat blood prior to quantification as described below.

Tacrolimus quantification by UPLC-tandem mass spectrometry

Tacrolimus was analyzed by UPLC (Nova-pack® C18 column, 2.1 x 10 mm cartridge (Waters # 186003523)) as described [316, 317]. Briefly, standard curves and quality control blood samples were prepared using dry tacrolimus (tlrl-fk5, Invivogen). For each sample, 50 µL blood was added

to a conical centrifugation tube, followed by 200 µL zinc sulfate heptahydrate ($ZnSO4 \cdot 7H2O$) to precipitate the blood proteins, and 500 µL ascomycin (20 ng/l in acetonitrile) as an internal standard. The samples were vortexed for 2 mins at 3,000 RPM, centrifuged for 3 mins at 13,000 RPM, and the supernatants collected in LCMS vials (60180-508, Thermo Scientific). Analysis was done using a fully validated, reverse phase ultra high-performance liquid chromatographic method for detecting tacrolimus in blood with an injection volume of 10 µL. Analytes were separated using a gradient elution consisting of an aqueous mobile phase (95% $H2O$ / 5% MeOH) and an organic mobile phase (100% MeOH), at a flow rate of 0.6 mL per min. To optimize ionization and enhance the chromatographic output quality, both mobile phases contained 0.1% formic acid (CH_2O_2) and 2 mM ammonium acetate. Both intra- and inter-day precision were shown to be acceptable (C.V. <10%, n=3) at concentrations of 4.3, 15.7, and 24.6 ng/mL. Results are expressed as tacrolimus in ng/g of tissue or ng/mL of blood. For animal blood and tissue tacrolimus levels, data represent triplicates from at least five animals per condition analyzed by ANOVA as noted in section 2.13.

Immunohistochemistry

For immunohistochemistry, tissues were fixed in 4% paraformaldehyde for 4 hrs, cryoprotected in 30% sucrose for 4 hrs, embedded in optical cutting temperature (OCT) medium (Tissue-Tek; Miles Inc, Elkhart, IN) and stored at 4°C overnight before freezing in liquid nitrogen. Embedded tissues were stored at -80°C prior to cryostat sectioning (15 µm thickness). ON sections were permeabilized with 0.2% triton X-100 in PBS for 15 mins, washed in PBS (2X), blocked for 1 hr (1% BSA in PBS, BP9706100, Fisher Scientific), and washed in PBS (2X). ON sections were labeled with anti-glial fibrillary acidic protein antibody (Anti-GFAP, 1:500, Abcam, AB7260, RRID:AB_296804) or anti-growth associated protein 43 (Anti-GAP-43, 1:500, Abcam, AB16053,

RRID:AB_598153), and DAPI (1:2000, Thermo Scientific, 62247). The sections were imaged and pixel intensities measured by experimentally blinded individuals using ImageJ as described [218]. Briefly, fifteen ROIs of 100 x 100 pixels were drawn around the crush site *(GFAP)* and distal to the crush site (*GAP-43*). Four ROIs were drawn on the image background. The area, mean fluorescence, and integrated density for each image were analyzed using the following formula: CTCF = integrated density – (area x mean background fluorescence). Data represent triplicates from three experimental repeats analyzed by ANOVA as noted in section 5.2.13.

Statistical analysis.

All analyses were done by experimentally blinded individuals. To determine significance between groups ($p < 0.05$), ANOVA was used in conjunction with a Tukey's post-hoc test using SPSS Statistical Analysis Software (IBM, Chicago, IL, USA). All error bars represent standard error of the mean (SEM) unless noted otherwise.

RESULTS

Tacrolimus regulates RGC viability bi-modally

Previous studies indicate tacrolimus has both neuroprotective and neuroregenerative effects on CNS neurons, including RGCs *in vitro* [318] and *in vivo* [297]. However, the effective concentration ranges on RGC viability and growth have not been reported for primary RGCs in culture. To determine the dose-dependent effects of tacrolimus on RGC toxicity, RGCs were

cultured in tacrolimus concentrations, ranging from 0.1 to 100 μM (Figure 28b). Below 0.1 μM, RGC viability was unchanged. At 0.1 μM, RGC viability was 66%, or 94% of the vehicle control, which is in the typical range for primary RGCs cultured *in vitro*. Over 0.1 μM, RGC viability initially increased to a maximum of 91% viable, 21% greater than control, at 0.5 μM, before decreasing dose-dependently to 0% at 75 μM. Lethal dose (LD) response analysis was conducted by plotting the data points on a semi-logarithmic graph and then using non-linear regression to generate a dose response curve, which indicated an LD_{50}=24.2 μM (Figure 28c).

Effect of tacrolimus on RGC axon growth

To determine tacrolimus effects on RGC neurite growth, RGCs were initially cultured at high density and total neurite growth, which included both axons and dendrites, was analyzed (Figure 29b). The average total neurite growth per neuronal cell body was greatest at 5 nM but neurite growth did not follow a typical dose-response relationship. From 10 nM to 5 μM total neurite growth remained largely unchanged before decreasing coordinately with viability to 0 at 75 μM.

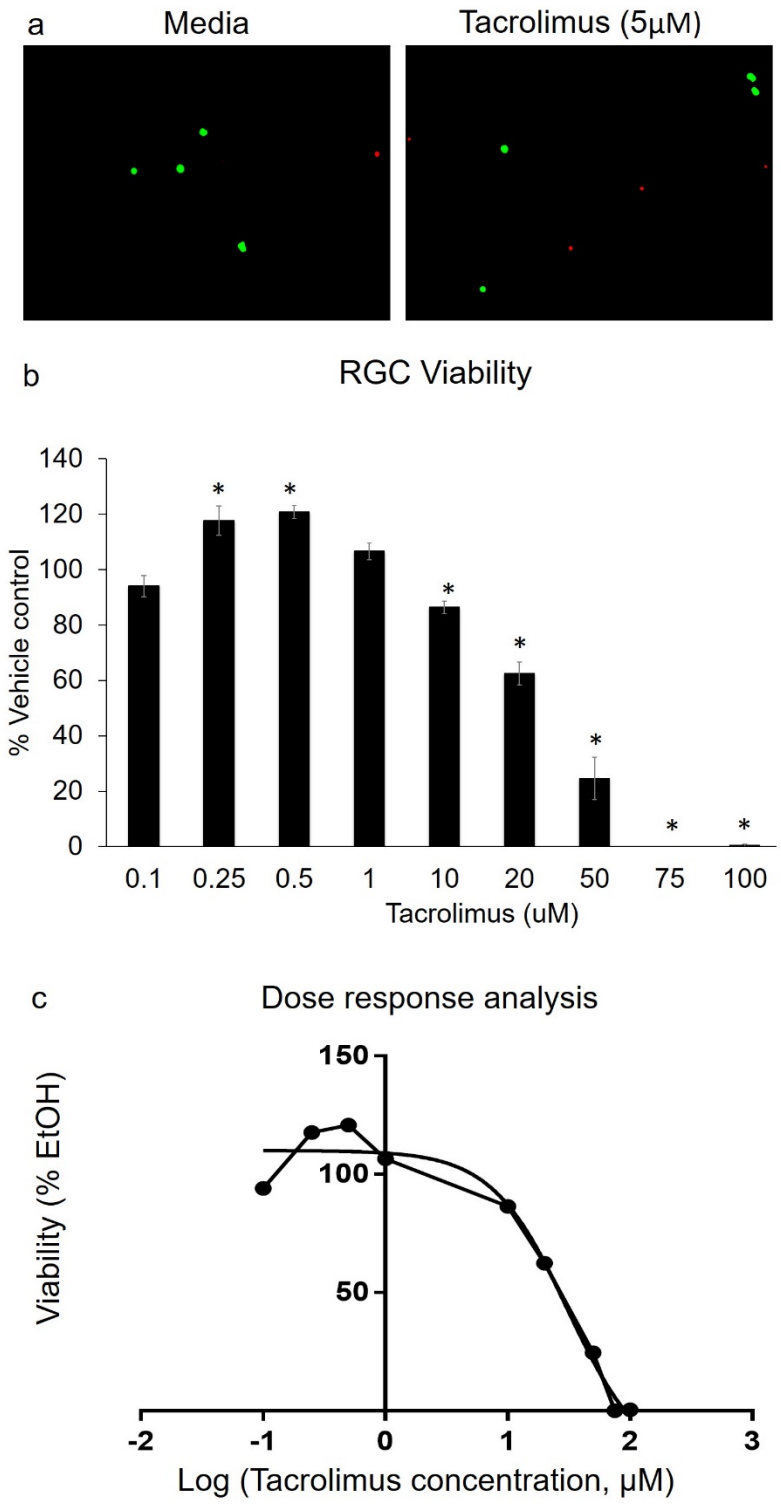

Figure 28. Tacrolimus regulates RGC viability bi-modally in a concentration dependent manner

Thus, although 5 nM stimulated growth to the greatest extent, tacrolimus appears to support RGC neurite growth over a broad concentration range up to 5 μM *in vitro*.

In high-density cultures, the specific effects of tacrolimus on neurite growth, i.e. dendrite vs. axon growth or branching, is masked by neurite to neurite contact and fasciculation [319]. Therefore, we analyzed the effects of 5 μM tacrolimus on total neurite growth, axon growth, and branching in non-contacting neurons, cultured in low-density cultures (Figure 29c-e). In contrast to high-density cultures, tacrolimus increased total neurite growth by 60% and axon growth by 70% (Figure 29b), whereas branching frequency was unchanged (Figure 29c). Thus, the majority, 85%, of the total increase in neurite growth by tacrolimus is due to increased axon growth. These data provide a basis for identifying the receptors and the signaling pathways by which tacrolimus acts to modulate CNS neurons, like RGCs, directly.

Electrospun PEUU and PEUU-Tac constructs

To construct a tacrolimus releasing matrix, a previously reported electrospinning protocol for PEUU [310] was extended by electrospinning either 10 or 20 mg of tacrolimus blended with PEUU. Macroscopically, PEUU and 10 or 20 mg loaded PEUU-Tac matrices were off-white, pliable, and indistinguishable from one another (Figure 30a, inset). Microscopically, PEUU polymer fiber size and gross organization were also similar initially. In both PEUU and PEUU-Tac matrices, scanning electron microscopy (SEM) revealed randomly organized polymer fibers with varied diameters (Figure 30a). The average polymer fiber diameter was similar in all three matrices; unloaded PEUU fibers were 510 ±130 nm and 10 or 20 mg loaded PEUU-Tac fibers averaged 560 ± 210 nm and 560 ± 160 nm, respectively. Thus, tacrolimus loading does not alter

the gross macroscopic appearance of PEUU matrices nor the microscopic organization and diameter of electrospun PEUU polymer fibers.

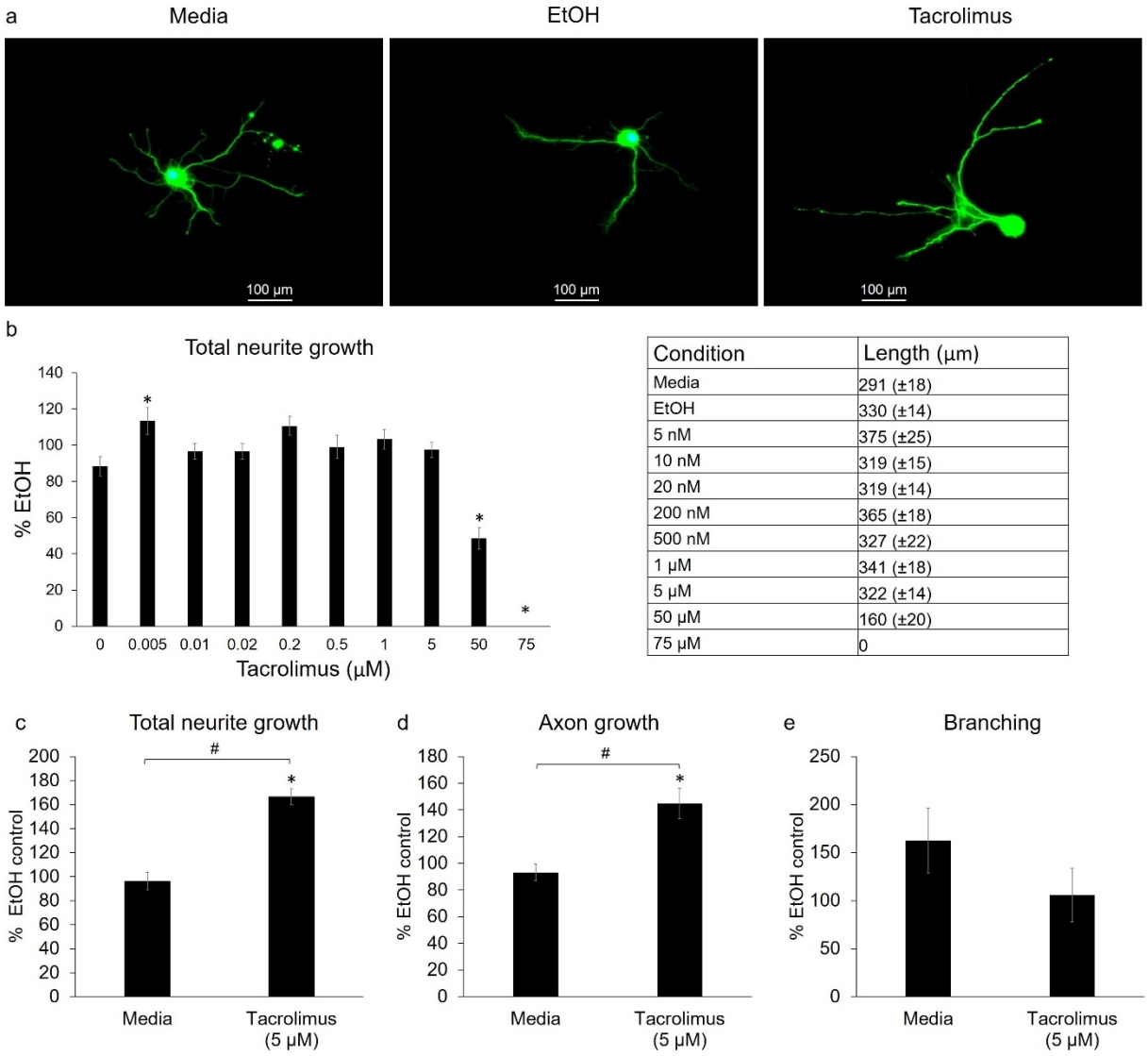

Condition	Length (µm)
Media	291 (±18)
EtOH	330 (±14)
5 nM	375 (±25)
10 nM	319 (±15)
20 nM	319 (±14)
200 nM	365 (±18)
500 nM	327 (±22)
1 µM	341 (±18)
5 µM	322 (±14)
50 µM	160 (±20)
75 µM	0

Figure 29. Total RGC neurite growth was greatest at 5 nM but did not follow a typical dose response curve in high density cultures. However, at concentrations over 5 µM, total neurite growth decreased similar to viability, reaching zero at 75 µM.

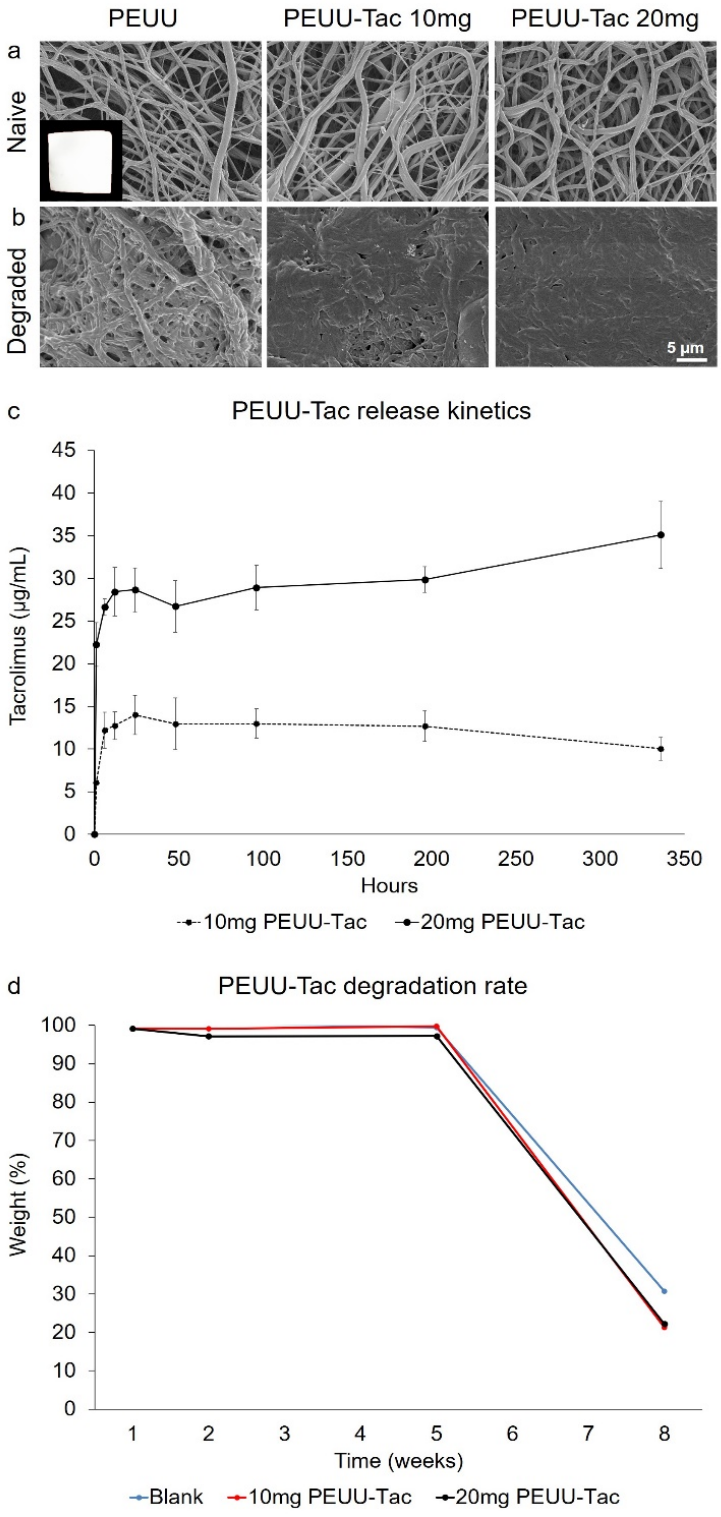

Figure 30. Macro- and microscopic PEUU and PEUU-Tac morphologies, tacrolimus release kinetics, and degradation rates.

PEUU-Tac release kinetics

Both the 10 and the 20 mg PEUU-Tac matrices released tacrolimus at similar rates, yielding final concentrations proportional to their loading concentration (Figure 30c). The 10 mg PEUU-Tac matrix yielded a maximum concentration of 11.56 μg/mL (14.5 μM) within the first 24 hours and a final concentration that was not significantly different from the 24-hour time point of 9.53 μg/mL (11.3 μM) at 14 days. The 20 mg matrix released tacrolimus similarly, yielding a concentration of 20.4 μg/mL (24.3 μM) within the first 24 hours and a final concentration of 23.7 μg/mL (28.2 μM) at 14 days that was also not significantly different from the 24-hour time point. Analysis of residual tacrolimus in PEUU-Tac matrices after 14 days showed that 85.7 ± 2.4 % was released within 24 hours and the remainder was retained in the matrix over the 14 day time point analyzed. Thus, both 10mg and 20 mg PEUU-Tac matrices release tacrolimus at similar rates *in vitro* with near maximum concentrations reached in approximately 24 hours without significant increases detected over the next 13 days analyzed.

PEUU-Tac matrix degradation *in vitro*

To determine if tacrolimus loading alters PEUU matrix degradation, we analyzed the percent change in mass of unloaded PEUU and 10 or 20 mg loaded PEUU-Tac matrices over eight weeks [314]. Changes in mass were similar for all three matrices (Figure 30d). At 1, 2, and 5 weeks, mass was largely unchanged. However, between weeks five and eight the mass decreased similarly and significantly in all three matrices. Unloaded PEUU matrix was reduced to 31 ± 1% and PEUU-Tac, 10 and 20 mg tacrolimus loaded matrices, were reduced to 21 ± 9%, and 22 ± 18%, respectively. However, these similar changes in mass, were accompanied by distinct microscopic

changes in PEUU fiber morphology that correlated with tacrolimus loading. At eight weeks, SEM showed that polymeric fibers were less defined but still distinguishable in PEUU. However, PEUU-Tac lacked identifiable polymer fibrils (Figure 30b). Thus, although changes in mass were similar, tacrolimus loading leads to a more rapid loss in polymeric fiber architecture. Despite these changes in polymer organization and losses in mass, the PEUU and PEUU-Tac matrices remained sufficiently intact to be handled manually after 8 weeks.

Mechanical properties of PEUU-Tac

The stress-strain relationship, Young's modulus, ultimate stress, and strain at break were calculated for the PEUU, 10 and 20mg PEUU-Tac matrices (Figure 31). The stress-strain relationship is shown for each PEUU device (Figure 31a). Tacrolimus loading did not significantly change Young's modulus. Unloaded PEUU was 25 ± 9 MPa, 10mg PEUU-Tac was 19 ± 12 MPa, and 20 mg PEUU-Tac was 15 ± 11 MPa (Figure 31b). Similarly, no significant difference in strain at break was observed between the PEUU (262 ± 21 %), 10mg (217 ± 67 %), and 20mg (222 ± 34 %) matrices (Figure 31c). However, ultimate stress was reduced significantly in tacrolimus loaded PEUU matrices compared to the unloaded matrix. PEUU ultimate stress was measured at 13 ± 4 MPa, 10 mg PEUU-Tac at 6 ± 0.5 MPa, and 20 mg PEUU-Tac at 6 ± 3 MPa (Figure 31d).

PEUU-Tac in an acute ON ischemia in rat

To determine if PEUU-Tac can deliver tacrolimus locally to CNS tissues trans-durally without significantly increasing blood levels, 10 mg PEUU-Tac matrices were used as nerve wraps after

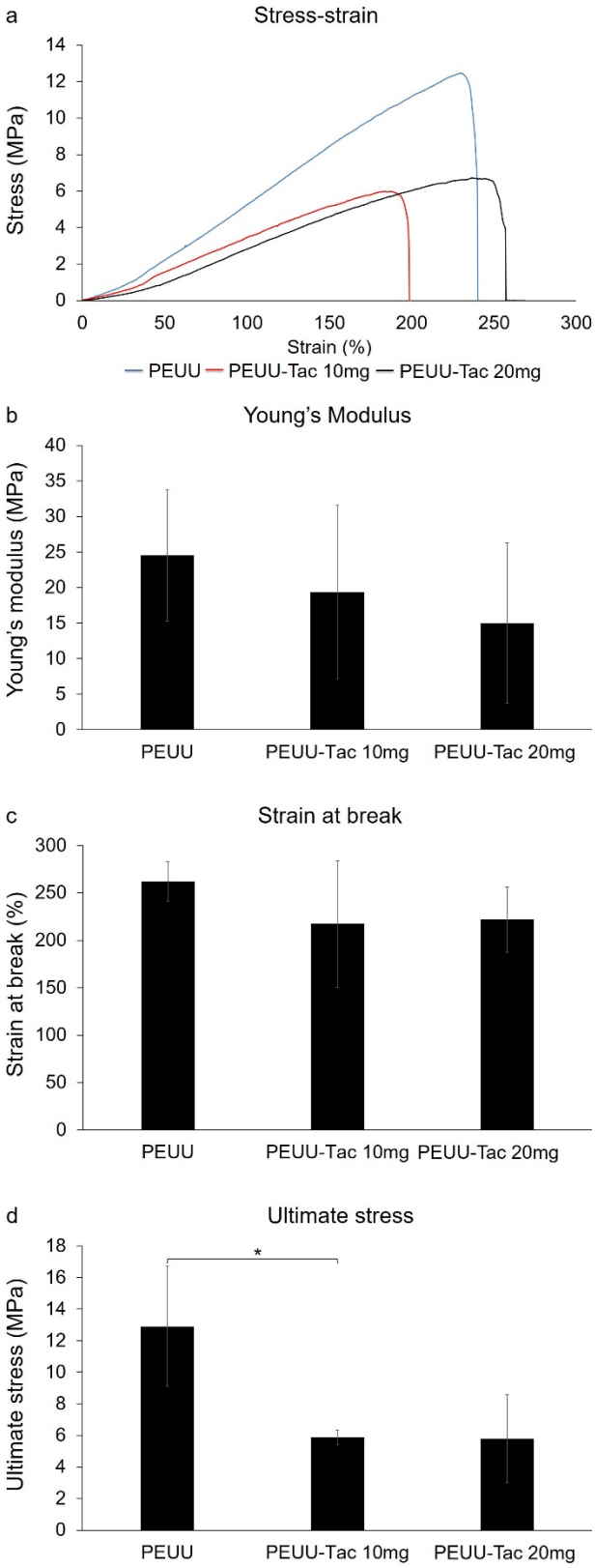

Figure 31. Mechanical properties of PEUU and PEUU-Tac matrices

acute ON ischemia in rat (Figure 32a). The ON was clamped using a Yasargil aneurism clip for 10 seconds and then either left untreated or wrapped with PEUU or PEUU-Tac around the injury site and sutured to itself and to the dura mater to prevent movement (Figure 32b). In a subset of animals, the sheath was fenestrated at the injury site to expose the ON before applying the PEUU-Tac matrix. In these *in vivo* studies, both the PEUU and PEUU-Tac sheets remained intact after 14 days, similar to our *in vitro* degradation studies, as well as previous studies using PEUU matrices in other rodent models [320, 321]. The PEUU-Tac matrices were easily removed after 14 days (Figure 32c) with obvious growth of new muscular and connective tissues. In these studies, we did not observe obvious cellular toxicity, necrosis, abnormal growth, nor inflammation in the ONs, which exhibited typical gross anatomical organization (Figure 32d).

PEUU-Tac delivered tacrolimus trans-durally to the optic nerve

Tacrolimus concentrations were analyzed in the blood, the retinas, and the ONs at 24 hours and at 14 days post injury. At 24 hours, PEUU-Tac increased tacrolimus in both fenestrated and unfenestrated ONs, but to significantly different extents (Figure 33 a-b). In fenestrated ONs, PEUU-Tac increased tacrolimus to approximately 56000 ± 4319 ng/g. In these animals, tacrolimus was also detected in the ipsilateral retina but at a much lower concentration, 1500 ± 898 ng/g, as well as in the contralateral retina, at 438 ± 31 ng/g, and ON, at 569 ± 64 ng/g (Figure 33a). In unfenestrated nerves, PEUU-Tac increased tacrolimus to approximately 5000 ± 1246 ng/g, approximately 11-fold lower than in fenestrated ONs. Similarly, tacrolimus also increased tacrolimus in the ipsilateral retina to 1900 ± 1484 µg/g, which was not significantly different than the ON. Moreover, tacrolimus was also detected in the contralateral retina at 341 ± 44 ng/g and ON at 1700 ± 225 ng/g.

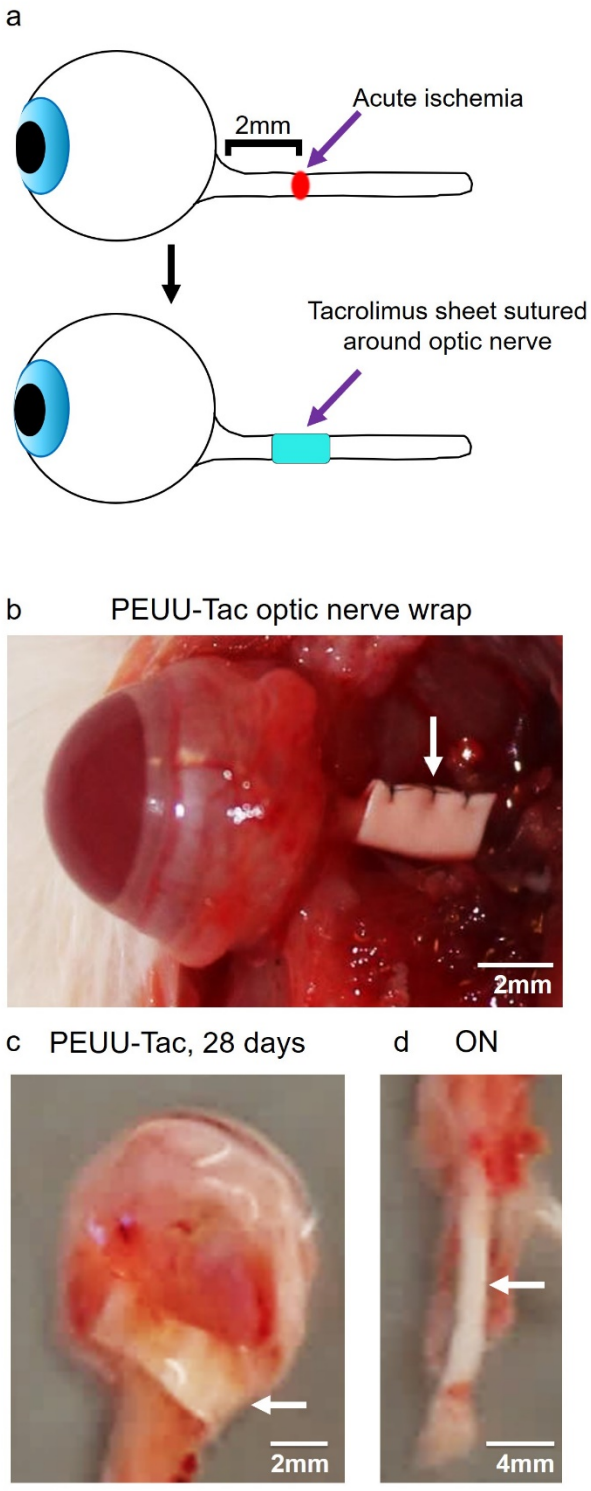

Figure 32. Surgical approach to use PEUU-Tac to treat acute optic nerve (ON) ischemia

In PEUU-Tac treated ONs, tacrolimus persisted over the 14-day time point analyzed. Despite the rapid release kinetics measured *in vitro*, tacrolimus remained detectable in PEUU-Tac treated ONs at levels similar to animals treated with tacrolimus systemically. At 14 days, tacrolimus was measured at 3300 ± 1151 ng/g in the PEUU-Tac treated ONs and at 609 ± 144 ng/g in the ipsilateral retina. In the contralateral ON, tacrolimus was measured at 2200 ± 477 ng/g and at 559 ± 100 ng/g in the contralateral retina. Thus, in the unfenestrated ONs, tacrolimus levels were increased in the right ON compared to both retinas but not the contralateral ON. Interestingly, systemic injections of tacrolimus at 2.2 mg/kg/day increased tacrolimus similarly in both ONs and in both retinas but at significantly lower levels than their accompanying ON. Tacrolimus was measured at 2200 ± 304 ng/g in the right ON and at 1700± 175 ng/g in the left ON, and at 530 ± 44 ng/g in the right retina and at 618 ± 60 ng/g in the left retina. Interestingly, tacrolimus levels in both the ONs and in the retinas were similar to the ONs and the retinas in the PEUU-Tac treated animals at 14 days post implantation (Figure 33c-d). Though further study is required, these data suggest PEUU-Tac applied to one ON delivers tacrolimus trans-durally to the treated ON and contiguous ocular tissues as effectively as daily systemic injections.

PEUU-Tac fails to increase tacrolimus blood levels significantly

Compared to systemic administration, tacrolimus blood levels in PEUU-Tac treated animals were significantly lower (Figure 33e-g). At 24 hours, tacrolimus blood concentrations were below detection. At 14 days, tacrolimus was detected at 0.15 ± 0.05 ng/mL, which is well below typical therapeutic trough levels, which range from 10-20 ng/mL. In contrast, systemic blood levels were measured at 7 ± 1 ng/mL at 24 hours and 28 ± 4 ng/mL at 14 days, above typical therapeutic trough levels. Thus, despite similar tacrolimus concentrations in the ONs and in the retinas, tacrolimus

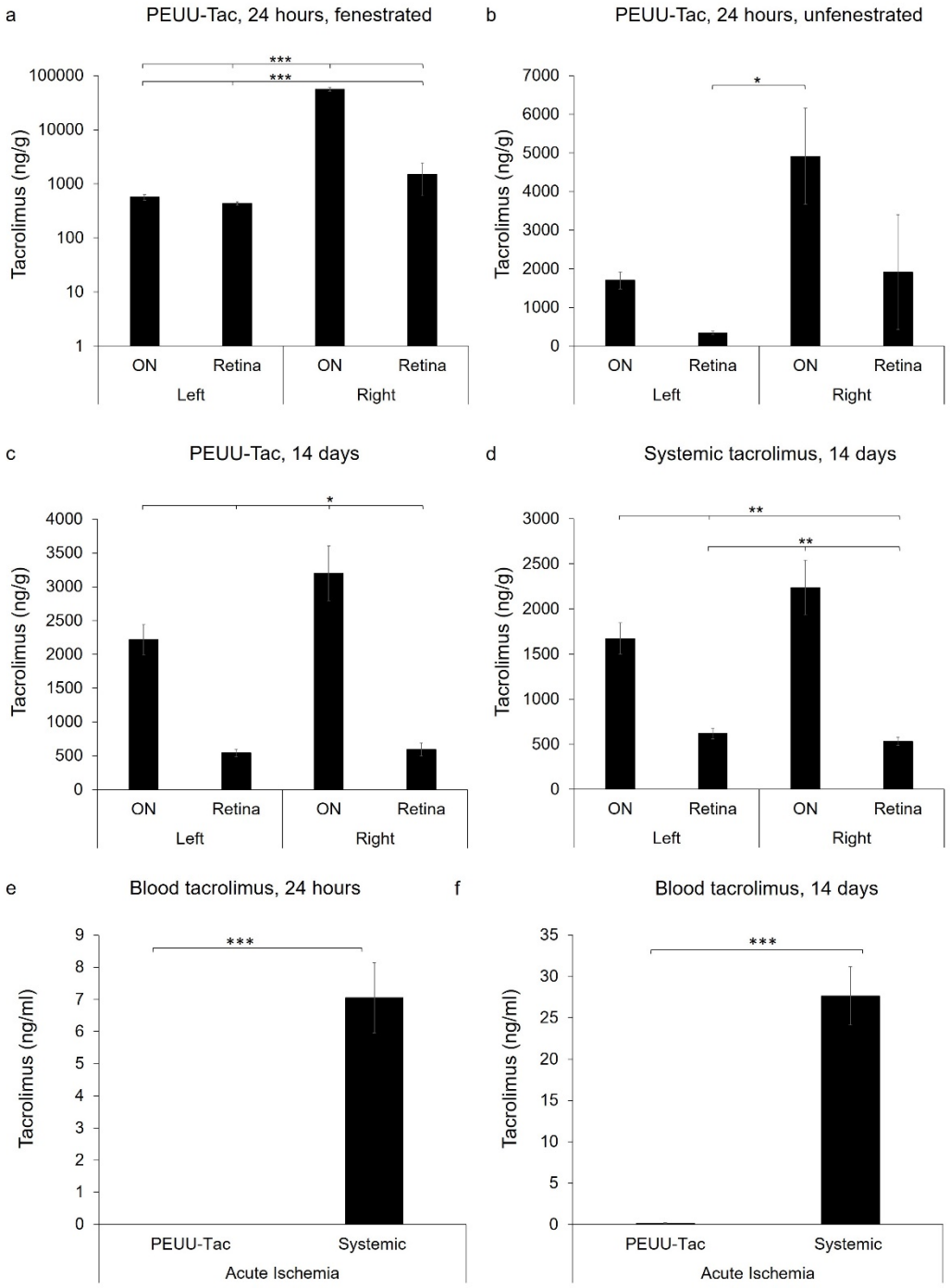

g

Group	24 hours	14 days
PEUU-Tac ON wrap	Below detection	0.15 (± 0.05) ng/ml
Systemic	7 (± 1) ng/ml	28 (± 4) ng/ml

Figure 33. Tacrolimus tissue concentrations in the optic nerves (ONs) and in the retinas. At 24 hrs, tacrolimus was undetectable in the blood in PEUU-Tac treated animals, whereas tacrolimus in systemically treated animals was significantly higher

blood levels were significantly reduced in PEUU-Tac treated animals, suggesting tacrolimus selectively accumulates in both the retinas and to a greater degree in the ONs irrespective of the administration route based on the 10 mg PEUU-Tac and systemic concentrations (2.2 mg/kg/day) used in this study.

After acute ON ischemia, PEUU-Tac downregulates GFAP expression

To determine if PEUU-Tac delivers bioactive tacrolimus trans-durally to glial cells, we analyzed *GFAP* expression, a marker for astrocyte activation, at the injury site (Figure 34). Compared to sham, uninjured nerves, *GFAP* expression increased significantly at the injury site in ONs after acute ischemia, consistent with typical astrocyte *GFAP* expression, migration, and proliferation responses to acute ON injury (Figure 34a-b). Qualitatively, increased magnification images showed obvious increases in *GFAP* expression at the injury site compared to uninjured nerves. *GFAP* was also increased in injured nerves treated with PEUU-Tac wraps or systemic tacrolimus but to a lesser extent (Figure 34c-f). Quantitatively, *GFAP* expression increased significantly in injured ONs, but not ONs wrapped in PEUU-Tac or treated systemically with tacrolimus (Figure 34g), consistent with previous systemic tacrolimus studies [322].

After acute ON ischemia, PEUU-Tac increases GAP-43 expression

To determine if PEUU-Tac delivers bioactive tacrolimus that can promote RGC axon survival or growth, we asked if PEUU-Tac increased the expression of the axon growth marker *GAP-43* (Figure 35). Compared to injured nerves, PEUU-Tac increased *GAP-43* expression dramatically along the length of the ON (Figure 35a-b). High magnification images of the injury site showed

qualitatively that both PEUU-Tac and systemic tacrolimus increased *GAP-43* expression compared to injured, untreated nerves (Figure 35 c-f), consistent with previous studies analyzing the effects of systemic tacrolimus on CNS axons after acute ischemic CNS injury [299, 318]. However, quantitatively, PEUU-Tac, but not systemic tacrolimus, increased *GAP-43* expression significantly in the ON (Figure 35g). Though more detailed cellular analyses are warranted, these results demonstrate feasibility by showing that PEUU-Tac can deliver bioactive tacrolimus trans-durally to the ON to positively effect cellular markers indicative of a more positive tissue remodeling response to injury in the CNS.

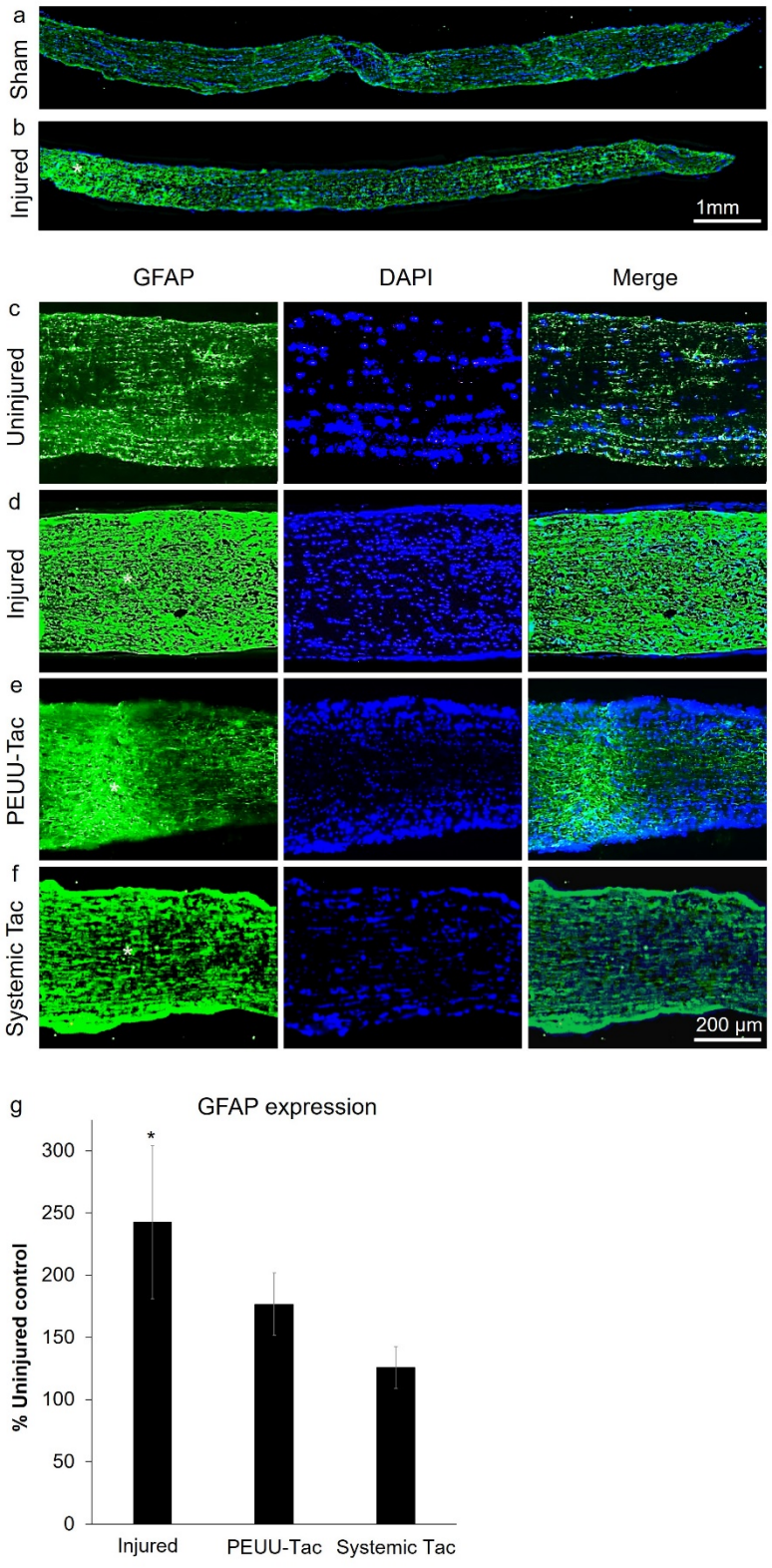

Figure 34. PEUU-Tac decreases GFAP expression at the injury site. GFAP expression increased significantly in injured ONs but not in ONs treated by PEUU-Tac or systemic tacrolimus

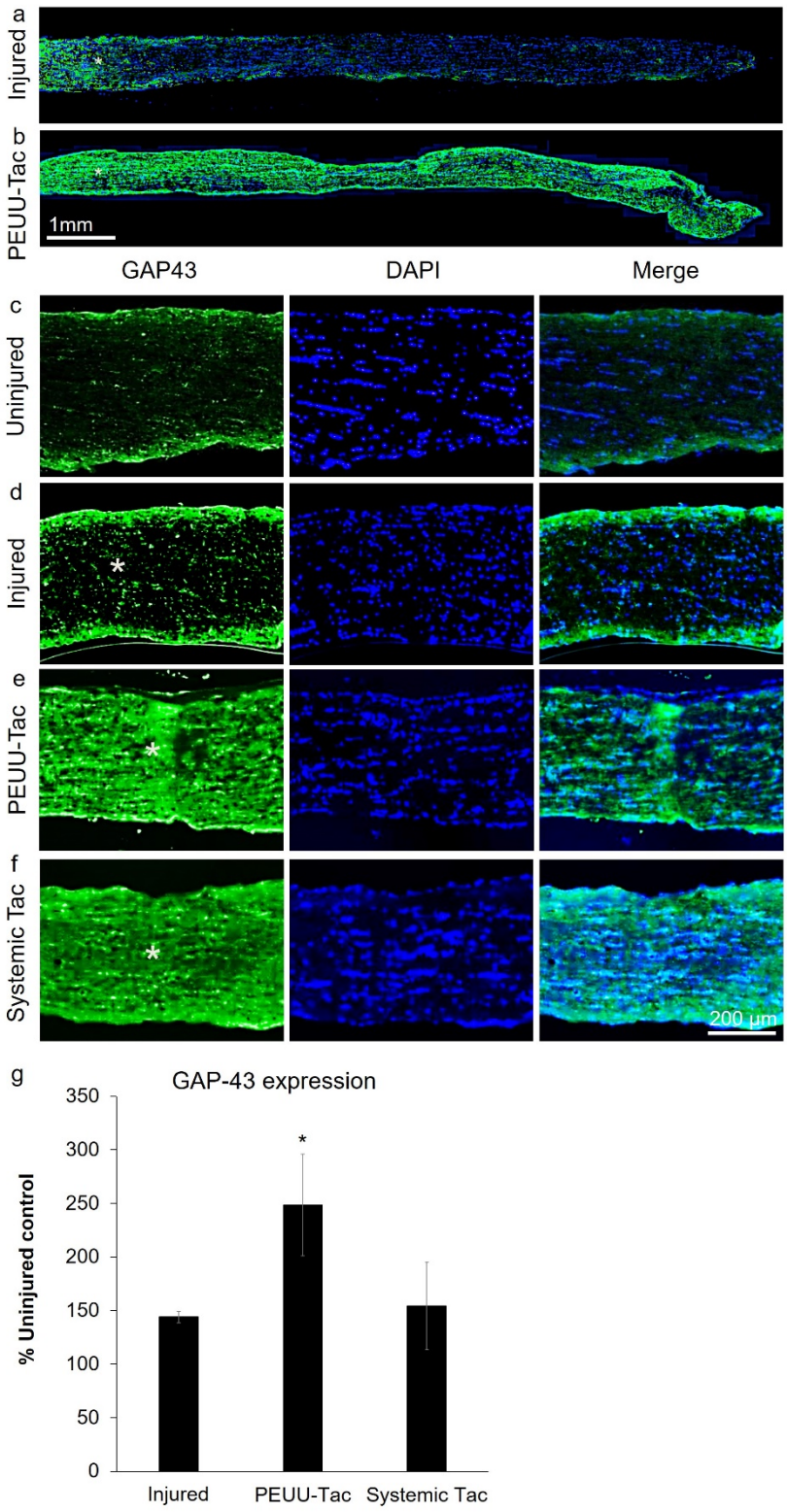

Figure 35. PEUU-Tac increases GAP43 expression at the injury site. GAP43 expression increased significantly in ONs treated with PEUU-Tac or systemic tacrolimus.

DISCUSSION

This study shows PEUU-Tac matrices, manufactured by electrospinning blended PEUU and tacrolimus, can be used to locally deliver bioactive tacrolimus trans-durally to CNS tissues without significantly raising blood levels. Tacrolimus is a macrolide calcineurin inhibitor often used as an immunosuppressant after allogeneic organ transplantation. In solid organ transplantation, life-long systemic tacrolimus immunosuppression is typically required to prevent rejection. Tacrolimus also has desirable neuroprotective and neuroregenerative properties for treating peripheral nerve or CNS injury and disease. However, treating nervous system tissues with systemic tacrolimus is complicated by the pharmacokinetic properties of tacrolimus. Tacrolimus is highly lipophilic and thus accumulates in fatty tissues throughout the body, including the myelin-based white matter in the CNS. However, for reasons not completely understood, higher systemic tacrolimus concentrations are necessary to effectively increase tacrolimus levels in CNS tissues. Due to the narrow therapeutic window for tacrolimus, systemic increases are not feasible since they would likely lead to toxic secondary exposures and potentially life-threatening side effects in non-targeted tissues or organs. Fortunately, pre-clinical models of acute ischemic nervous system injury indicate shorter therapeutic time windows are more effective in promoting positive CNS tissue remodeling, like increased axon growth [299, 300, 323]. These shorter therapeutic windows are in agreement with early modulation of the pro-inflammatory innate immune response and preventing or suppressing injury-induced microglial and astrocyte activation [324], which can increase CNS neuron survival [38] and decrease cellular and ECM remodeling preceding scar tissue formation [244]. Modulating the early innate immune response has been shown to be a critical factor in vertebrates that can functionally regenerate CNS tissues [325]. Thus, the PEUU-Tac matrix reported here may fill a clinical need by providing a platform combining two FDA

approved materials, into a tunable platform that can be secured in place to effectively deliver tacrolimus trans-durally to CNS tissues. Moreover, PEUU can be easily tuned with additional genetic and biochemical reagents tailored to the nature and the scope of the injury.

PEUU-Tac has desirable mechanical and biocompatible properties for treating CNS tissues. Like PEUU [310], PEUU-Tac is a flexible, biodegradable polymeric matrix that can be easily cut, shaped, and sutured to the dura mater with mechanical and degradation properties that can be easily tuned to match the tissue of interest. In this study, PEUU-Tac's mechanical properties closely matched the biomechanical properties of the dura mater surrounding the CNS in both rodents and in humans. Matching biomechanics is necessary to effectively sustain physiologically applied mechanical forces [326]. In fact, PEUU was chosen specifically for this reason since PEUU polymers can be easily tuned to match the biomechanical properties of different tissues of interest [310, 312]. In this study, PEUU-Tac matrices had breaking strains around 200% and tensile strengths around 6 MPa. In rat, the tensile strength for rat dura mater is generally reported to be under 3 MPA with breaking strains around 140% [327, 328] and, similarly, tensile strengths for human dura mater have been reported to be approximately 1-5 MPa with breaking strains considerably lower than PEUU [329-331]. Thus, the PEUU-Tac matrices appear to be a good match biomechanically for trans-dural drug delivery to CNS tissues.

In vitro, PEUU-Tac released tacrolimus rapidly, approximately 85% was released within 24 hours, resulting in a local concentration of 9.53 µg/mL or 11.3 µM for the 10 mg PEUU-Tac used in *in vivo* studies. After acute ON ischemia in rat, an ophthalmic surgeon surgically inserted PEUU-Tac through a narrow, almost bloodless conjunctival plane, wrapped the PEUU-Tac around the ON at the injury site by looping a suture connected to the wrap around the ON. The PEUU matrix was then sutured both to itself and to the dura to prevent movement. Like PEUU, PEUU-

Tac exhibited good tolerance *in vivo* and possessed good suture retention. Obvious cellular toxicity, necrosis, abnormal growth, or inflammation were unobserved. After 2 weeks *in vivo*, PEUU-Tac matrices appeared intact and were easily removed, suggesting that if necessary, the matrices could have been removed earlier since tacrolimus release from PEUU-Tac was essentially complete within 24 hours. Moreover, PEUU matrices could be replaced if needed with the same or different matrices to treat different phases of the default healing response in the CNS [332]. Finally, the ability of a trained surgeon to perform this procedure in a rodent model is encouraging for treating ONs in humans, which provide easier access and greater exposure, but also for treating spinal cord, brain, and peripheral nerve injuries where biomechanical tissue compliance during flexion and/or suturing are desired.

PEUU-Tac delivered tacrolimus to ONs trans-durally without significantly increasing blood levels. In fenestrated ONs, tacrolimus increased to 56,000 ng/g, or approximately 70 μM, well above the toxicity limit (LD_{50}=24 μM) measured for primary RGCs *in vitro* and above levels considered safe clinically which are typically in the low ng/g range. In unfenestrated nerves, PEUU-Tac also successfully increased tacrolimus but to levels 10-fold lower at 5000 ng/g or approximately 6 μM within 24 hours. In PEUU-Tac treated ONs, tacrolimus remained detectable at 14 days, at around 3200 ng/g or 3.8 μM, which is still well above clinically accepted levels. Moreover, these concentrations are several hundred fold higher than blood trough concentrations (> 10-30 ng/mL or 10-30 nM) shown to be neurotoxic in the CNS [333, 334] and in the PNS [335]. Tacrolimus was also detected in the contralateral ON (2200 ng/g, 2.6 μM) and at lower levels in both the ipsilateral (591 ng/g, 0.7 μM) and contralateral (541 ng/g, 0.66 μM) retinas, indicating contiguous ocular tissues also absorbed tacrolimus. However, despite high ON levels and detection in other ocular tissues, tacrolimus was undetectable in the blood at 24 hours and

minimally detected at 0.15 ± 0.05 ng/mL after 14 days compared to systemic tacrolimus blood levels measured at 27.66 ± 3.53 ng/mL after 14 days. These results indicate PEUU-Tac can deliver tacrolimus trans-durally to CNS tissues. However, the initial tacrolimus concentration measured in this study are too high, requiring either lower initial tacrolimus concentrations in the PEUU-Tac matrix and/or slower release kinetics, both properties that are easily modified and expected to further reduce absorption by adjacent ocular tissues and by the blood. Using data from this study and physiologically based pharmacokinetics, studies are ongoing to determine the appropriate tacrolimus loading concentrations and release kinetics from PEUU-Tac to maximize the cellular responses to acute ischemic injury and to minimize neurotoxicity.

After acute ON ischemia, PEUU-Tac positively modulated typical markers of the default healing response in CNS tissues. After ON injury, injured RGC axons typically degenerate [336] and astrocytes, among other immune and glial cells, proliferate and migrate to the injury site, locally increasing *GFAP* expression and contribute to scar tissue formation [32]. In PEUU-Tac wrapped nerves, *GFAP* expression increased but to significantly lower levels at the injury site than in untreated, injured ONs. Moreover, in PEUU-Tac treated nerves *GAP-43* expression increased along the length of the ON, similar to observations after systemic tacrolimus delivery [299, 318]. Though additional cellular and functional studies are required, these initial data show that, despite the high tacrolimus ON concentrations measured, PEUU-Tac delivers bioactive tacrolimus trans-durally that is sufficient to decrease *GFAP* expression and presumably astrogliosis, while increasing *GAP-43* expression and presumably RGC axon growth. Once tacrolimus loading and/or release kinetics are optimized for the PEUU-Tac matrices, future studies will include functional studies to correlate axon growth and decreased astrocyte activation with neuronal signaling and visual function.

Though these initial studies demonstrate feasibility, several caveats need to be addressed for optimizing PEUU-Tac for functional studies. FKBPs are enriched in CNS tissues [337] and tacrolimus is highly lipophilic, suggesting tacrolimus may selectively accumulate in CNS tissues with high myelin content, like the ON. Though oligodendrocytes may not express FKBP [338], tacrolimus influences myelination [339] and oligodendrocyte survival *in vitro* [340, 341]. Second, different FKBP receptors are differentially expressed by CNS neurons like RGCs [297] and many glial cells, resulting in varying regulation of different signaling pathways involved in cell cycle control [342], neuronal motility [343], and apoptosis [344], highlighting the importance of analyzing the inter- and intracellular effects of tacrolimus within CNS cellular populations. Third, tacrolimus has also been shown to effect blood brain barrier integrity and function [344] and thus may differentially regulate absorption, particularly at local delivery sites where tacrolimus concentrations are high. Regulating tacrolimus tissue and blood levels is critical due to the narrow therapeutic index, tissue absorption variability, and pharmokinetic variability, [345] and thus is further complicated by the number of cellular targets and compartmentalization. Hence, bioavailability of tacrolimus differs across cellular populations. Whether the measured tacrolimus concentration in the ON in this study accurately reflects tacrolimus bioavailability is unknown, but this information is required to properly tune PEUU-Tac matrices for dosing. Clinically, tacrolimus doses are based on whole blood trough levels, which poorly predict tissue levels; even within the therapeutic range, toxicity may occur [346]. Furthermore, physiology, age, and concurrent medications can alter tacrolimus levels and biological activity [347]. Thus, tacrolimus tissue concentrations at target sites may better predict outcomes [348], highlighting the need to optimize tacrolimus delivery time and concentration indices for CNS tissues specifically prior to conducting functional studies.

CONCLUSION

Injury to CNS tissues like the ON often leads to a pro-inflammatory innate immune response, negative tissue remodeling to form scar tissue, and axon degeneration that leads to permanently lost neurological function. The PEUU-Tac matrix proposed here utilizes cost effective materials already used in FDA approved products. These materials are readily available, do not produce adverse immune responses when used correctly, and are highly translatable clinically. The combination of the two materials provides a device capable of being tailored to a patient's specific injury, increasing the probability of a positive outcome. Clinically, tacrolimus has a narrow therapeutic index and high inter- and intra-individual pharmacokinetic variability, necessitating therapeutic drug monitoring to individualize dosage. The sustained detection of tacrolimus in the ON and positive effects on tissue remodeling indicate that a single PEUU-Tac application may be sufficient to treat ON injury where systemic administration requires frequent injections to maintain the same tacrolimus levels. Thus, PEUU-Tac could greatly reduce issues with patient compliance/adherence to the treatment and decrease the chances of unwanted, potentially life-threatening side-effects [304, 349, 350].

APPENDIX B

PRESENTAITON AND PUBLICATION LIST

PUBLISHED MANUSCRIPTS

1. Yang XL, **van der Merwe Y**, Sims J, Parra C, Ho LC, Schuman JS, Wollstein G, Lathrop KL, Chan KC. Age-related changes in eye, brain and visuomotor behavior in the DBA/2J mouse model of chronic glaucoma. Scientific Reports. 2018. 8:4643.
2. Ren T, Faust AE, **van der Merwe Y**, Xiao B, Johnson S, Kandakatla A, Gorantla VS, Badylak SF, Washington KM, Steketee MB. Fetal extracellular matrix nerve wraps locally improve peripheral nerve remodeling after complete transection and direct repair in rat. Scientific Reports. 2018. 8:4474.
3. **Van der Merwe Y,** Steketee MB. Extracellular Vesicles: Biomarkers, Therapeutics, and Vehicles in the Visual System. Curr Ophthalmol Rep. 2017;5(4):276-282. Epub 2017 Oct 6.
4. **Van der Merwe Y,** Faust AE, Conner I, Gu X, Feturi F, Zhao W, Leonard B, Roy S, Gorantla VS, Venkataramanan R, Washington KM, Wagner WR, Steketee MB. EBioMedicine. 2017 Dec;26:47-59. Epub 2017 Nov 24

5. **Van der Merwe Y**, Faust AE, Steketee MB. Matrix bound vesicles and miRNA cargoes are bioactive factors within extracellular matrix bioscaffolds. Neural Regen Res. 2017 Oct;12(10):1597-1599.

6. Voorhees AP, Ho LC, Jan NJ, Tran H, **van der Merwe Y**, Chan K, Sigal IA. Whole-globe biomechanics using high-field MRI. Exp Eye Res. 2017 Jul;160:85-95. Epub 2017 May 17

7. Faust A, Kandakatla A, **van der Merwe Y**, Ren T, Huleihel L, Hussey G, Naranjo JD, Johnson S, Badylak S, Steketee M. Urinary bladder extracellular matrix hydrogels and matrix-bound vesicles differentially regulate central nervous system neuron viability and axon growth and branching. J Biomater Appl. 2017 Apr;31(9):1277-1295. Epub 2017 Mar 9.

8. Chan KC, Zhou IY, Liu SS, **van der Merwe Y**, Fan SJ, Hung VK, Chung SK, Wu WT, So KF, Wu EX. Longitudinal assessments of normal and perilesional tissue sin focal brain ischemia and partial optic nerve injury with manganese-enhanced MRI. Sci Rep. 2017 Feb 23;7:43124

9. Kancherla S, Kohler WJ, **van der Merwe Y**, Chan KC. N vivo evaluation of the visual pathway in streptozotocin-induced diabetes by diffusion tensor MRI and contrast enhanced MRI. PLoS One. 2016 Oct 21;11(10):e0165169. eCollection 2016.

10. Ho LC, Sigal IA, Jan NJ, Yang X, **van der Merwe Y**, Yu Y, Chau Y, Leung CK, Conner IP, Jin T, Wu EX, Kim SG, Wollstein G, Schuman JS, Chan KC. Non-invasive MRI assessments of tissue microstructures and macromolecules in the eye upon biomechanical or biochemical modulation. Sci Rep. 2016 Aug 26;6:32080

11. **van der Merwe Y,** Steketee MB. Immunomodulatory approaches to CNS injury: extracellular matrix and exosomes from extracellular matrix conditioned macrophages. Neural Regen Res. 2016 Apr;11(4):554-6.

12. Ren T, **van der Merwe Y**, Steketee MB. Developing extracellular matrix technology to treat retinal or optic nerve injury eNeuro. 2015 Oct 8;2(5). pii: ENEURO.0077-15.2015. eCollection 2015 Sep. Review.

13. Ho LC, Wang B, Conner IP, **van der Merwe Y**, Bilonick RA, Kim SG, Wu EX, Sigal IA, Wollstein G, Schuman JS, Chan KC. In vivo evaluation of white matter integrity and anterograde transport in visual system after excitotoxic retinal injury with multimodal MRI and OCT. Invest Ophthalmol Vis Sci. 2015 Jun;56(6):3788-800. doi: 10.1167/iovs.14-15552.

14. Crapo PM, Medberry CJ, Reing JE, Tottey S, **van der Merwe Y**, Jones KE, Badylak SF. Biologic scaffolds composed of central nervous system extracellular matrix. Biomaterials. 2012 May;33(13):3539-47. Epub 2012 Feb 14

FILED PATENTS

1. KM Washington, WR Wagner, MB Steketee, **Y van der Merwe**, X Gu. Devices and methods for local delivery to nervous system tissue. UPitt Ref.: 03767. Filed: 06/23/2017
2. **Y van der Merwe**, AE Faust, GS Hussey, WR Wagner, SF Badylak, MB Steketee. Matrix bound vesicles (MBVs) ocular applications. UPitt Ref.: 04230. Filed 05/05/2017

PRESENTATIONS

1. Neuroimaging and optokinetics reveal changes in brain microstructure and visuomotor behavior following ocular hypertension, **Yolandi van der Merwe, B.Eng., Leon C. Ho, B.Eng., Xiaoling Yang, M.D., Michael B. Steketee, Ph.D., Kevin C. Chan, Ph.D.,** Science 2014, October 3rd, 2014
2. Neuroimaging and optokinetics reveal changes in brain microstructure and visuomotor behavior following ocular hypertension, **Yolandi van der Merwe, B.Eng., Leon C. Ho, B.Eng., Xiaoling Yang, M.D., Michael B. Steketee, Ph.D., Kevin C. Chan, Ph.D.,** Pittsburgh Imaging Community Retreat, November 3rd, 2014
3. Elevating intraocular pressure acutely compromises optic nerve integrity and visuomotor behavior without an apparent change in axonal transport, **Yolandi van der Merwe, Leon C. Ho, Xiaoling Yang, Ian P. Conner, Seong-Gi Kim, Gadi Wollstein, Joel S. Schuman, Michael B. Steketee, Kevin C. Chan,** McGowan Retreat, March 8th, 2015
4. Acute intraocular pressure elevation compromises optic nerve integrity and visuomotor behavior without apparent change in axonal transport, **Yolandi van der Merwe, Leon Ho, Xiaoling Yang, Ian P. Conner, Seong-Gi Kim, Gadi Wollstein, Joel S. Schuman, Michael B. Steketee, Kevin C. Chan,** ARVO, May 2nd, 2015
5. Intraocular Pressure Elevation Induced by Crosslinking Hydrogel Injection Leads to Morphological and Microstructural Changes in the Eye and Visual Pathway, **Yolandi van der Merwe, Leon Ho, Ian P. Conner, Xiaoling Yang, Yu Yu,**

Christopher K. Leung, Ian A. Sigal, Gadi Wollstein, Joel S. Schuman, Michael B. Steketee, Kevin C. Chan, ARVO, May 2nd, 2015

6. In vivo evaluation of ocular physiology and structural integrity of the optic nerve upon whole eye transplantation using gadolinium-enhanced MRI and diffusion tensor imaging, **Yolandi van der Merwe, Leon C. Ho, Yang Li, Maxine R. Miller, Chiaki Komatsu, Hongkun Wang, Michael B. Steketee, Seong-Gi Kim, Joel S. Schuman, Kia M. Washington, Kevin C. Chan, and the WET Consortium,** International Society for Magnetic Resonance in Medicine, June 1st, 2015
7. Longitudinal characterization of brain microstructure and visuomotor behavior following acute ocular hypertension using diffusion tensor imaging, magnetization transfer imaging, and optokinetics, **Yolandi van der Merwe, Leon C. Ho, Xiaoling Yang, Seong-Gi Kim, Gadi Wollstein, Joel S. Schuman, Michael B. Steketee, Kevin C. Chan,** International Society for Magnetic Resonance in Medicine, June 1st, 2015
8. Intraocular Pressure Elevation Induced by Crosslinking Hydrogel Injection Leads to Morphological and Microstructural Changes in the Eye and Visual Pathway, **Yolandi van der Merwe, Leon C. Ho, Xiaoling Yang, Ian P. Conner, Seong-Gi Kim, Gadi Wollstein, Joel S. Schuman, Michael B. Steketee, Kevin C. Chan,** Vision Research Day, June 19th, 2015
9. Longitudinal characterization of brain microstructure and visuomotor behavior following acute intraocular pressure elevation using diffusion tensor imaging, magnetization transfer imaging, and optokinetics, **Yolandi van der Merwe, Leon**

C. Ho, Xiaoling Yang, Seong-Gi Kim, Gadi Wollstein, Joel S. Schuman, Michael B. Steketee, Kevin C. Chan, Vision Research Day, June 19th, 2015

10. Acute intraocular pressure elevation compromises optic nerve integrity and visuomotor behavior without apparent change in axonal transport, **Yolandi van der Merwe, Leon Ho, Xiaoling Yang, Ian P. Conner, Seong-Gi Kim, Gadi Wollstein, Joel S. Schuman, Michael B. Steketee, Kevin C. Chan,** Vision Restoration Day, June 26th, 2015
11. Using extracellular matrix technology to promote retinal ganglion cell survival and axon regeneration, **Yolandi van der Merwe, Ian Conner, Anne Faust, Xinzhu Gu, Asma Naqvi, Tanchen Ren, Apoorva Kandakatla, Vibha Reddy, Bo Wang, Katie Lucy, Fardeen Mehdi, Lydia Lewis, Hannah Song, Kevin Chan, Gadi Wollstein, Kia Washington, William Wagner, Stephen Badylak, Michael Steketee,** SFN, October 19th, 2015
12. Localized FK506 delivery for optic nerve regeneration. **Yolandi van der Merwe, Kia M. Washington, MD, Anne E. Faust, Ian Conner, Xinzhu Gu, Chris Kaufman, Fardeen Mehdi, Asma Naqvi, Tanchen Ren, Kevin C. Chan, PhD, Raman Venkataramanan, William R. Wagner, PhD, Michael B. Steketee, PhD.** McGowan Retreat, March 6th, 2016
13. Neurobehavioral effects of acute and chronic intraocular pressure elevation on the visual system by OCT, MRI and optokinetic assessments. **Yolandi van der Merwe; Jenny J. Liu; Katie A. Lucy; Bo Wang; Xiaoling Yang; Leon Ho; Yu Yu; Christopher K. Leung; Ian P. Conner; Gadi Wollstein; Joel S. Schuman;**

Michael B. Steketee; Kevin C. Chan. ARVO Imaging of the Eye, April 29th, 2016, Seattle, Washington.

14. Citicoline preserves optic nerve integrity and visuomotor function following chronic intraocular pressure elevation. **Yolandi van der Merwe, Xiaoling Yang, Leon C. Ho, Yu Yu, Ying Chau, Christopher Leung, Ian Conner, Michael B. Steketee, Gadi Wollstein, Joel S. Schuman, Kevin C. Chan.** ARVO, May 3rd, 2016, Seattle, Washington.
15. Oral citicoline treatment improves visuomotor response and white matter integrity in the visual pathway after chronic intraocular pressure elevation. **Yolandi van der Merwe, Xiaoling Yang, Leon C. Ho, Yu Yu, Christopher Leung, Ian Conner, Gadi Wollstein, Joel S. Schuman, Michael B. Steketee, Kevin C. Chan.** International Society for Magnetic Resonance in Medicine, May 13th, 2016, Singapore
16. Localized FK506 delivery for CNS neuroprotection**. Yolandi van der Merwe, Chris Kaufman, Anne E. Faust, Ian Conner, Xinzhu Gu, Tanchen Ren, Fardeen Mehdi, Asma Naqvi, Kevin C. Chan, PhD, Kia M. Washington, MD, Raman Venkataramanan, William R. Wagner, PhD, Michael B. Steketee, PhD.** FCVR, June 20th, 2016
17. Localized FK506 delivery for CNS neuroprotection**. Yolandi van der Merwe, Anne E. Faust, Ian Conner, Xinzhu Gu, Chris Kaufman, Tanchen Ren, Fardeen Mehdi, Asma Naqvi, Kevin C. Chan, PhD, Kia M. Washington, MD, Raman Venkataramanan, William R. Wagner, PhD, Michael B. Steketee, PhD.** MHSRS, August 2016, Kissimmee, Florida

18. Citicoline preserves optic nerve integrity and visuomotor function following chronic intraocular pressure elevation. **Yolandi van der Merwe, Xiaoling Yang, Leon C. Ho, Yu Yu, Christopher Leung, Ian Conner, Gadi Wollstein, Joel S. Schuman, Michael B. Steketee, Kevin C. Chan.** Brain Day, November 4th, 2016
19. Extracellular vesicles purified from porcine vitreous positively regulate retinal ganglion cell axon survival and growth. **Yolandi van der Merwe, Anne E. Faust, Bianca Leonard, Mark Curtis, Apoorva Kandakatla, Kevin C. Chan, and Michael B. Steketee**. ARVO, May 2017, Baltimore, Maryland.

BIBLIOGRAPHY

1. Ophthalmology, A.A.o., *Eye Health Statistics.* https://www.aao.org/newsroom/eye-health-statistics, 2018.
2. Blindness, P., *The Scope of the Eye Injury Problem.* https://www.preventblindness.org/, 2018.
3. McGwin, G., Jr., A. Xie, and C. Owsley, *Rate of eye injury in the United States.* Arch Ophthalmol, 2005. **123**(7): p. 970-6.
4. Institute, N.E., *All Vision Impairment.* https://www.nei.nih.gov, 2018.
5. Institute, N.E., *Blindness.* https://www.nei.nih.gov, 2018.
6. Wittenborn, J.S., et al., *The economic burden of vision loss and eye disorders among the United States population younger than 40 years.* Ophthalmology, 2013. **120**(9): p. 1728-35.
7. Le Bihan, D. and H. Johansen-Berg, *Diffusion MRI at 25: exploring brain tissue structure and function.* Neuroimage, 2012. **61**(2): p. 324-41.
8. Ho, L.C., et al., *Non-invasive MRI Assessments of Tissue Microstructures and Macromolecules in the Eye upon Biomechanical or Biochemical Modulation.* Sci Rep, 2016. **6**: p. 32080.
9. Henkelman, R.M., G.J. Stanisz, and S.J. Graham, *Magnetization transfer in MRI: a review.* NMR Biomed, 2001. **14**(2): p. 57-64.
10. Aoki, I., S. Naruse, and C. Tanaka, *Manganese-enhanced magnetic resonance imaging (MEMRI) of brain activity and applications to early detection of brain ischemia.* NMR Biomed, 2004. **17**(8): p. 569-80.
11. Pautler, R.G., *In vivo, trans-synaptic tract-tracing utilizing manganese-enhanced magnetic resonance imaging (MEMRI).* NMR Biomed, 2004. **17**(8): p. 595-601.
12. Pautler, R.G., A.C. Silva, and A.P. Koretsky, *In vivo neuronal tract tracing using manganese-enhanced magnetic resonance imaging.* Magn Reson Med, 1998. **40**(5): p. 740-8.
13. Chan, K.C., et al., *In vivo manganese-enhanced MRI and diffusion tensor imaging of developing and impaired visual brains.* Conf Proc IEEE Eng Med Biol Soc, 2011. **2011**: p. 7005-8.

14. Chan, K.C., et al., *Evaluation of the retina and optic nerve in a rat model of chronic glaucoma using in vivo manganese-enhanced magnetic resonance imaging.* Neuroimage, 2008. **40**(3): p. 1166-74.

15. Chan, K.C. and E.X. Wu, *In vivo manganese-enhanced MRI for visuotopic brain mapping.* Conf Proc IEEE Eng Med Biol Soc, 2012. **2012**: p. 2279-82.

16. Haenold, R., et al., *Magnetic resonance imaging of the mouse visual pathway for in vivo studies of degeneration and regeneration in the CNS.* Neuroimage, 2012. **59**(1): p. 363-76.

17. Sandvig, A., et al., *Axonal tracing of the normal and regenerating visual pathway of mouse, rat, frog, and fish using manganese-enhanced MRI (MEMRI).* J Magn Reson Imaging, 2011. **34**(3): p. 670-5.

18. Pautler, R.G., *Biological applications of manganese-enhanced magnetic resonance imaging.* Methods Mol Med, 2006. **124**: p. 365-86.

19. Van der Linden, A., et al., *Current status of functional MRI on small animals: application to physiology, pathophysiology, and cognition.* NMR Biomed, 2007. **20**(5): p. 522-45.

20. Watanabe, T., J. Frahm, and T. Michaelis, *Functional mapping of neural pathways in rodent brain in vivo using manganese-enhanced three-dimensional magnetic resonance imaging.* NMR Biomed, 2004. **17**(8): p. 554-68.

21. Wang, J., et al., *Structural brain alterations in primary open angle glaucoma: a 3T MRI study.* Sci Rep, 2016. **6**: p. 18969.

22. Wang, J., et al., *Graph theoretical analysis reveals the reorganization of the brain network pattern in primary open angle glaucoma patients.* Eur Radiol, 2016. **26**(11): p. 3957-3967.

23. Bien, A., et al., *Apoptotic versus necrotic characteristics of retinal ganglion cell death after partial optic nerve injury.* J Neurotrauma, 1999. **16**(2): p. 153-63.

24. Slater, B.J., et al., *Rodent anterior ischemic optic neuropathy (rAION) induces regional retinal ganglion cell apoptosis with a unique temporal pattern.* Invest Ophthalmol Vis Sci, 2008. **49**(8): p. 3671-6.

25. Warner, N. and E. Eggenberger, *Traumatic optic neuropathy: a review of the current literature.* Curr Opin Ophthalmol, 2010. **21**(6): p. 459-62.

26. Goldberg, J.L., et al., *Amacrine-signaled loss of intrinsic axon growth ability by retinal ganglion cells.* Science, 2002. **296**(5574): p. 1860-4.

27. Lathrop, K.L. and M.B. Steketee, *Mitochondrial Dynamics in Retinal Ganglion Cell Axon Regeneration and Growth Cone Guidance.* J Ocul Biol, 2013. **1**(2): p. 9.

28. Mansour-Robaey, S., et al., *Effects of ocular injury and administration of brain-derived neurotrophic factor on survival and regrowth of axotomized retinal ganglion cells.* Proc Natl Acad Sci U S A, 1994. **91**(5): p. 1632-6.

29. McKeon, R.J., M.J. Jurynec, and C.R. Buck, *The chondroitin sulfate proteoglycans neurocan and phosphacan are expressed by reactive astrocytes in the chronic CNS glial scar.* J Neurosci, 1999. **19**(24): p. 10778-88.

30. Tang, S., et al., *Soluble myelin-associated glycoprotein released from damaged white matter inhibits axonal regeneration.* Mol Cell Neurosci, 2001. **18**(3): p. 259-69.

31. Horn, K.P., et al., *Another barrier to regeneration in the CNS: activated macrophages induce extensive retraction of dystrophic axons through direct physical interactions.* J Neurosci, 2008. **28**(38): p. 9330-41.

32. Silver, J. and J.H. Miller, *Regeneration beyond the glial scar.* Nat Rev Neurosci, 2004. **5**(2): p. 146-56.

33. Butt, A.M., et al., *Functions of optic nerve glia: axoglial signalling in physiology and pathology.* Eye (Lond), 2004. **18**(11): p. 1110-21.

34. Pindzola, R.R., C. Doller, and J. Silver, *Putative inhibitory extracellular matrix molecules at the dorsal root entry zone of the spinal cord during development and after root and sciatic nerve lesions.* Dev Biol, 1993. **156**(1): p. 34-48.

35. Pasterkamp, R.J., P.N. Anderson, and J. Verhaagen, *Peripheral nerve injury fails to induce growth of lesioned ascending dorsal column axons into spinal cord scar tissue expressing the axon repellent Semaphorin3A.* Eur J Neurosci, 2001. **13**(3): p. 457-71.

36. Bundesen, L.Q., et al., *Ephrin-B2 and EphB2 regulation of astrocyte-meningeal fibroblast interactions in response to spinal cord lesions in adult rats.* J Neurosci, 2003. **23**(21): p. 7789-800.

37. Hagino, S., et al., *Slit and glypican-1 mRNAs are coexpressed in the reactive astrocytes of the injured adult brain.* Glia, 2003. **42**(2): p. 130-8.

38. Liddelow, S.A., et al., *Neurotoxic reactive astrocytes are induced by activated microglia.* Nature, 2017. **541**(7638): p. 481-487.

39. Lawson, L.J., et al., *Heterogeneity in the distribution and morphology of microglia in the normal adult mouse brain.* Neuroscience, 1990. **39**(1): p. 151-70.

40. Mittelbronn, M., et al., *Local distribution of microglia in the normal adult human central nervous system differs by up to one order of magnitude.* Acta Neuropathol, 2001. **101**(3): p. 249-55.

41. Schafer, D.P., et al., *Microglia sculpt postnatal neural circuits in an activity and complement-dependent manner.* Neuron, 2012. **74**(4): p. 691-705.

42. Erblich, B., et al., *Absence of colony stimulation factor-1 receptor results in loss of microglia, disrupted brain development and olfactory deficits.* PLoS One, 2011. **6**(10): p. e26317.

43. Aarum, J., et al., *Migration and differentiation of neural precursor cells can be directed by microglia.* Proc Natl Acad Sci U S A, 2003. **100**(26): p. 15983-8.

44. Ginhoux, F., et al., *Fate mapping analysis reveals that adult microglia derive from primitive macrophages.* Science, 2010. **330**(6005): p. 841-5.

45. Ginhoux, F., et al., *Origin and differentiation of microglia.* Front Cell Neurosci, 2013. **7**: p. 45.

46. Kierdorf, K., et al., *Microglia emerge from erythromyeloid precursors via Pu.1- and Irf8-dependent pathways.* Nat Neurosci, 2013. **16**(3): p. 273-80.

47. Nikodemova, M., et al., *Microglial numbers attain adult levels after undergoing a rapid decrease in cell number in the third postnatal week.* J Neuroimmunol, 2015. **278**: p. 280-8.

48. Hefendehl, J.K., et al., *Homeostatic and injury-induced microglia behavior in the aging brain.* Aging Cell, 2014. **13**(1): p. 60-9.

49. Ransohoff, R.M. and V.H. Perry, *Microglial physiology: unique stimuli, specialized responses.* Annu Rev Immunol, 2009. **27**: p. 119-45.

50. Perry, V.H., P.B. Andersson, and S. Gordon, *Macrophages and inflammation in the central nervous system.* Trends Neurosci, 1993. **16**(7): p. 268-73.

51. Nimmerjahn, A., F. Kirchhoff, and F. Helmchen, *Resting microglial cells are highly dynamic surveillants of brain parenchyma in vivo.* Science, 2005. **308**(5726): p. 1314-8.

52. Boche, D., V.H. Perry, and J.A. Nicoll, *Review: activation patterns of microglia and their identification in the human brain.* Neuropathol Appl Neurobiol, 2013. **39**(1): p. 3-18.

53. Giulian, D. and T.J. Baker, *Characterization of ameboid microglia isolated from developing mammalian brain.* J Neurosci, 1986. **6**(8): p. 2163-78.

54. Bethea, J.R. and W.D. Dietrich, *Targeting the host inflammatory response in traumatic spinal cord injury.* Curr Opin Neurol, 2002. **15**(3): p. 355-60.

55. Cherry, J.D., J.A. Olschowka, and M.K. O'Banion, *Neuroinflammation and M2 microglia: the good, the bad, and the inflamed.* J Neuroinflammation, 2014. **11**: p. 98.

56. Brown, B.N., et al., *Macrophage phenotype and remodeling outcomes in response to biologic scaffolds with and without a cellular component.* Biomaterials, 2009. **30**(8): p. 1482-91.

57. Brown, B.N., et al., *Macrophage phenotype as a predictor of constructive remodeling following the implantation of biologically derived surgical mesh materials.* Acta Biomater, 2012. **8**(3): p. 978-87.

58. Filardy, A.A., et al., *Proinflammatory clearance of apoptotic neutrophils induces an IL-12(low)IL-10(high) regulatory phenotype in macrophages.* J Immunol, 2010. **185**(4): p. 2044-50.

59. Mantovani, A., et al., *The chemokine system in diverse forms of macrophage activation and polarization.* Trends Immunol, 2004. **25**(12): p. 677-86.

60. Gordon, S. and P.R. Taylor, *Monocyte and macrophage heterogeneity.* Nat Rev Immunol, 2005. **5**(12): p. 953-64.

61. Gadani, S.P., et al., *IL-4 in the brain: a cytokine to remember.* J Immunol, 2012. **189**(9): p. 4213-9.

62. Sica, A. and A. Mantovani, *Macrophage plasticity and polarization: in vivo veritas.* J Clin Invest, 2012. **122**(3): p. 787-95.

63. Edwards, J.P., et al., *Biochemical and functional characterization of three activated macrophage populations.* J Leukoc Biol, 2006. **80**(6): p. 1298-307.

64. Martinez, F.O., et al., *Macrophage activation and polarization.* Front Biosci, 2008. **13**: p. 453-61.

65. Pellerin, L. and P.J. Magistretti, *Neuroenergetics: calling upon astrocytes to satisfy hungry neurons.* Neuroscientist, 2004. **10**(1): p. 53-62.

66. Paulson, O.B. and E.A. Newman, *Does the release of potassium from astrocyte endfeet regulate cerebral blood flow?* Science, 1987. **237**(4817): p. 896-8.

67. Pellerin, L. and P.J. Magistretti, *Excitatory amino acids stimulate aerobic glycolysis in astrocytes via an activation of the Na+/K+ ATPase.* Dev Neurosci, 1996. **18**(5-6): p. 336-42.

68. Choi, H.B., et al., *Metabolic communication between astrocytes and neurons via bicarbonate-responsive soluble adenylyl cyclase.* Neuron, 2012. **75**(6): p. 1094-104.

69. Kimelberg, H.K. and M. Nedergaard, *Functions of astrocytes and their potential as therapeutic targets.* Neurotherapeutics, 2010. **7**(4): p. 338-53.

70. Freeman, M.R., *Specification and morphogenesis of astrocytes.* Science, 2010. **330**(6005): p. 774-8.

71. Halassa, M.M., et al., *Synaptic islands defined by the territory of a single astrocyte.* J Neurosci, 2007. **27**(24): p. 6473-7.

72. Sofroniew, M.V. and H.V. Vinters, *Astrocytes: biology and pathology.* Acta Neuropathol, 2010. **119**(1): p. 7-35.

73. Sofroniew, M.V., *Reactive astrocytes in neural repair and protection.* Neuroscientist, 2005. **11**(5): p. 400-7.

74. Faulkner, J.R., et al., *Reactive astrocytes protect tissue and preserve function after spinal cord injury.* J Neurosci, 2004. **24**(9): p. 2143-55.

75. Zador, Z., et al., *Role of aquaporin-4 in cerebral edema and stroke.* Handb Exp Pharmacol, 2009(190): p. 159-70.

76. Rothstein, J.D., et al., *Knockout of glutamate transporters reveals a major role for astroglial transport in excitotoxicity and clearance of glutamate.* Neuron, 1996. **16**(3): p. 675-86.

77. Sofroniew, M.V., *Molecular dissection of reactive astrogliosis and glial scar formation.* Trends Neurosci, 2009. **32**(12): p. 638-47.

78. Chen, D.F., S. Jhaveri, and G.E. Schneider, *Intrinsic changes in developing retinal neurons result in regenerative failure of their axons.* Proc Natl Acad Sci U S A, 1995. **92**(16): p. 7287-91.

79. Moya, K.L., et al., *Changes in rapidly transported proteins in developing hamster retinofugal axons.* J Neurosci, 1988. **8**(12): p. 4445-54.

80. Wang, J.T., et al., *Disease gene candidates revealed by expression profiling of retinal ganglion cell development.* J Neurosci, 2007. **27**(32): p. 8593-603.

81. Goldberg, J.L., et al., *Retinal ganglion cells do not extend axons by default: promotion by neurotrophic signaling and electrical activity.* Neuron, 2002. **33**(5): p. 689-702.

82. Sun, F., et al., *Sustained axon regeneration induced by co-deletion of PTEN and SOCS3.* Nature, 2011. **480**(7377): p. 372-5.

83. Benowitz, L.I. and Y. Yin, *Optic nerve regeneration.* Arch Ophthalmol, 2010. **128**(8): p. 1059-64.

84. Kurimoto, T., et al., *Long-distance axon regeneration in the mature optic nerve: contributions of oncomodulin, cAMP, and pten gene deletion.* J Neurosci, 2010. **30**(46): p. 15654-63.

85. Park, K.K., et al., *Promoting axon regeneration in the adult CNS by modulation of the PTEN/mTOR pathway.* Science, 2008. **322**(5903): p. 963-6.

86. Benowitz, L.I., Z. He, and J.L. Goldberg, *Reaching the brain: Advances in optic nerve regeneration.* Exp Neurol, 2015.

87. Moore, D.L., et al., *KLF family members regulate intrinsic axon regeneration ability.* Science, 2009. **326**(5950): p. 298-301.

88. Cui, D.M., et al., *KLF4 Knockdown Attenuates TBI-Induced Neuronal Damage through p53 and JAK-STAT3 Signaling.* CNS Neurosci Ther, 2017. **23**(2): p. 106-118.

89. Luo, X., et al., *Enhanced Transcriptional Activity and Mitochondrial Localization of STAT3 Co-induce Axon Regrowth in the Adult Central Nervous System.* Cell Rep, 2016. **15**(2): p. 398-410.

90. Mehta, S.T., et al., *Hyperactivated Stat3 boosts axon regeneration in the CNS.* Exp Neurol, 2016. **280**: p. 115-20.

91. Qin, S., Y. Zou, and C.L. Zhang, *Cross-talk between KLF4 and STAT3 regulates axon regeneration.* Nat Commun, 2013. **4**: p. 2633.

92. Li, Y., et al., *Mobile zinc increases rapidly in the retina after optic nerve injury and regulates ganglion cell survival and optic nerve regeneration.* Proc Natl Acad Sci U S A, 2017. **114**(2): p. E209-E218.

93. Cen, L.P., et al., *AAV-mediated transfer of RhoA shRNA and CNTF promotes retinal ganglion cell survival and axon regeneration.* Neuroscience, 2016. **343**: p. 472-482.

94. Smith, P.D., et al., *SOCS3 deletion promotes optic nerve regeneration in vivo.* Neuron, 2009. **64**(5): p. 617-23.

95. Marin, M.A., et al., *Reassembly of Excitable Domains after CNS Axon Regeneration.* J Neurosci, 2016. **36**(35): p. 9148-60.

96. Jin, D., et al., *Restoration of skilled locomotion by sprouting corticospinal axons induced by co-deletion of PTEN and SOCS3.* Nat Commun, 2015. **6**: p. 8074.

97. Badylak, S.F., *The extracellular matrix as a biologic scaffold material.* Biomaterials, 2007. **28**(25): p. 3587-93.

98. Massensini, A.R., et al., *Concentration-dependent rheological properties of ECM hydrogel for intracerebral delivery to a stroke cavity.* Acta Biomater, 2015. **27**: p. 116-30.

99. Badylak, S.F., *The extracellular matrix as a scaffold for tissue reconstruction.* Semin Cell Dev Biol, 2002. **13**(5): p. 377-83.

100. Costa, A., et al., *Biologic Scaffolds.* Cold Spring Harb Perspect Med, 2017. **7**(9).

101. Gilbert, T.W., et al., *Production and characterization of ECM powder: implications for tissue engineering applications.* Biomaterials, 2005. **26**(12): p. 1431-5.

102. Badylak, S.F., et al., *The use of extracellular matrix as an inductive scaffold for the partial replacement of functional myocardium.* Cell Transplant, 2006. **15 Suppl 1**: p. S29-40.

103. Freytes, D.O., et al., *Preparation and rheological characterization of a gel form of the porcine urinary bladder matrix.* Biomaterials, 2008. **29**(11): p. 1630-7.

104. Keane, T.J. and S.F. Badylak, *The host response to allogeneic and xenogeneic biological scaffold materials.* J Tissue Eng Regen Med, 2015. **9**(5): p. 504-11.

105. Brown, B.N., et al., *Macrophage polarization: an opportunity for improved outcomes in biomaterials and regenerative medicine.* Biomaterials, 2012. **33**(15): p. 3792-802.

106. Agrawal, V., et al., *Epimorphic regeneration approach to tissue replacement in adult mammals.* Proc Natl Acad Sci U S A, 2010. **107**(8): p. 3351-5.

107. Beattie, A.J., et al., *Chemoattraction of progenitor cells by remodeling extracellular matrix scaffolds.* Tissue Eng Part A, 2009. **15**(5): p. 1119-25.

108. Huleihel, L., et al., *Matrix bound nanovesicles recapitulate extracellular matrix effects on macrophage phenotype.* Tissue Eng Part A, 2017.

109. Dziki, J.L., et al., *Extracellular Matrix Bioscaffolds as Immunomodulatory Biomaterials.* Tissue Eng Part A, 2017.

110. Agrawal, V., et al., *Recruitment of progenitor cells by an extracellular matrix cryptic peptide in a mouse model of digit amputation.* Tissue Eng Part A, 2011. **17**(19-20): p. 2435-43.

111. Fercana, G.R., et al., *Perivascular extracellular matrix hydrogels mimic native matrix microarchitecture and promote angiogenesis via basic fibroblast growth factor.* Biomaterials, 2017. **123**: p. 142-154.

112. Wu, Y., et al., *Implantation of Brain-derived Extracellular Matrix Enhances Neurological Recovery after Traumatic Brain Injury.* Cell Transplant, 2016.

113. Lynch, K. and M. Pei, *Age associated communication between cells and matrix: a potential impact on stem cell-based tissue regeneration strategies.* Organogenesis, 2014. **10**(3): p. 289-98.

114. Kurtz, A. and S.J. Oh, *Age related changes of the extracellular matrix and stem cell maintenance.* Prev Med, 2012. **54 Suppl**: p. S50-6.

115. Sokocevic, D., et al., *The effect of age and emphysematous and fibrotic injury on the re-cellularization of de-cellularized lungs.* Biomaterials, 2013. **34**(13): p. 3256-69.

116. Williams, C., et al., *Young developmental age cardiac extracellular matrix promotes the expansion of neonatal cardiomyocytes in vitro.* Acta Biomater, 2014. **10**(1): p. 194-204.

117. Nakayama, K.H., et al., *Renal tissue engineering with decellularized rhesus monkey kidneys: age-related differences.* Tissue Eng Part A, 2011. **17**(23-24): p. 2891-901.

118. Huleihel, L., et al., *Matrix-bound nanovesicles within ECM bioscaffolds.* Sci Adv, 2016. **2**(6): p. e1600502.

119. Faust, A., et al., *Urinary bladder extracellular matrix hydrogels and matrix-bound vesicles differentially regulate central nervous system neuron viability and axon growth and branching.* Journal of Biomaterials Applications, 2017.

120. Huleihel, L., et al., *Matrix-Bound Nanovesicles Recapitulate Extracellular Matrix Effects on Macrophage Phenotype.* Tissue Eng Part A, 2017.

121. Faust, A., et al., *Urinary bladder extracellular matrix hydrogels and matrix-bound vesicles differentially regulate central nervous system neuron viability and axon growth and branching.* J Biomater Appl, 2017. **31**(9): p. 1277-1295.

122. Huleihel, L., et al., *Macrophage phenotype in response to ECM bioscaffolds.* Semin Immunol, 2017.

123. Xin, H., et al., *Exosome-mediated transfer of miR-133b from multipotent mesenchymal stromal cells to neural cells contributes to neurite outgrowth.* Stem Cells, 2012. **30**(7): p. 1556-64.

124. Le, M.T., et al., *MicroRNA-125b promotes neuronal differentiation in human cells by repressing multiple targets.* Mol Cell Biol, 2009. **29**(19): p. 5290-305.

125. Han, F., et al., *MicroRNA-30b promotes axon outgrowth of retinal ganglion cells by inhibiting Semaphorin3A expression.* Brain Res, 2015. **1611**: p. 65-73.

126. Thanos, S. and R. Naskar, *Correlation between retinal ganglion cell death and chronically developing inherited glaucoma in a new rat mutant.* Exp Eye Res, 2004. **79**(1): p. 119-29.

127. Danesh-Meyer, H.V. and L.A. Levin, *Glaucoma as a neurodegenerative disease.* J Neuroophthalmol, 2015. **35 Suppl 1**: p. S22-8.

128. Vohra, R., J.C. Tsai, and M. Kolko, *The role of inflammation in the pathogenesis of glaucoma.* Surv Ophthalmol, 2013. **58**(4): p. 311-20.

129. Danesh-Meyer, H.V., et al., *Optic disc morphology in open-angle glaucoma compared with anterior ischemic optic neuropathies.* Invest Ophthalmol Vis Sci, 2010. **51**(4): p. 2003-10.

130. Quigley, H.A. and A.T. Broman, *The number of people with glaucoma worldwide in 2010 and 2020.* Br J Ophthalmol, 2006. **90**(3): p. 262-7.

131. Tham, Y.C., et al., *Global prevalence of glaucoma and projections of glaucoma burden through 2040: a systematic review and meta-analysis.* Ophthalmology, 2014. **121**(11): p. 2081-90.

132. Susanna, R., Jr., et al., *Why Do People (Still) Go Blind from Glaucoma?* Transl Vis Sci Technol, 2015. **4**(2): p. 1.

133. Cohen, L.P. and L.R. Pasquale, *Clinical characteristics and current treatment of glaucoma.* Cold Spring Harb Perspect Med, 2014. **4**(6).

134. Morrison, J.C., E. Johnson, and W.O. Cepurna, *Rat models for glaucoma research.* Prog Brain Res, 2008. **173**: p. 285-301.

135. Weinreb, R.N. and J.D. Lindsey, *The importance of models in glaucoma research.* J Glaucoma, 2005. **14**(4): p. 302-4.

136. Yucel, Y. and N. Gupta, *Glaucoma of the brain: a disease model for the study of transsynaptic neural degeneration.* Prog Brain Res, 2008. **173**: p. 465-78.

137. Yucel, Y.H. and N. Gupta, *A framework to explore the visual brain in glaucoma with lessons from models and man.* Exp Eye Res, 2015. **141**: p. 171-8.

138. Lawlor, M., et al., *Glaucoma and the brain: Trans-synaptic degeneration, structural change, and implications for neuroprotection.* Surv Ophthalmol, 2017.

139. Cacabelos, R., et al., *Therapeutic effects of CDP-choline in Alzheimer's disease. Cognition, brain mapping, cerebrovascular hemodynamics, and immune factors.* Ann N Y Acad Sci, 1996. **777**: p. 399-403.

140. Galletti, P., et al., *Biochemical rationale for the use of CDPcholine in traumatic brain injury: pharmacokinetics of the orally administered drug.* J Neurol Sci, 1991. **103 Suppl**: p. S19-25.

141. Skripuletz, T., et al., *Pivotal role of choline metabolites in remyelination.* Brain, 2015. **138**(Pt 2): p. 398-413.

142. Alvarez-Sabin, J., et al., *Long-Term Treatment with Citicoline Prevents Cognitive Decline and Predicts a Better Quality of Life after a First Ischemic Stroke.* Int J Mol Sci, 2016. **17**(3).

143. Schauss, A.G., et al., *Single- and repeated-dose oral toxicity studies of citicoline free-base (choline cytidine 5'-pyrophosphate) in Sprague-Dawley rats.* Int J Toxicol, 2009. **28**(6): p. 479-87.

144. Weiss, G.B., *Metabolism and actions of CDP-choline as an endogenous compound and administered exogenously as citicoline.* Life Sci, 1995. **56**(9): p. 637-60.

145. Secades, J.J. and J.L. Lorenzo, *Citicoline: pharmacological and clinical review, 2006 update.* Methods Find Exp Clin Pharmacol, 2006. **28 Suppl B**: p. 1-56.

146. Martinet, M., P. Fonlupt, and H. Pacheco, *Effects of cytidine-5' diphosphocholine on norepinephrine, dopamine and serotonin synthesis in various regions of the rat brain.* Arch Int Pharmacodyn Ther, 1979. **239**(1): p. 52-61.

147. Galletti, P., et al., *Transport and metabolism of double-labelled CDPcholine in mammalian tissues.* Biochem Pharmacol, 1985. **34**(23): p. 4121-30.

148. Horsfield, M.A. and D.K. Jones, *Applications of diffusion-weighted and diffusion tensor MRI to white matter diseases - a review.* NMR Biomed, 2002. **15**(7-8): p. 570-7.

149. Song, S.K., et al., *Diffusion tensor imaging detects and differentiates axon and myelin degeneration in mouse optic nerve after retinal ischemia.* Neuroimage, 2003. **20**(3): p. 1714-22.

150. Pawela, C.P., et al., *Resting-state functional connectivity of the rat brain.* Magn Reson Med, 2008. **59**(5): p. 1021-9.

151. Yu, Y. and Y. Chau, *Formulation of in situ chemically cross-linked hydrogel depots for protein release: from the blob model perspective.* Biomacromolecules, 2015. **16**(1): p. 56-65.

152. Douglas, R.M., et al., *Independent visual threshold measurements in the two eyes of freely moving rats and mice using a virtual-reality optokinetic system.* Vis Neurosci, 2005. **22**(5): p. 677-84.

153. Prusky, G.T., et al., *Rapid quantification of adult and developing mouse spatial vision using a virtual optomotor system.* Invest Ophthalmol Vis Sci, 2004. **45**(12): p. 4611-6.

154. Paxinos, G. and C. Watson, *The Rat Brain in Stereotaxic Coordinates: Hard Cover Edition*. 2006: Elsevier Science.

155. Forrester, J. and A. Peters, *Nerve fibres in optic nerve of rat.* Nature, 1967. **214**(5085): p. 245-7.

156. Frezzotti, P., et al., *Structural and functional brain changes beyond visual system in patients with advanced glaucoma.* PLoS One, 2014. **9**(8): p. e105931.

157. Abbott, C.J., et al., *Evaluation of retinal nerve fiber layer thickness and axonal transport 1 and 2 weeks after 8 hours of acute intraocular pressure elevation in rats.* Invest Ophthalmol Vis Sci, 2014. **55**(2): p. 674-87.

158. Fortune, B., et al., *Deformation of the rodent optic nerve head and peripapillary structures during acute intraocular pressure elevation.* Invest Ophthalmol Vis Sci, 2011. **52**(9): p. 6651-61.

159. Fortune, B., et al., *The effect of acute intraocular pressure elevation on peripapillary retinal thickness, retinal nerve fiber layer thickness, and retardance.* Invest Ophthalmol Vis Sci, 2009. **50**(10): p. 4719-26.

160. Crish, S.D., et al., *Distal axonopathy with structural persistence in glaucomatous neurodegeneration.* Proc Natl Acad Sci U S A, 2010. **107**(11): p. 5196-201.

161. Buckingham, B.P., et al., *Progressive ganglion cell degeneration precedes neuronal loss in a mouse model of glaucoma.* J Neurosci, 2008. **28**(11): p. 2735-44.

162. Thuen, M., et al., *Manganese-enhanced MRI of the optic visual pathway and optic nerve injury in adult rats.* J Magn Reson Imaging, 2005. **22**(4): p. 492-500.

163. Chan, K.C., et al., *In vivo visuotopic brain mapping with manganese-enhanced MRI and resting-state functional connectivity MRI.* Neuroimage, 2014. **90**: p. 235-45.

164. Liang, Y.X., et al., *CNS regeneration after chronic injury using a self-assembled nanomaterial and MEMRI for real-time in vivo monitoring.* Nanomedicine, 2011. **7**(3): p. 351-9.

165. Chan, K.C., et al., *Longitudinal Assessments of Normal and Perilesional Tissues in Focal Brain Ischemia and Partial Optic Nerve Injury with Manganese-enhanced MRI.* Sci Rep, 2017. **7**: p. 43124.

166. Ho, L.C., et al., *In Vivo Evaluation of White Matter Integrity and Anterograde Transport in Visual System After Excitotoxic Retinal Injury With Multimodal MRI and OCT.* Invest Ophthalmol Vis Sci, 2015. **56**(6): p. 3788-800.

167. van der Heijden, M.E., et al., *Effects of Chronic and Acute Intraocular Pressure Elevation on Scotopic and Photopic Contrast Sensitivity in Mice.* Invest Ophthalmol Vis Sci, 2016. **57**(7): p. 3077-87.

168. Chan, K.C., K.F. So, and E.X. Wu, *Proton magnetic resonance spectroscopy revealed choline reduction in the visual cortex in an experimental model of chronic glaucoma.* Exp Eye Res, 2009. **88**(1): p. 65-70.

169. Babb, S.M., et al., *Oral choline increases choline metabolites in human brain.* Psychiatry Res, 2004. **130**(1): p. 1-9.

170. Parisi, V., et al., *Treatment with citicoline eye drops enhances retinal function and neural conduction along the visual pathways in open angle glaucoma.* Graefes Arch Clin Exp Ophthalmol, 2015. **253**(8): p. 1327-40.

171. Chamoun, M., et al., *Dose-dependent effect of donepezil administration on long-term enhancement of visually evoked potentials and cholinergic receptor overexpression in rat visual cortex.* J Physiol Paris, 2016. **110**(1-2): p. 65-74.

172. Khor, C.C., et al., *Genome-wide association study identifies five new susceptibility loci for primary angle closure glaucoma.* Nat Genet, 2016. **48**(5): p. 556-62.

173. Dekeyster, E., et al., *Ocular hypertension results in retinotopic alterations in the visual cortex of adult mice.* Curr Eye Res, 2015. **40**(12): p. 1269-83.

174. Klaassens, B.L., et al., *Time related effects on functional brain connectivity after serotonergic and cholinergic neuromodulation.* Hum Brain Mapp, 2016.

175. Chamoun, M., et al., *Cholinergic Potentiation of Restoration of Visual Function after Optic Nerve Damage in Rats.* Neural Plast, 2017. **2017**: p. 6928489.

176. Shah, D., et al., *Cholinergic and serotonergic modulations differentially affect large-scale functional networks in the mouse brain.* Brain Struct Funct, 2016. **221**(6): p. 3067-79.

177. Shah, D., et al., *Acute modulation of the cholinergic system in the mouse brain detected by pharmacological resting-state functional MRI.* Neuroimage, 2015. **109**: p. 151-9.

178. Thuen, M., et al., *Manganese-enhanced MRI of the rat visual pathway: acute neural toxicity, contrast enhancement, axon resolution, axonal transport, and clearance of Mn(2+).* J Magn Reson Imaging, 2008. **28**(4): p. 855-65.

179. Schuettauf, F., et al., *Citicoline and lithium rescue retinal ganglion cells following partial optic nerve crush in the rat.* Exp Eye Res, 2006. **83**(5): p. 1128-34.

180. Park, C.H., et al., *Neuroprotective effect of citicoline against KA-induced neurotoxicity in the rat retina.* Exp Eye Res, 2005. **81**(3): p. 350-8.

181. Roberti, G., et al., *A preliminary study of the neuroprotective role of citicoline eye drops in glaucomatous optic neuropathy.* Indian J Ophthalmol, 2014. **62**(5): p. 549-53.

182. Grieb, P. and R. Rejdak, *Pharmacodynamics of citicoline relevant to the treatment of glaucoma.* J Neurosci Res, 2002. **67**(2): p. 143-8.

183. Parisi, V., et al., *Evidence of the neuroprotective role of citicoline in glaucoma patients.* Prog Brain Res, 2008. **173**: p. 541-54.

184. Rejdak, R., et al., *Oral citicoline treatment improves visual pathway function in glaucoma.* Med Sci Monit, 2003. **9**(3): p. PI24-8.

185. Grieb, P., et al., *Citicoline: A Food Beneficial for Patients Suffering from or Threated with Glaucoma.* Front Aging Neurosci, 2016. **8**: p. 73.

186. Grieb, P., *Neuroprotective properties of citicoline: facts, doubts and unresolved issues.* CNS Drugs, 2014. **28**(3): p. 185-93.

187. Silver, J., *The glial scar is more than just astrocytes.* Exp Neurol, 2016. **286**: p. 147-149.

188. Stichel, C.C. and H.W. Muller, *The CNS lesion scar: new vistas on an old regeneration barrier.* Cell Tissue Res, 1998. **294**(1): p. 1-9.

189. de Lima, S., G. Habboub, and L.I. Benowitz, *Combinatorial therapy stimulates long-distance regeneration, target reinnervation, and partial recovery of vision after optic nerve injury in mice.* Int Rev Neurobiol, 2012. **106**: p. 153-72.

190. Trakhtenberg, E.F., et al., *Zinc chelation and Klf9 knockdown cooperatively promote axon regeneration after optic nerve injury.* Exp Neurol, 2018. **300**: p. 22-29.

191. Bei, F., et al., *Restoration of Visual Function by Enhancing Conduction in Regenerated Axons.* Cell, 2016. **164**(1-2): p. 219-32.

192. Pernet, V., et al., *Long-distance axonal regeneration induced by CNTF gene transfer is impaired by axonal misguidance in the injured adult optic nerve.* Neurobiol Dis, 2013. **51**: p. 202-13.

193. Pernet, V., et al., *Misguidance and modulation of axonal regeneration by Stat3 and Rho/ROCK signaling in the transparent optic nerve.* Cell Death Dis, 2013. **4**: p. e734.

194. Sicari, B.M., et al., *The promotion of a constructive macrophage phenotype by solubilized extracellular matrix.* Biomaterials, 2014. **35**(30): p. 8605-12.

195. Du, P., et al., *Human lung fibroblast-derived matrix facilitates vascular morphogenesis in 3D environment and enhances skin wound healing.* Acta Biomater, 2017. **54**: p. 333-344.

196. Agrawal, V., et al., *Partial characterization of the Sox2+ cell population in an adult murine model of digit amputation.* Tissue Eng Part A, 2012. **18**(13-14): p. 1454-63.

197. Robinson, K.A., et al., *Extracellular matrix scaffold for cardiac repair.* Circulation, 2005. **112**(9 Suppl): p. I135-43.

198. Gaetani, R., et al., *Cardiac derived extracellular matrix enhances cardiogenic properties of human cardiac progenitor cells.* Cell Transplant, 2015.

199. Badylak, S.F., et al., *Esophageal reconstruction with ECM and muscle tissue in a dog model.* J Surg Res, 2005. **128**(1): p. 87-97.

200. Badylak, S.F., et al., *Esophageal preservation in five male patients after endoscopic inner-layer circumferential resection in the setting of superficial cancer: a regenerative medicine approach with a biologic scaffold.* Tissue Eng Part A, 2011. **17**(11-12): p. 1643-50.

201. Bhrany, A.D., et al., *Development of an esophagus acellular matrix tissue scaffold.* Tissue Eng, 2006. **12**(2): p. 319-30.

202. Wood, J.D., et al., *Use of a particulate extracellular matrix bioscaffold for treatment of acquired urinary incontinence in dogs.* J Am Vet Med Assoc, 2005. **226**(7): p. 1095-7.

203. Badylak, S.F., et al., *Mechanisms by which acellular biologic scaffolds promote functional skeletal muscle restoration.* Biomaterials, 2016. **103**: p. 128-36.

204. Ren, T., Y. van der Merwe, and M.B. Steketee, *Developing Extracellular Matrix Technology to Treat Retinal or Optic Nerve Injury(1,2,3).* eNeuro, 2015. **2**(5).

205. Meng, F., M. Modo, and S.F. Badylak, *Biologic scaffold for CNS repair.* Regen Med, 2014. **9**(3): p. 367-83.

206. Carey, L.E., et al., *In vivo degradation of 14C-labeled porcine dermis biologic scaffold.* Biomaterials, 2014. **35**(29): p. 8297-304.

207. Wu, J., et al., *An injectable extracellular matrix derived hydrogel for meniscus repair and regeneration.* Acta Biomater, 2015. **16**: p. 49-59.

208. Johnson, T.D., R.L. Braden, and K.L. Christman, *Injectable ECM scaffolds for cardiac repair.* Methods Mol Biol, 2014. **1181**: p. 109-20.

209. Yang, G., et al., *Enhancement of tenogenic differentiation of human adipose stem cells by tendon-derived extracellular matrix.* Biomaterials, 2013. **34**(37): p. 9295-306.

210. Lang, R., et al., *Three-dimensional culture of hepatocytes on porcine liver tissue-derived extracellular matrix.* Biomaterials, 2011. **32**(29): p. 7042-52.

211. Ghuman, H., et al., *ECM hydrogel for the treatment of stroke: Characterization of the host cell infiltrate.* Biomaterials, 2016. **91**: p. 166-81.

212. DeQuach, J.A., et al., *Decellularized porcine brain matrix for cell culture and tissue engineering scaffolds.* Tissue Eng Part A, 2011. **17**(21-22): p. 2583-92.

213. Crapo, P.M., et al., *Effects of biologic scaffolds on human stem cells and implications for CNS tissue engineering.* Tissue Eng Part A, 2014. **20**(1-2): p. 313-23.

214. Wolf, M.T., et al., *A hydrogel derived from decellularized dermal extracellular matrix.* Biomaterials, 2012. **33**(29): p. 7028-38.

215. Barres, B.A., et al., *Immunological, morphological, and electrophysiological variation among retinal ganglion cells purified by panning.* Neuron, 1988. **1**(9): p. 791-803.

216. Steketee, M.B., et al., *Regulation of intrinsic axon growth ability at retinal ganglion cell growth cones.* Invest Ophthalmol Vis Sci, 2014. **55**(7): p. 4369-77.

217. Feng, D.F., et al., *Standardizing optic nerve crushes with an aneurysm clip.* Neurol Res, 2010. **32**(5): p. 476-81.

218. McCloy, R.A., et al., *Partial inhibition of Cdk1 in G 2 phase overrides the SAC and decouples mitotic events.* Cell Cycle, 2014. **13**(9): p. 1400-12.

219. van der Merwe, Y., et al., *An Elastomeric Polymer Matrix, PEUU-Tac, Delivers Bioactive Tacrolimus Transdurally to the CNS in Rat.* EBioMedicine, 2017. **26**: p. 47-59.

220. Freytes, D.O., et al., *Hydrated versus lyophilized forms of porcine extracellular matrix derived from the urinary bladder.* J Biomed Mater Res A, 2008. **87**(4): p. 862-72.

221. Medberry, C.J., et al., *Hydrogels derived from central nervous system extracellular matrix.* Biomaterials, 2013. **34**(4): p. 1033-40.

222. Morishita, S., et al., *Systemic simvastatin rescues retinal ganglion cells from optic nerve injury possibly through suppression of astroglial NF-kappaB activation.* PLoS One, 2014. **9**(1): p. e84387.

223. Hashimoto, Y., et al., *Preparation and characterization of decellularized cornea using high-hydrostatic pressurization for corneal tissue engineering.* Biomaterials, 2010. **31**(14): p. 3941-8.

224. Goh, S.K., et al., *Perfusion-decellularized pancreas as a natural 3D scaffold for pancreatic tissue and whole organ engineering.* Biomaterials, 2013. **34**(28): p. 6760-72.

225. Kjellen, L. and U. Lindahl, *Proteoglycans: structures and interactions.* Annu Rev Biochem, 1991. **60**: p. 443-75.

226. Koci, Z., et al., *Extracellular Matrix Hydrogel Derived from Human Umbilical Cord as a Scaffold for Neural Tissue Repair and Its Comparison with Extracellular Matrix from Porcine Tissues.* Tissue Eng Part C Methods, 2017.

227. Tukmachev, D., et al., *Injectable Extracellular Matrix Hydrogels as Scaffolds for Spinal Cord Injury Repair.* Tissue Eng Part A, 2016. **22**(3-4): p. 306-17.

228. Hejcl, A., et al., *Adjusting the chemical and physical properties of hydrogels leads to improved stem cell survival and tissue ingrowth in spinal cord injury reconstruction: a comparative study of four methacrylate hydrogels.* Stem Cells Dev, 2013. **22**(20): p. 2794-805.

229. Perris, R. and D. Perissinotto, *Role of the extracellular matrix during neural crest cell migration.* Mech Dev, 2000. **95**(1-2): p. 3-21.

230. Sobeih, M.M. and G. Corfas, *Extracellular factors that regulate neuronal migration in the central nervous system.* Int J Dev Neurosci, 2002. **20**(3-5): p. 349-57.

231. Ulrich, R., et al., *Matrix metalloproteinases and their inhibitors in the developing mouse brain and spinal cord: a reverse transcription quantitative polymerase chain reaction study.* Dev Neurosci, 2005. **27**(6): p. 408-18.

232. Bilousova, T.V., et al., *Matrix metalloproteinase-7 disrupts dendritic spines in hippocampal neurons through NMDA receptor activation.* J Neurochem, 2006. **97**(1): p. 44-56.

233. Vaillant, C., et al., *Spatiotemporal expression patterns of metalloproteinases and their inhibitors in the postnatal developing rat cerebellum.* J Neurosci, 1999. **19**(12): p. 4994-5004.

234. Hubschmann, M.V., et al., *Neural cell adhesion molecule function is regulated by metalloproteinase-mediated ectodomain release.* J Neurosci Res, 2005. **80**(6): p. 826-37.

235. Kalus, I., et al., *Proteolytic cleavage of the neural cell adhesion molecule by ADAM17/TACE is involved in neurite outgrowth.* J Neurochem, 2006. **98**(1): p. 78-88.

236. Angeloni, N.L., et al., *Regeneration of the cavernous nerve by Sonic hedgehog using aligned peptide amphiphile nanofibers.* Biomaterials, 2011. **32**(4): p. 1091-101.

237. Coulson-Thomas, V.J., et al., *Tumor Necrosis Factor-stimulated Gene-6 (TSG-6) Is Constitutively Expressed in Adult Central Nervous System (CNS) and Associated with Astrocyte-mediated Glial Scar Formation following Spinal Cord Injury.* J Biol Chem, 2016. **291**(38): p. 19939-52.

238. Cregg, J.M., et al., *Functional regeneration beyond the glial scar.* Exp Neurol, 2014. **253**: p. 197-207.

239. Zai, L.J. and J.R. Wrathall, *Cell proliferation and replacement following contusive spinal cord injury.* Glia, 2005. **50**(3): p. 247-57.

240. Wanner, I.B., et al., *Glial scar borders are formed by newly proliferated, elongated astrocytes that interact to corral inflammatory and fibrotic cells via STAT3-dependent mechanisms after spinal cord injury.* J Neurosci, 2013. **33**(31): p. 12870-86.

241. Bush, T.G., et al., *Leukocyte infiltration, neuronal degeneration, and neurite outgrowth after ablation of scar-forming, reactive astrocytes in adult transgenic mice.* Neuron, 1999. **23**(2): p. 297-308.

242. Myer, D.J., et al., *Essential protective roles of reactive astrocytes in traumatic brain injury.* Brain, 2006. **129**(Pt 10): p. 2761-72.

243. Huleihel, L., et al., *Matrix-Bound Nanovesicles Recapitulate Extracellular Matrix Effects on Macrophage Phenotype.* Tissue Eng Part A, 2017. **23**(21-22): p. 1283-1294.

244. van der Merwe, Y. and M.B. Steketee, *Immunomodulatory approaches to CNS injury: extracellular matrix and exosomes from extracellular matrix conditioned macrophages.* Neural Regen Res, 2016. **11**(4): p. 554-6.

245. Yin, Y., et al., *Macrophage-derived factors stimulate optic nerve regeneration.* J Neurosci, 2003. **23**(6): p. 2284-93.

246. Benowitz, L.I. and Y. Yin, *Combinatorial treatments for promoting axon regeneration in the CNS: strategies for overcoming inhibitory signals and activating neurons' intrinsic growth state.* Dev Neurobiol, 2007. **67**(9): p. 1148-65.

247. Popovich, P.G. and E.E. Longbrake, *Can the immune system be harnessed to repair the CNS?* Nat Rev Neurosci, 2008. **9**(6): p. 481-93.

248. Brinkmann, V. and A. Zychlinsky, *Neutrophil extracellular traps: is immunity the second function of chromatin?* J Cell Biol, 2012. **198**(5): p. 773-83.

249. Schnell, L., et al., *Acute inflammatory responses to mechanical lesions in the CNS: differences between brain and spinal cord.* Eur J Neurosci, 1999. **11**(10): p. 3648-58.

250. Donnelly, D.J. and P.G. Popovich, *Inflammation and its role in neuroprotection, axonal regeneration and functional recovery after spinal cord injury.* Exp Neurol, 2008. **209**(2): p. 378-88.

251. Soares, H.D., et al., *Inflammatory leukocytic recruitment and diffuse neuronal degeneration are separate pathological processes resulting from traumatic brain injury.* J Neurosci, 1995. **15**(12): p. 8223-33.

252. Holmin, S., et al., *Intracerebral inflammation after human brain contusion.* Neurosurgery, 1998. **42**(2): p. 291-8; discussion 298-9.

253. Sroga, J.M., et al., *Rats and mice exhibit distinct inflammatory reactions after spinal cord injury.* J Comp Neurol, 2003. **462**(2): p. 223-40.

254. Nagamoto-Combs, K., et al., *Prolonged microgliosis in the rhesus monkey central nervous system after traumatic brain injury.* J Neurotrauma, 2007. **24**(11): p. 1719-42.

255. Hains, B.C. and S.G. Waxman, *Activated microglia contribute to the maintenance of chronic pain after spinal cord injury.* J Neurosci, 2006. **26**(16): p. 4308-17.

256. Kigerl, K.A., et al., *Identification of two distinct macrophage subsets with divergent effects causing either neurotoxicity or regeneration in the injured mouse spinal cord.* J Neurosci, 2009. **29**(43): p. 13435-44.

257. Rosario, D.J., et al., *Decellularization and sterilization of porcine urinary bladder matrix for tissue engineering in the lower urinary tract.* Regen Med, 2008. **3**(2): p. 145-56.

258. Van der Merwe, Y., et al., *An Elastomeric Polymer Matrix, PEUU-Tac, Delivers Bioactive Tacrolimus Transdurally to the CNS in Rat.* EBioMedicine, 2017.

259. Chen, H., et al., *Optic neuropathy due to microbead-induced elevated intraocular pressure in the mouse.* Invest Ophthalmol Vis Sci, 2011. **52**(1): p. 36-44.

260. Shaw, P.X., et al., *Topical administration of a Rock/Net inhibitor promotes retinal ganglion cell survival and axon regeneration after optic nerve injury.* Exp Eye Res, 2016.

261. Alarcon-Martinez, L., et al., *Short and long term axotomy-induced ERG changes in albino and pigmented rats.* Mol Vis, 2009. **15**: p. 2373-83.

262. Riazifar, M., et al., *Stem Cell Extracellular Vesicles: Extended Messages of Regeneration.* Annu Rev Pharmacol Toxicol, 2017. **57**: p. 125-154.

263. Van der Merwe, Y. and M.B. Steketee, *Extracellular Vesicles: Biomarkers, Therapeutics, and Vehicles in the Visual System.* Curr Ophthalmol Rep 2017.

264. Li, B., et al., *Simvastatin attenuates microglial cells and astrocyte activation and decreases interleukin-1beta level after traumatic brain injury.* Neurosurgery, 2009. **65**(1): p. 179-85; discussion 185-6.

265. Lu, Y., et al., *Differential pro-inflammatory responses of astrocytes and microglia involve STAT3 activation in response to 1800 MHz radiofrequency fields.* PLoS One, 2014. **9**(9): p. e108318.

266. Huleihel, L., et al., *Macrophage phenotype in response to ECM bioscaffolds.* Semin Immunol, 2017. **29**: p. 2-13.

267. Badylak, S.F., et al., *Macrophage phenotype as a determinant of biologic scaffold remodeling.* Tissue Eng Part A, 2008. **14**(11): p. 1835-42.

268. Novak, M.L. and T.J. Koh, *Phenotypic transitions of macrophages orchestrate tissue repair.* Am J Pathol, 2013. **183**(5): p. 1352-1363.

269. Calkins, D.J., et al., *The challenge of regenerative therapies for the optic nerve in glaucoma.* Exp Eye Res, 2017.

270. Fitzgerald, M., et al., *Secondary retinal ganglion cell death and the neuroprotective effects of the calcium channel blocker lomerizine.* Invest Ophthalmol Vis Sci, 2009. **50**(11): p. 5456-62.

271. Sanes, J.R. and R.H. Masland, *The types of retinal ganglion cells: current status and implications for neuronal classification.* Annu Rev Neurosci, 2015. **38**: p. 221-46.

272. de Lima, S., et al., *Full-length axon regeneration in the adult mouse optic nerve and partial recovery of simple visual behaviors.* Proc Natl Acad Sci U S A, 2012. **109**(23): p. 9149-54.

273. Leibinger, M., et al., *Boosting Central Nervous System Axon Regeneration by Circumventing Limitations of Natural Cytokine Signaling.* Mol Ther, 2016. **24**(10): p. 1712-1725.

274. Chan, K.C., et al., *In vivo evaluation of retinal and callosal projections in early postnatal development and plasticity using manganese-enhanced MRI and diffusion tensor imaging.* Neuroimage, 2012. **59**(3): p. 2274-83.

275. Chan, K.C., et al., *In vivo retinotopic mapping of superior colliculus using manganese-enhanced magnetic resonance imaging.* Neuroimage, 2011. **54**(1): p. 389-95.

276. Kowal, J., et al., *Proteomic comparison defines novel markers to characterize heterogeneous populations of extracellular vesicle subtypes.* Proc Natl Acad Sci U S A, 2016. **113**(8): p. E968-77.

277. Kole, A.J., et al., *miR-29b is activated during neuronal maturation and targets BH3-only genes to restrict apoptosis.* Genes Dev, 2011. **25**(2): p. 125-30.

278. Cui, Y., et al., *MiR-125b orchestrates cell proliferation, differentiation and migration in neural stem/progenitor cells by targeting Nestin.* BMC Neurosci, 2012. **13**: p. 116.

279. Patron, J.P., et al., *MiR-133b targets antiapoptotic genes and enhances death receptor-induced apoptosis.* PLoS One, 2012. **7**(4): p. e35345.

280. Hu, K., et al., *MicroRNA expression profile of the hippocampus in a rat model of temporal lobe epilepsy and miR-34a-targeted neuroprotection against hippocampal neurone cell apoptosis post-status epilepticus.* BMC Neurosci, 2012. **13**: p. 115.

281. Pomeshchik, Y., et al., *Interleukin-33 treatment reduces secondary injury and improves functional recovery after contusion spinal cord injury.* Brain Behav Immun, 2015. **44**: p. 68-81.

282. Gadani, S.P., et al., *The glia-derived alarmin IL-33 orchestrates the immune response and promotes recovery following CNS injury.* Neuron, 2015. **85**(4): p. 703-9.

283. Hu, B., et al., *Effect of Extracellular Vesicles on Neural Functional Recovery and Immunologic Suppression after Rat Cerebral Apoplexy.* Cell Physiol Biochem, 2016. **40**(1-2): p. 155-162.

284. Peruzzotti-Jametti, L., et al., *The role of the immune system in central nervous system plasticity after acute injury.* Neuroscience, 2014. **283**: p. 210-21.

285. Russo, R., et al., *Retinal ganglion cell death in glaucoma: exploring the role of neuroinflammation.* Eur J Pharmacol, 2016.

286. Petan, J.A., et al., *Physiochemical properties of generic formulations of tacrolimus in Mexico.* Transplant Proc, 2008. **40**(5): p. 1439-42.

287. Starzl, T.E., et al., *FK 506 for liver, kidney, and pancreas transplantation.* Lancet, 1989. **2**(8670): p. 1000-4.

288. Madan, V. and C.E. Griffiths, *Systemic ciclosporin and tacrolimus in dermatology.* Dermatol Ther, 2007. **20**(4): p. 239-50.

289. Chen, B., et al., *Efficacy and safety of tacrolimus treatment for neuromyelitis optica spectrum disorder.* Sci Rep, 2017. **7**(1): p. 831.

290. Xu, X., et al., *FKBP12 is the only FK506 binding protein mediating T-cell inhibition by the immunosuppressant FK506.* Transplantation, 2002. **73**(11): p. 1835-8.

291. Zawadzka, M., et al., *Early steps of microglial activation are directly affected by neuroprotectant FK506 in both in vitro inflammation and in rat model of stroke.* J Mol Med (Berl), 2012. **90**(12): p. 1459-71.

292. Zawadzka, M. and B. Kaminska, *A novel mechanism of FK506-mediated neuroprotection: downregulation of cytokine expression in glial cells.* Glia, 2005. **49**(1): p. 36-51.

293. Szydlowska, K., M. Zawadzka, and B. Kaminska, *Neuroprotectant FK506 inhibits glutamate-induced apoptosis of astrocytes in vitro and in vivo.* J Neurochem, 2006. **99**(3): p. 965-75.

294. Liu, W., Y. Tang, and J. Feng, *Cross talk between activation of microglia and astrocytes in pathological conditions in the central nervous system.* Life Sci, 2011. **89**(5-6): p. 141-6.

295. Fukuta, T., et al., *Treatment of stroke with liposomal neuroprotective agents under cerebral ischemia conditions.* Eur J Pharm Biopharm, 2015. **97**(Pt A): p. 1-7.

296. Gold, B.G., D.M. Armistead, and M.S. Wang, *Non-FK506-binding protein-12 neuroimmunophilin ligands increase neurite elongation and accelerate nerve regeneration.* J Neurosci Res, 2005. **80**(1): p. 56-65.

297. Freeman, E.E. and C.L. Grosskreutz, *The effects of FK506 on retinal ganglion cells after optic nerve crush.* Invest Ophthalmol Vis Sci, 2000. **41**(5): p. 1111-5.

298. Wang, M.S. and B.G. Gold, *FK506 increases the regeneration of spinal cord axons in a predegenerated peripheral nerve autograft.* J Spinal Cord Med, 1999. **22**(4): p. 287-96.

299. Madsen, J.R., et al., *Tacrolimus (FK506) increases neuronal expression of GAP-43 and improves functional recovery after spinal cord injury in rats.* Exp Neurol, 1998. **154**(2): p. 673-83.

300. Voda, J., T. Yamaji, and B.G. Gold, *Neuroimmunophilin ligands improve functional recovery and increase axonal growth after spinal cord hemisection in rats.* J Neurotrauma, 2005. **22**(10): p. 1150-61.

301. Sharifi, Z.N., et al., *Effects of FK506 on Hippocampal CA1 Cells Following Transient Global Ischemia/Reperfusion in Wistar Rat.* Stroke Res Treat, 2012. **2012**: p. 809417.

302. Varghese, J., et al., *Tacrolimus-related adverse effects in liver transplant recipients: its association with trough concentrations.* Indian J Gastroenterol, 2014. **33**(3): p. 219-25.

303. Yamazoe, K., et al., *Efficacy and safety of systemic tacrolimus in high-risk penetrating keratoplasty after graft failure with systemic cyclosporine.* Cornea, 2014. **33**(11): p. 1157-63.

304. Randhawa, P.S., T.E. Starzl, and A.J. Demetris, *Tacrolimus (FK506)-Associated Renal Pathology.* Adv Anat Pathol, 1997. **4**(4): p. 265-276.

305. Gabriel, D., et al., *Improved topical delivery of tacrolimus: A novel composite hydrogel formulation for the treatment of psoriasis.* J Control Release, 2016. **242**: p. 16-24.

306. Deuse, T., et al., *Mechanisms behind local immunosuppression using inhaled tacrolimus in preclinical models of lung transplantation.* Am J Respir Cell Mol Biol, 2010. **43**(4): p. 403-12.

307. Lapteva, M., et al., *Polymeric micelle nanocarriers for the cutaneous delivery of tacrolimus: a targeted approach for the treatment of psoriasis.* Mol Pharm, 2014. **11**(9): p. 2989-3001.

308. Tajdaran, K., et al., *A novel polymeric drug delivery system for localized and sustained release of tacrolimus (FK506).* Biotechnol Bioeng, 2015. **112**(9): p. 1948-53.

309. Guan, J., et al., *Synthesis, characterization, and cytocompatibility of elastomeric, biodegradable poly(ester-urethane)ureas based on poly(caprolactone) and putrescine.* J Biomed Mater Res, 2002. **61**(3): p. 493-503.

310. Stankus, J.J., J. Guan, and W.R. Wagner, *Fabrication of biodegradable elastomeric scaffolds with sub-micron morphologies.* J Biomed Mater Res A, 2004. **70**(4): p. 603-14.

311. Steketee, M.B., et al., *Nanoparticle-mediated signaling endosome localization regulates growth cone motility and neurite growth.* Proc Natl Acad Sci U S A, 2011. **108**(47): p. 19042-7.

312. Hong, Y., et al., *Mechanical properties and in vivo behavior of a biodegradable synthetic polymer microfiber-extracellular matrix hydrogel biohybrid scaffold.* Biomaterials, 2011. **32**(13): p. 3387-94.

313. Howrie, D.L., et al., *Anaphylactoid reactions associated with parenteral cyclosporine use: possible role of Cremophor EL.* Drug Intell Clin Pharm, 1985. **19**(6): p. 425-7.

314. Hong, Y., et al., *Tailoring the degradation kinetics of poly(ester carbonate urethane)urea thermoplastic elastomers for tissue engineering scaffolds.* Biomaterials, 2010. **31**(15): p. 4249-58.

315. Sarikcioglu, L., N. Demir, and A. Demirtop, *A standardized method to create optic nerve crush: Yasargil aneurysm clip.* Exp Eye Res, 2007. **84**(2): p. 373-7.

316. Solari, M.G., et al., *Daily topical tacrolimus therapy prevents skin rejection in a rodent hind limb allograft model.* Plast Reconstr Surg, 2009. **123**(2 Suppl): p. 17S-25S.

317. Unadkat, J.V., et al., *Single Implantable FK506 Disk Prevents Rejection in Vascularized Composite Allotransplantation.* Plast Reconstr Surg, 2017. **139**(2): p. 403e-414e.

318. Rosenstiel, P., et al., *Differential effects of immunophilin-ligands (FK506 and V-10,367) on survival and regeneration of rat retinal ganglion cells in vitro and after optic nerve crush in vivo.* J Neurotrauma, 2003. **20**(3): p. 297-307.

319. Steketee, M.B. and K.W. Tosney, *Contact with isolated sclerotome cells steers sensory growth cones by altering distinct elements of extension.* J Neurosci, 1999. **19**(9): p. 3495-506.

320. Takanari, K., et al., *Abdominal wall reconstruction by a regionally distinct biocomposite of extracellular matrix digest and a biodegradable elastomer.* J Tissue Eng Regen Med, 2016. **10**(9): p. 748-61.

321. D'Amore, A., et al., *Bi-layered polyurethane - Extracellular matrix cardiac patch improves ischemic ventricular wall remodeling in a rat model.* Biomaterials, 2016. **107**: p. 1-14.

322. Fields, J.A., et al., *Neuroprotective effects of the immunomodulatory drug FK506 in a model of HIV1-gp120 neurotoxicity.* J Neuroinflammation, 2016. **13**(1): p. 120.

323. Yang, R.K., et al., *Dose-dependent effects of FK506 on neuroregeneration in a rat model.* Plast Reconstr Surg, 2003. **112**(7): p. 1832-40.

324. Wakita, H., et al., *Dose-dependent, protective effect of FK506 against white matter changes in the rat brain after chronic cerebral ischemia.* Brain Res, 1998. **792**(1): p. 105-13.

325. Godwin, J.W., A.R. Pinto, and N.A. Rosenthal, *Macrophages are required for adult salamander limb regeneration.* Proc Natl Acad Sci U S A, 2013. **110**(23): p. 9415-20.

326. Griffin, M., et al., *Biomechanical Characterization of Human Soft Tissues Using Indentation and Tensile Testing.* J Vis Exp, 2016(118).

327. Maikos, J.T., R.A. Elias, and D.I. Shreiber, *Mechanical properties of dura mater from the rat brain and spinal cord.* J Neurotrauma, 2008. **25**(1): p. 38-51.

328. Fiford, R.J. and L.E. Bilston, *The mechanical properties of rat spinal cord in vitro.* J Biomech, 2005. **38**(7): p. 1509-15.

329. van Noort, R., et al., *A study of the uniaxial mechanical properties of human dura mater preserved in glycerol.* Biomaterials, 1981. **2**(1): p. 41-5.

330. Bilston, L.E. and L.E. Thibault, *The mechanical properties of the human cervical spinal cord in vitro.* Ann Biomed Eng, 1996. **24**(1): p. 67-74.

331. Raykin, J., et al., *Characterization of the mechanical behavior of the optic nerve sheath and its role in spaceflight-induced ophthalmic changes.* Biomech Model Mechanobiol, 2017. **16**(1): p. 33-43.

332. Fitzgerald, M., et al., *Early events of secondary degeneration after partial optic nerve transection: an immunohistochemical study.* J Neurotrauma, 2010. **27**(2): p. 439-52.

333. Toledo Perdomo, K., et al., *Reversible acute encephalopathy with mutism, induced by calcineurin inhibitors after renal transplantation.* J Nephrol, 2012. **25**(5): p. 839-42.

334. Bechstein, W.O., *Neurotoxicity of calcineurin inhibitors: impact and clinical management.* Transpl Int, 2000. **13**(5): p. 313-26.

335. Arnold, R., et al., *Association between calcineurin inhibitor treatment and peripheral nerve dysfunction in renal transplant recipients.* Am J Transplant, 2013. **13**(9): p. 2426-32.

336. Benowitz, L.I., Z. He, and J.L. Goldberg, *Reaching the brain: Advances in optic nerve regeneration.* Exp Neurol, 2017. **287**(Pt 3): p. 365-373.

337. Lyson, T., et al., *Cyclosporine- and FK506-induced sympathetic activation correlates with calcineurin-mediated inhibition of T-cell signaling.* Circ Res, 1993. **73**(3): p. 596-602.

338. Kato, H., et al., *Postischemic changes in the immunophilin FKBP12 in the rat brain.* Brain Res Mol Brain Res, 2000. **84**(1-2): p. 58-66.

339. Gold, B.G., et al., *FK506 and a nonimmunosuppressant derivative reduce axonal and myelin damage in experimental autoimmune encephalomyelitis: neuroimmunophilin ligand-mediated neuroprotection in a model of multiple sclerosis.* J Neurosci Res, 2004. **77**(3): p. 367-77.

340. Craighead, M.W., et al., *Human oligodendroglial cell line, MO3.13, can be protected from apoptosis using the general caspase inhibitor zVAD-FMK.* J Neurosci Res, 1999. **57**(2): p. 236-43.

341. Nottingham, S., P. Knapp, and J. Springer, *FK506 treatment inhibits caspase-3 activation and promotes oligodendroglial survival following traumatic spinal cord injury.* Exp Neurol, 2002. **177**(1): p. 242-51.

342. Aghdasi, B., et al., *FKBP12, the 12-kDa FK506-binding protein, is a physiologic regulator of the cell cycle.* Proc Natl Acad Sci U S A, 2001. **98**(5): p. 2425-30.

343. Ahearn, I.M., et al., *FKBP12 binds to acylated H-ras and promotes depalmitoylation.* Mol Cell, 2011. **41**(2): p. 173-85.

344. Anghel, D., et al., *Neurotoxicity of immunosuppressive therapies in organ transplantation.* Maedica (Buchar), 2013. **8**(2): p. 170-5.

345. Jacobson, P., et al., *Factors affecting the pharmacokinetics of tacrolimus (FK506) in hematopoietic cell transplant (HCT) patients.* Bone Marrow Transplant, 2001. **28**(8): p. 753-8.

346. Sikma, M.A., et al., *Pharmacokinetics and Toxicity of Tacrolimus Early After Heart and Lung Transplantation.* Am J Transplant, 2015. **15**(9): p. 2301-13.

347. Diehl, R., et al., *Immunosuppression for in vivo research: state-of-the-art protocols and experimental approaches.* Cell Mol Immunol, 2017. **14**(2): p. 146-179.

348. Noll, B.D., et al., *Validation of an LC-MS/MS method to measure tacrolimus in rat kidney and liver tissue and its application to human kidney biopsies.* Ther Drug Monit, 2013. **35**(5): p. 617-23.

349. Bottiger, Y., et al., *Tacrolimus whole blood concentrations correlate closely to side-effects in renal transplant recipients.* Br J Clin Pharmacol, 1999. **48**(3): p. 445-8.

350. Mayer, A.D., et al., *Multicenter randomized trial comparing tacrolimus (FK506) and cyclosporine in the prevention of renal allograft rejection: a report of the European Tacrolimus Multicenter Renal Study Group.* Transplantation, 1997. **64**(3): p. 436-43.